Numerical Study of Self-organized Fractal Systems

博士学位論文

論文題目　Numerical Study of
Self-organized Fractal Systems
(計算機シミュレーションによる
自己組織フラクタルの研究)

提出者　東北大学大学院情報科学研究科
システム情報科学　専攻

学籍番号　5ds20

氏名　稲岡　創

指導教官	高安 秀樹　教授
審査委員 （○印は主査）	○ 高安 秀樹 教授 1 澤田 康次 教授　2 岡田 正巳 教授 3 　　教授　4 　　教授 5 　　教授　6 　　教授

DOCTORAL DISSERTATION

Numerical Study of Self-organized Fractal Systems

Hajime Inaoka

Graduate School of Information Sciences,
Tohoku University,
Aoba-ku, Sendai 980, Japan

March, 1996

Contents

Acknowledgments

In the first place, I would like to thank Prof. H. Takayasu. My work during the last five years owes much to his thoughtful and helpful comments and suggestions.

I would like to thank my colleagues at our laboratory at the Graduate School of Information Sciences of the Tohoku University. My work was greatly encouraged by useful discussions and good scientific atmosphere in our laboratory. Especially, I would like to thank Dr. A. Yu. Tretyakov for carefully reading this doctoral dissertation.

I would also like to thank Prof. K. Ito and other people at the Department of Earth Sciences at the Kobe University for various help during my study there.

This work has been partially supported by the Japan Society for the Promotion of Science.

Chapter 1
Introduction

1.1 Approach to Fractal Systems

1.1.1 Concept of Fractals

"How long is the coast of Britain?" — Mandelbrot asked the question when he firstly introduced the concept of "fractal" [B. B. Mandelbrot (1967)]. He pointed out that the length of coastlines tends to diverge as the observing resolution becomes finer. The divergence of the length of the coastlines comes from their non-trivial self-similarity. "Fractal" is a generic term for objects showing non-trivial self-similarities. He introduced non-integer dimensionality called fractal dimension to characterize such non-trivial self-similar geometry into the field of physics.

At first, the idea of non-integer dimensionality must have given peculiar impression to scientists. But, in fact, we are surrounded by many fractal objects. For examples, coastlines, river networks, shape of mountains, surface of clouds, patterns of lightning, distributions of earthquakes, clusters of galaxies, patterns of cracks, branches of trees, blood vessels, time sequence of stock prices, and so on, — all these objects have been recognized to be fractal. As the familiarity of the fractal objects had been recognized, the concept of fractal started to attract much attention by scientists.

The concept of fractal is deeply related to the statistical power-law behaviors of physical quantities, and such power-law behaviors themselves are also referred to as fractals. For example, the fractal properties of a system often reveal themselves in power-law size distribution of a physical quantity, q, as

$$P(\geq q) \propto q^{-\tau} \quad , \tag{1.1}$$

where $P(\geq q)$ denotes the probability that the physical quantity takes a value larger than or equal to q. The energy released in earthquake phenomena is known to follow such a power-law distribution. The causes of exponential or Gaussian behaviors in a system can often be explained by considering in-

dependent events in the system in the frame of probability theory. On the other hand, it is not so easy to explain the causes of the power-law behaviors. In this sense, the power-law behaviors of physical quantities present an open non-trivial problem.

1.1.2 Fractals and Far-form-equilibrium Systems

In the early stage of the study of fractals, the main task of the scientists may have been characterizing various objects by fractal dimension. As the concept of fractal has become widely accepted, the central point of the studies has shifted to studying the causes of fractals.

We can say that the construction of the unified physics of equilibrium systems has been already accomplished. However, the wide existence of the fractal object in nature cannot be explained by the framework of the physics of the equilibrium systems. For example, the second law of thermodynamics insists that the entropy in a closed system increases until the system reaches the equilibrium state. Physically it means that the closed system tends to be homogeneous and that complex structures are destined to vanish. If the real world surrounding us tended to the equilibrium state, the fractal structures in nature would not be able to survive in long time period and, therefore, they would be rare.

On the other hand, in the last several decades, it was recognized that abundant complex patterns are spontaneously formed in far-from-equilibrium open systems. Also it has been found that some far-from-equilibrium systems spontaneously produce non-exponential or non-Gaussian behaviors of physical quantities including power-law behaviors. Since fractal objects found in nature are generally formed in far-from-equilibrium conditions, the study of the origins of fractal behaviors is linked to the development of the physics of far-from-equilibrium systems.

1.1.3 Self-organized Fractal Systems

By the studies of fractal systems in the last decade, there has been formed a consensus that many fractal behaviors in far-from-equilibrium systems are formed by mechanisms so-called fractal growth phenomena and self-organized criticality.

One of the typical examples of the fractal growth phenomena is the model of diffusion-limited aggregation. The model of the diffusion-limited aggregation numerically produces random branching fractal aggregates as shown in Fig.1.1. The aggregate in the system is grown by particles injected into the system. The injected particles perform random walks and irreversibly stick to become a part of the aggregate when they touch the aggregate. As can be seen from the mechanism, the diffusion-limited aggregation is a phenomenon in a far-from-equilibrium system. Later in Chapter 3, we will discuss the diffusion-limited aggregation in detail.

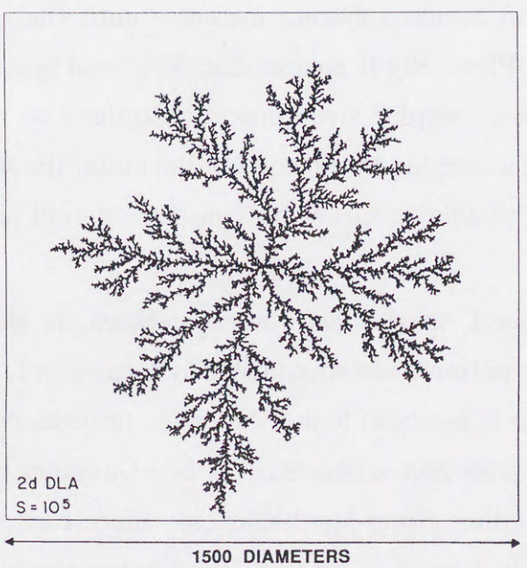

Figure 1.1: An example of an aggregate by the diffusion-limited aggregation [S. Tolman, P. Meakin, and M. Matsushita (1989), Fig.1(a)].

The key word to understand the mechanisms of the fractal growth phenomena is "competition". In the model of the diffusion-limited aggregation, the aggregate is formed under the condition of competition between growing branches: the competition for the diffusing particles. Namely, the larger branch can more effectively gather the diffusing particles and grow faster. During the last decade, it has been recognized that the competition between the growing elements is one of the essential factors for the fractal behaviors of the fractal growth systems.

Physicists had recognized the power-law behaviors of the physical quantities in second order phase transition phenomena long before the proposal of the concept of fractal. Since, in that case, the fractal behaviors are only observed around the critical point of the system, they are referred to as "critical phenomena". In the recent years, it has been found that some far-from-equilibrium systems can be regarded evolving themselves to the critical state and spontaneously producing fractal behaviors of physical quantities. These phenomena are now often referred to as "self-organized criticality". The fractal growth phenomena are also regarded as kinds of self-organized criticality on the point that they spontaneously produce power-law size distribution of growing elements. The studies of the self-organized criticality have become more and more extensive and, now, we see the rapid progress of the studies. We will also give detail discussion about the self-organized criticality in the next chapter.

1.2 Purpose of Study

Recent rapid progress of computer capabilities widens the range of applicability of computers to the studies of physical problems. In fact, the progress in the studies of fractal systems has been much supported by the study of numerical models.

In this doctoral dissertation, we study Laplacian fractals, river networks, and impact fracture mainly by using numerical models. We try to clarify the cause of the fractal behaviors of physical quantities, especially, the power-law size distribution seen in these systems. Throughout discussions, we stress the role of the competition seen in fractal growth systems in organizing fractal behaviors in these fractal systems.

In the following chapter, we introduce several basic concepts in the study of fractal systems and discuss the effectiveness of the numerical models in this field for later discussions. In Chapter 3, a model of the competitive process deduced from the mechanism of the Laplacian fractals is introduced. By the model we clarify the nature of the competition in the Laplacian fractals. In Chapter 4, we learn that the formation of the river networks by erosion process can be regarded as a kind of fractal growth processes. We introduce a numerical model for the erosion process intending to reproduce the fractal behaviors and several experiential laws of the river networks. In Chapter 5, we propose a model of impact fracture process by applying the concept of the competitive process. We intend to reproduce the power-law fragment size distribution confirmed by the experiments of impact fragmentation. The last chapter is devoted to a discuss on common features in the three models treated in detail in Chapters 3, 4, and 5. We find that the three models are at the self-organized critical state and that they commonly form self-similar or self-affine domain configurations in the space where the models are defined.

Chapter 2

Basic Concepts

2.1 Self-organized Criticality

Before the introduction of the concept of fractals, the power-law behavior of physical quantities had been already recognized in the field of the statistical physics of equilibrium systems related to second order phase transition [H. E. Stanley (1987)]. Phase transition in the model of percolation is a well studied example [D. Stauffer and A. Aharony (1985)].

The model of percolation is defined on a lattice. In the case of site percolation, each lattice site is regarded as occupied with probability p and empty with probability $1 - p$. The neighboring occupied sites are regarded to be connected to each other and an ensemble of connected sites makes a cluster separated by empty sites. We consider the percolation probability, P_∞, that there emerges an infinitely large cluster. It is known that there exists a critical probability, $p = p_c$, at which the phase transition takes place. Namely, the percolation probability P_∞ takes a non-zero value for $p > p_c$ while it is zero for $p \leq p_c$. At and in the vicinity of the critical probability, the system shows various non-trivial power-law behaviors. For example, the percolation probability P_∞ shows a power-law behavior as

$$P_\infty \propto (p - p_c)^\beta \tag{2.1}$$

for $p > p_c$ and the cumulative cluster size distribution, $P(\geq s)$, follows a power-law as

$$P(\geq s) \propto s^{-\tau} \tag{2.2}$$

at $p = p_c$, where s denotes the size of the cluster. Since such non-trivial power-law behaviors are only observed near the critical point, they are referred to as "critical phenomena".

Although critical phenomena are characterized by fractal behaviors, fractals in nature are highly unlikely to be caused by critical phenomena because we have to tune and keep the control parameter of the system around the critical

point to observe this kind of fractal behaviors. In the above example, we have to keep the probability p in the vicinity of the critical probability $p = p_c$. On the other hand, many kinds of fractal objects are widely seen in nature as if they emerge spontaneously and exist stably.

The critical phenomena introduced above is a concept in the statistical physics of equilibrium systems while systems found in nature are mostly in far-from-equilibrium state. In recent years, it has been recognized that some far-from-equilibrium systems organize the power-law behaviors of physical quantities without tuning of their control parameters. Such spontaneously appearing power-law behaviors in far-from-equilibrium systems are often referred to as "self-organized criticality". The self-organized criticality is now widely regarded as the cause of the fractals seen in nature.

2.1.1 Sandpile Model

The term "self-organized criticality" was firstly used in the study of a model called a sandpile model by Bak, Tang, and Wiesenfeld [P. Bak, C. Tang, and K. Wiesenfeld (1987) and (1988)]. Let us consider a situation when sand grains are deposited one by one at arbitrary points on a dish. At first, the sand is accumulated on the dish making a sandpile. When the sandpile grows large enough, avalanches of the sand triggered by falls of sand grains start to emerge flowing toward the edge of the dish. Eventually, the system reaches a kind of a steady state where avalanches of various size emerge with probability depending only on the avalanche size.

A lattice model was proposed to simulate the process. The model is defined on a two-dimensional square lattice and it is easily generalized to higher dimensions. Each lattice site (x, y) registers the number of the sand grains, $z(x, y)$, which can be regarded as the height at the site. For a given initial configuration of $z(x, y)$, the system evolves by repeating the following procedures:

1. The height of an arbitrary chosen site (x, y), $z(x, y)$, is increased by δz. In the numerical simulations, δz is usually set to $\delta z = 1$. This process corresponds to the fall of a sand grain.

2. If the height of the chosen site reaches a critical height, $z_c = 4\,\delta z$, by procedure 1, the sand grains at the chosen site are shifted to the four nearest neighbor sites, that is, the heights at the chosen site (x, y) and at its four nearest neighbor sites are replaced by

$$\begin{cases} z(x,y) & \rightarrow & z(x,y) - 4\,\delta z \\ z(x',y') & \rightarrow & z(x',y') + \delta z \end{cases} ,$$

   where (x', y') denotes the four nearest neighbor sites of the chosen site (x, y). We refer to this process as "relaxation".

3. In the procedure 2, if the height of the nearest neighbor site $z(x', y')$ again reaches the critical height, the relaxation again occurs in the same way as in procedure 1 at (x', y'). The relaxation process continues until a state where no site reaches the critical height is realized.

Note that, in a real sandpile, an avalanche occurs when the local slope at some point exceeds a certain critical slope, while, in the numerical model, the role of the slope is replaced by the height. In the above procedures, when the relaxation process reaches the edges of the system, the sand grain flows out of the system and it is lost. Manna also proposed a similar lattice model where $z_c = 2$ and the relaxed sand grains flow to arbitrary two nearest neighbor sites [S. S. Manna (1991)]. That is, in the procedure 2, when the height of a site reaches the critical value $z_c = 2$ the height is changed by

$$\begin{cases} z(x,y) & \rightarrow & z(x,y) - 2\,\delta z \\ z(x',y') & \rightarrow & z(x',y') + \delta z \end{cases} ,$$

where (x', y') denotes the arbitrary chosen two nearest neighbor sites of the relaxing site.

It is known that the size of the avalanche, the number of relaxing sites caused by a grain injection, follows a power-law distribution as

$$P(\geq s) \propto s^{-\tau} \quad , \tag{2.3}$$

where s denotes the avalanche size and τ is found in the range $\tau = 0.22 - 0.28$ for both models from large scale simulations [S. S. Manna (1990) and (1991)]. It is remarkable that the power-law behavior of the model is produced spontaneously.

2.2 Renormalization and Universality

Fractal systems are characterized and distinguished by the exponents of the power-law behaviors of physical quantities in the systems, for example, by fractal dimensions. The framework of real space renormalization group provides a powerful theoretical technique to evaluate the exponents in a way directly making use of the self-similarity of a fractal system [H. Takayasu (1990)]. In addition, the technique of the renormalization leads us to the concept of universality in fractal systems.

2.2.1 Real Space Renormalization Group

The real space renormalization group treats the change of physical quantities under the coarse graining of observation scale. Let $\boldsymbol{q}$ be a set of some physical quantities at certain observation scale. As the observation scale is coarse grained by a factor of b, the observed physical quantities change to $\boldsymbol{q}'$. Let us introduce the renormalization transformation, R_b, as

$$\boldsymbol{q}' = R_b(\boldsymbol{q}) \quad , \tag{2.4}$$

where b should take a value in the range of $b \geq 1$.

Considering renormalization transformations at coarse-graining factors b_1, b_2, and $b_1 \cdot b_2$, we argue that the result of two successive renormalization transformation R_{b_1} and R_{b_2} should be identical to the result of the transformation $R_{b_1 \cdot b_2}$. That is, the relation

$$R_{b_1} \cdot R_{b_2} = R_{b_2} \cdot R_{b_1} = R_{b_1 \cdot b_2} \tag{2.5}$$

should hold. For the identity transformation, R_1, we have

$$R_1 \cdot R_b = R_b \cdot R_1 = R_b \quad . \tag{2.6}$$

The relations Eqs.(2.5) and (2.6) show that the renormalization transformation R_b forms a semi-group. The term "renormalization group" comes from this property of the renormalization transformation.

Defining a renormalization transformation in a certain coarse-graining process, we find the fixed points of the transformation, $\boldsymbol{q}^*$, for which

$$\boldsymbol{q}^* = R_b(\boldsymbol{q}^*) \quad . \tag{2.7}$$

The relation Eq.(2.7) means that the physical properties of the system described by the set of the physical quantities $\boldsymbol{q}$ do not depend on the observation scale when $\boldsymbol{q}$ takes $\boldsymbol{q}^*$. This is directly related to the self-similarity of the system. The exponents of the power-law behaviors of the physical quantities in the system are calculated from the fixed point $\boldsymbol{q}^*$.

Although the renormalization group approach is an intuitively understandable powerful technique to investigate fractal systems, we should note that it is an approximate technique and that the fractal behavior of the system described by the technique sometimes differs from that in the real system.

2.2.2 Application to Sandpile Model

Let us introduce an example of the use of renormalization group approach by applying it to the sandpile model [L. Pietronero, A. Vespignani, and S. Zapperi (1994)].

Changing the observation scale by a factor of b, we consider coarse-grained supersites of size b. Here, we consider the two-dimensional case, so a supersite contains b^2 usual sites. It is regarded that the relaxation of a supersite occurs when the relaxation of the usual sites spans the supersite to involve the neighboring supersites. In the case illustrated in Fig.2.1, the relaxation spans to one of the nearest neighbor supersites. Therefore, it is regarded that the coarse-grained relaxation to the nearest neighbor supersite occurs. Let p_i be the probability that the relaxed sand flows to i nearest neighbor sites when

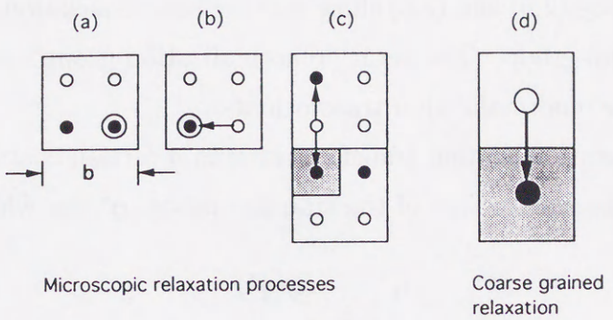

Figure 2.1: An example of the renormalization scheme for the relaxation dynamics. The sites illustrated by marks ○, ●, and ⊙ are non-critical, critical, and relaxing sites, respectively [L. Pietronero, A. Vespignani, and S. Zapperi (1994), Fig.4].

a relaxation of a site occurs. Note that i takes one, two, three, or four in the case of a two-dimensional square lattice. The probability p_i satisfies the normalization condition,

$$\sum_{i=1}^{4} p_i = 1 \quad . \tag{2.8}$$

The sets of p_i for the models by Bak et al. and Manna are $(p_1, p_2, p_3, p_4) = (0, 0, 0, 1)$ and $(0, 1, 0, 0)$, respectively.

We denote the concentration of the critical sites where a relaxation is caused by adding one sand grain having additional height δz by ρ. We consider the renormalization transformation for p_i and ρ as following.

We label the configuration of critical and non-critical sites in a super site by ω. Assuming that the spatial distribution of the critical sites is independent, the realization probability for ω, $W(\omega)$, is calculated for each configuration. In the example of the case $b = 2$ shown in Fig.2.1, the probability $W(\omega)$ is calculated as

$$W(\omega) = \rho^2(1-\rho)^2 \tag{2.9}$$

since the configuration consists of two critical and two non-critical sites. The probability that the relaxation process shown in Fig.2.1(b) occurs is calcu-

lated as $\frac{1}{4}{p_1}^{(k)}$ since the relaxation has equal chance to occur to four nearest neighbors. The index (k) denotes that the quantity is observed before the renormalization. In the same way, the probability for the process in Fig.2.1(c) is $\frac{1}{6}{p_2}^{(k)}$. Therefore, the probability of the realization of the relaxation process shown in Fig.2.1 is calculated as $\frac{1}{24}{p_1}^{(k)}{p_2}^{(k)}$. We calculate the probabilities for all the realizations of the relaxation process on a configuration ω. The probabilities of the realizations are classified by the number of the destinations of the supersite relaxation, i: the number of the nearest neighbor supersites where the relaxed sand flows to. Then the classified probabilities are summed up making renormalized probability set on ω, ${p_i}^{(k+1)}(\omega)$. The index $(k+1)$ denotes the observed quantities after the renormalization. The renormalized probability sets ${p_i}^{(k+1)}(\omega)$ are calculated for all the configurations ω. The renormalization transformation of the probability set p_i is defined by the sum of ${p_i}^{(k+1)}(\omega)$ weighted by $W(\omega)$ for all ω. That is, the transformation is defined as

$$ {p_i}^{(k+1)} \equiv \sum_{\omega} W(\omega)\, {p_i}^{(k)}(\omega) = F_i(\rho^{(k)}, {p_i}^{(k)}) \quad , \tag{2.10} $$

where the right part of the equation, $F_i(\rho^{(k)}, {p_i}^{(k)})$, represents that the transformation is a set of functions of the probability $\rho^{(k)}$ and ${p_i}^{(k)}$.

The quantity of the sand during the relaxation process is conserved in the sandpile model. It means that the quantity of outflowing sand from a site is equal to that of the inflowing sand into the site on the average. This property should be preserved after the renormalization transformation, which serves as a condition determining the renormalized concentration of the critical sites, $\rho^{(k+1)}$. Using the renormalized height unit, $\delta z^{(k+1)}$, the condition is written as

$$ \delta z^{(k+1)} = \rho^{(k+1)}\, \delta z^{(k+1)} \Big(\sum_{i=1}^{4} i\, {p_i}^{(k+1)}\Big) \quad . \tag{2.11} $$

By solving Eq.(2.11) and using (2.10), the renormalized critical site concentration is written by a function of the probability $\rho^{(k)}$ and ${p_i}^{(k)}$, F_ρ, as

$$ \rho^{(k+1)} = F_\rho(\rho^{(k)}, {p_i}^{(k)}) \quad . \tag{2.12} $$

By Eqs.(2.10) and (2.12), the renormalization transformation for p_i and ρ is represented as a set of functions of $\rho^{(k)}$ and $p_i{}^{(k)}$. The transformation is so complex that it is difficult to theoretically calculate the fixed point, $p_i{}^*$ and ρ^*. However, by assuming a proper value of initial critical site concentration, $\rho^{(0)}$, the initial probability set, $p_i{}^{(0)}$, for the models by Bak et al. and Manna can be numerically renormalized. By the transformation Eqs.(2.10) and (2.12), $p_i{}^{(0)}$ and $\rho^{(0)}$ are transformed to $p_i{}^{(1)}$ and $\rho^{(1)}$. Applying the transformation again to the results, we get $p_i{}^{(2)}$ and $\rho^{(2)}$. By repeating such iteration, it is found that $p_i{}^{(k)}$ and $\rho^{(k)}$ starting from both the initial conditions for the models by Bak et al. and Manna asymptotically approach to a common fixed point as shown in Table 2.2.

Number of iterations (k)	ρ	p_1	p_2	p_3	p_4
		Manna two-state model			
0	0.1	0	1	0	0
1	0.612	0.436	0.495	0.068	0.001
2	0.575	0.405	0.463	0.118	0.013
3	0.542	0.362	0.456	0.158	0.024
4	0.518	0.324	0.434	0.188	0.033
∞	0.468	0.240	0.442	0.261	0.057
		BTW four-state model			
0	0.9	0	0	0	1
1	0.252	0	0	0.033	0.967
2	0.308	0	0.012	0.726	0.262
3	0.353	0.030	0.261	0.553	0.152
4	0.388	0.090	0.357	0.437	0.116
∞	0.468	0.240	0.442	0.261	0.057

Table 2.2: The renormalization transformation for ρ and p_i for models by Manna and Bak et al. Both the sets of ρ and p_i approach to a common fixed point [L. Pietronero, A. Vespignani, and S. Zapperi (1994), Table I].

It is remarkable that the fixed point is stable under the renormalization transformation. In the model of the percolation, the critical probability p_c can be also evaluated by the technique of the renormalization group. However, the fixed point showing non-trivial fractal behaviors is unstable under the renormalization transformation. The stability of the fixed points in both the cases corresponds to the nature of the fractal behaviors. That is, the stable fixed point reflects the spontaneous fractal behavior in the self-organized criticality and the unstable fixed point represents the critical phenomena requiring the careful tuning of the control parameter.

The exponent of the power-law avalanche size distribution Eq.(2.3) is calculated from the fixed point. Since it is numerically confirmed that the fractal dimension of the individual avalanches is 2, the size distribution of the avalanches is transformed to the diameter distribution, $P(l)$, as

$$P(l) \propto l^{-1-2\tau} \quad , \tag{2.13}$$

where l denotes the diameter of the avalanche. Under the condition that an avalanche having diameter over $b^{k-1}\epsilon$ occurs, the conditional probability, K, that the avalanche diameter does not exceed $b^k\epsilon$ is expressed as

$$K = \int_{b^{k-1}\epsilon}^{b^k\epsilon} P(l)\,dl \Big/ \int_{b^{k-1}\epsilon}^{\infty} P(l)\,dl = 1 - 2^{-2\tau} \quad , \tag{2.14}$$

where ϵ denotes the lattice constant of the original model before the renormalization. The identical probability is expressed by using the fixed point probability as

$$K = \sum_{i=1}^{4} {p_i}^* (1-\rho^*)^i \quad . \tag{2.15}$$

The concrete value of Eq.(2.15) is calculated by using the numerical result in Table 2.2 as $K = 0.296$. Substituting the numerical value into Eq.(2.14), the exponent of the avalanche size distribution is estimated as

$$\tau = -\frac{1}{2}\frac{\ln(1-K)}{\ln 2} = 0.253 \quad . \tag{2.16}$$

The value shows good agreement with the numerical results.

2.2.3 Universality

In the renormalization group approach, there are the cases that originally different physical systems have an identical fixed point under a renormalization transformation. In the above example of the renormalization for the sandpile model, the probability p_i and ρ in the models by Bak et al. and by Manna approaches to an identical fixed point by repeating the renormalization transformation. The resulting fractal behaviors are also identical for both the models. In the case when several systems show an identical fractal behavior, it is said that the systems belong to the same universality class. The renormalization is a powerful technique to detect universality.

The system evolution of the sandpile models by Bak et al. and Manna is performed by the local rules. The state of a lattice site has effects on the state of the nearest neighbor sites by the local rules, and the state of the nearest neighbor sites influence the next nearest neighbor sites. In this way, although the system evolution of the sandpile models are governed by the local rules, the state of a site has a long range effect and it produces the global fractal behaviors. Such global behavior caused by the cooperation of local elements is referred to as "cooperative phenomenon".

As discussed previously in this section, the renormalization group approach treats the change of physical quantities under the coarse graining of observation scale. In a system of a cooperative phenomenon such as the sandpile models, the influence of a site is transmitted through site to site by local rules. The renormalization group approach clarifies the manner of the long range interaction observed in large scale. The universality seen in different systems means the identical manners of the long range interaction and the fractal behaviors in large observation scale.

2.3 Stable Distribution

The concept of stable distribution is closely related to the concept of fractals. In brief, the stability of a probability distribution means that the sum of the stochastic variables following an independent identical distribution again follows the distribution having similar function form as the original distribution. It is a representation of self-similarity in terms of probability theory.

2.3.1 Self-similarity in Random Walk

Let us consider a random walk process on one-dimensional space and let $x(t)$ be the position of the random walker at time t. Fig.2.3 shows an example of the trajectory of the Brownian motion. Fig.2.3(b) shows an enlargement of the part of Fig.2.3(a). The trajectories in the figures are similar to each other indicating the existence of a kind of self-similarity in the Brownian motion. However, the enlargement rates of the Fig.2.3(b) in the x-direction and in the t-direction are different. The average displacement of the Brownian motion during a period of Δt is known to follow

$$\langle x(t+\Delta t) - x(t) \rangle \ \propto \ \Delta t^{\frac{1}{2}} \quad . \tag{2.17}$$

The relation indicates that it is needed to expand a trajectory by the factor of $b^{\frac{1}{2}}$ in the x-direction when we enlarge the trajectory by a factor of b in the t-direction to confirm the self-similarity of the trajectory of the Brownian motion. Such an anisotropic self-similar object is called a "self-affine" fractal.

The trajectory of the Brownian motion in Fig.2.3(a) is actually drawn by treating four individual steps in Fig.2.3(b) as one step. Namely, the displacement in one step in Fig.2.3(a), η, is defined by the sum of the displacement in four steps in Fig.2.3(b) as

$$\eta \ = \ \sum_{i=1}^{4} \xi_i \quad , \tag{2.18}$$

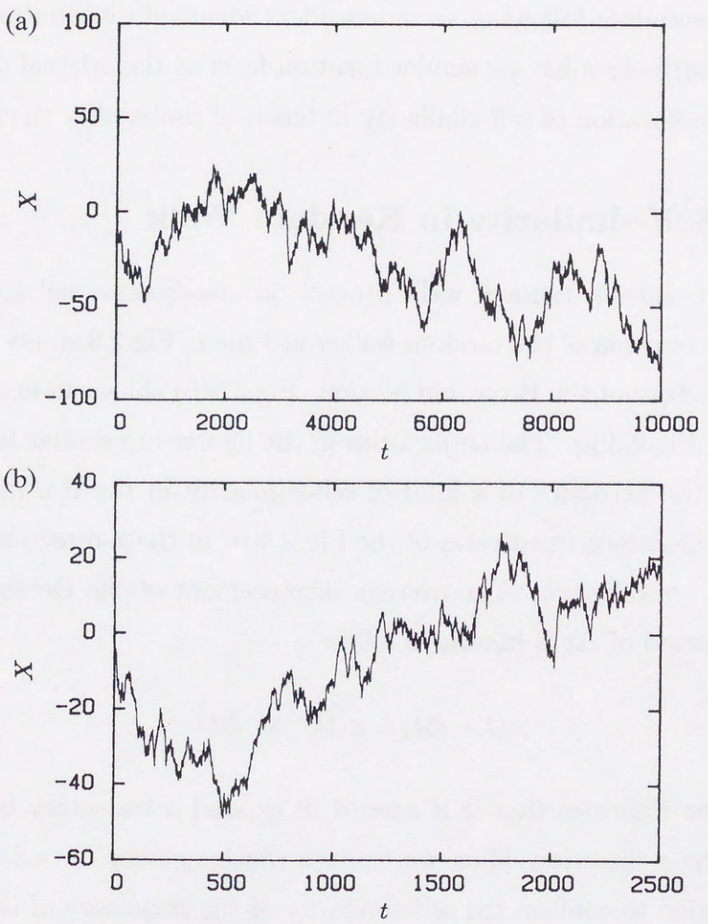

Figure 2.3: (a) A trajectory of one-dimensional Brownean motion [J. Feder (1988), Fig.9.3(b)]. (b) An enlargement of (a). The enlargement rate in the x-direction is 2 while it is 4 in the t-direction [J. Feder (1988), Fig.9.1(b)].

where ξ_i denotes the displacement by one step in Fig.2.3(b). The similarity between Figs.2.3(a) and 2.3(b) implies that the stochastic variable η follows similar distribution to that of the variable ξ. From Eq.(2.17), the variables η and ξ should follow a relation as

$$\eta \stackrel{d}{=} 4^{\frac{1}{2}}\xi \quad , \tag{2.19}$$

where $\stackrel{d}{=}$ denotes that the random variables of both sides have the same distribution. The relation shows that the stochastic variable ξ follows a stable distribution as we discuss in the following. In fact, the variable ξ follows a Gaussian distribution which is the most widely known example of stable distribution.

2.3.2 Fractal Nature of Stable Distribution

The concept of the stability of probability distribution is introduced in the framework of probability theory. The definition of stable distribution is given as follows [W. Feller (1966)]:

Let X, X_1, X_2, ..., X_n be independent stochastic variables with a common distribution P. The distribution P is stable if and only if for $Y \equiv X_1 + X_2 + \cdots + X_n$ there exist constants c_n and γ_n such that

$$Y_n \stackrel{d}{=} c_n X + \gamma_n \quad . \tag{2.20}$$

As can be seen from the definition, the stability of a distribution means that the sum of stochastic variables following an identical distribution also follows the identical distribution under a proper linear transformation.

The family of stable distribution is characterized by real parameters, α and θ, and the corresponding probability density distribution function, $P(X;\alpha,\theta)$, for $\alpha \neq 1$ is described as

$$P(X;\alpha,\theta) = \frac{1}{\pi}\,\mathrm{Re}\left[\int_0^\infty \exp\{-ixz - z^\alpha e^{\frac{i\pi}{x}\theta}\}\,dz\right] \quad , \tag{2.21}$$

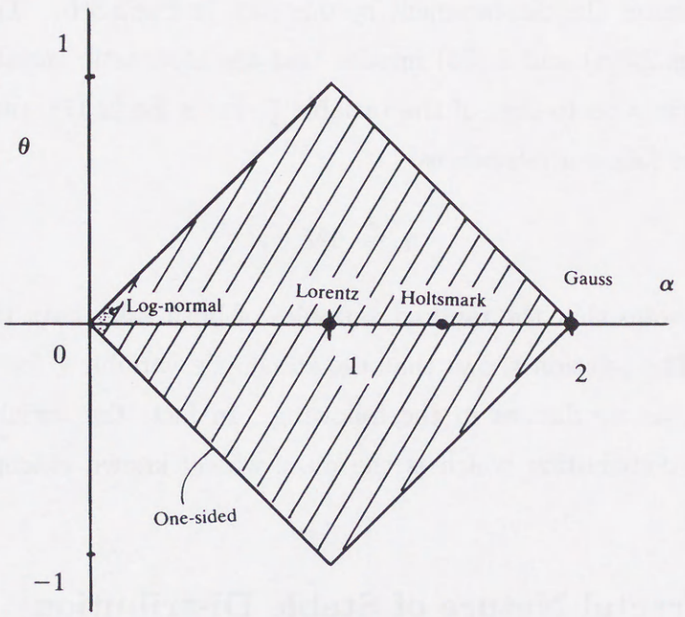

Figure 2.4: The parameter space for stable distribution [H. Takayasu (1990), Fig.5.4].

where α takes $0 < \alpha < 2$ and θ should be in the range of

$$|\theta| \leq \begin{cases} \alpha & \text{for } 0 < \alpha < 1 \\ 2 - \alpha & \text{for } 1 < \alpha < 2 \end{cases} . \tag{2.22}$$

The special cases of $(\alpha, \theta) = (1, 0)$ and $(2, 0)$ lead to Lorentzian and Gaussian distributions, respectively. The parameter range of α and θ is illustrated in Fig.2.4 showing the locations of several well known distributions. The general form of stable distribution is obtained by a linear transformation of the stochastic variable X.

The most remarkable feature of stable distribution is that they have a power-law tail where $|X|$ is sufficiently large except the case of $\alpha = 2$. The parameter α is called a "characteristic exponent". The power-law behavior of stable distribution is described in the cumulative form as

$$P(\geq X) \propto X^{-\alpha} , \tag{2.23}$$

so the characteristic exponent directly describes the power-law behavior of the distribution. The parameter θ describes the symmetry of distribution, and in the case when the distribution is asymmetric, the long tail of the distribution follows the relation Eq.(2.23).

There is a theorem more readily applicable to physical problems compared to Eq.(2.20):

Let X_r be a stochastic variable with a real parameter r. If X_r satisfies the next two relations then X_r follows a stable distribution with the characteristic exponent α:

$$X_a \stackrel{d}{=} a^{\frac{1}{\alpha}} X_1 \quad , \tag{2.24}$$

$$X_a + X_b \stackrel{d}{=} X_{a+b} \quad , \tag{2.25}$$

where X_a, X_b, and X_1 are assumed to be independent.

This theorem only treats the stochastic variable X_r which is a quantity observed in physical systems.

2.4 Minimal Model for Fractal Systems

One of the most important aims of the study of fractal systems is to clarify the causes of the fractal behaviors. Our main interest is in fractal behaviors caused by local rules, that is, the fractal behaviors by cooperative phenomena. As we discussed in Sec.2.2, it is essential for fractal behaviors by a cooperative phenomenon that the local rules cause long range interaction. Here, we should note that not all the local rules of a fractal system cause long range interaction. For example, in the case of the sandpile, the motion of each sand grain must be affected by the effect of friction between sand grains. However, the sandpile models by Bak et al. and Manna well reproduce the fractal behaviors although the models completely neglect the effect of the friction. This fact proves that the effect of the friction between sand grains is limited to short range and has no effect on the global fractal behaviors. Taking advantage of this fact, we can consider a way to clarify the essential factors for fractal behaviors using a proper model.

Let us assume that we can consider a model that includes only the essential factors for the fractal behaviors in a fractal system. In the model the short range effects are removed, so the complexity of the system must be drastically reduced. We can expect that the model reproduces the fractal behaviors since all the essential long range effects still remain in the model although the model is simplified.

Actually, it must be difficult to construct such an ideal model because we consider the situation that the essential factors for the fractal behaviors are still unknown and the purpose of the study is to clarify the essential factors. However, at least, we can pick up the rules which seems to be essential for the fractal behaviors by insight and construct a model including them. It is not guaranteed that all of the chosen effects are the essential factors of the fractal behaviors: there must be cases that some short range effects are included in

the model. In addition, when we construct such a model, we sometimes have to add some rules which are not contained in the original system for technical convenience. For example, especially in the case of a numerical model, the system is often represented by a lattice and it is inevitable that some rules to treat the quantities on the lattice are added to the model. As a result, the model includes some short range effects as well as the essential factors. Even in this case, the model must reproduce the identical fractal behaviors to the original system as far as the model does not omit any of the essential factors and as far as it does not contain any additional long range effects. It is guaranteed by the universality seen in fractal systems. On the other hand, if the model loses some essential factors or contains some additional long range effects, the fractal behaviors of the model must become different from those of the original system.

Based on the above discussion, we construct a model for a fractal system containing the effects which seems to be essential for the fractal behaviors with as little as possible of short range effects. The effects are picked up by our insight into the fractal system. If the model reproduces the fractal behaviors of the original system, we consider that the chosen effects are the essential factors for the fractal behaviors of the original system. We call the model constructed in this way a "minimal model". We can study a fractal system avoiding its complexity by using a minimal model.

Chapter 3

Laplacian Fractals

3.1 Fractality in Laplacian Fractals

"Laplacian fractals" is a term for the group of growth systems governed by some Laplace fields which spontaneously produce complex self-similar dendritic structures. One of the best studied examples of the Laplacian fractals is the model of diffusion-limited aggregation. Historically, the diffusion-limited aggregation played an important role in making many physicists recognize the significance of the concept of fractals. Here, we survey the fractal features and the growth mechanism of the Laplacian fractals.

3.1.1 Diffusion-limited Aggregation

The model of diffusion-limited aggregation was introduced to reproduce the complex dendritic pattern of the cathode deposition of positive metallic ions in weak electrolyte [T. A. Witten and L. M. Sander (1981) and (1983)]. In the model the pattern is grown by considering the aggregation process of diffusing particles. Although the model is easily generalized to the cases in higher dimensions, we only treat the two-dimensional case in the following discussion.

The model of diffusion-limited aggregation in two-dimensional space is introduced as follows:

A seed particle is put in the center of the system and another particle is launched from a place sufficiently far from the seed particle. The launched particle performs Brownian motion until it touches the seed particle making an aggregate. Then one more particle is launched from a place sufficiently far from the aggregate. It also performs the Brownian motion until it touches and sticks to the aggregate. This process is repeated until the aggregate grows to sufficient size.

The resulting cluster has complex dendritic structure as shown in Fig.3.1. We can easily recognize the fractal branching structure of the aggregate.

The fractal dimension of the cluster is estimated by observing the power-

Figure 3.1: An aggregate of the diffusion-limited aggregation of 3600 particles on a two-dimensional square lattice [T. A. Witten and L. M. Sander (1981), Fig.1].

law behavior of a density-density correlation function. The density-density correlation function describes the expectation that the two points separated by a vector $\boldsymbol{r}$ belong to the cluster. The density-density correlation function, $c(\boldsymbol{r})$, for an aggregate S is defined as

$$c(\boldsymbol{r}) \equiv \frac{1}{V}\sum_{\boldsymbol{r}'}\rho(\boldsymbol{r}+\boldsymbol{r}')\rho(\boldsymbol{r}') \quad , \tag{3.1}$$

where V denotes the total number of the particles contained in S and $\rho(\boldsymbol{r})$ is a density function defined as

$$\rho(\boldsymbol{r}) \equiv \begin{cases} 1 & \text{for } \boldsymbol{r} \in S \\ 0 & \text{for } \boldsymbol{r} \notin S \end{cases} \quad . \tag{3.2}$$

In the case of the diffusion-limited aggregation, S is isotropic and $c(\boldsymbol{r})$ is simply a function of $r = |\boldsymbol{r}|$. As shown in Fig.3.2, the density-density correlation function $c(r)$ shows a power-law decay,

$$c(r) \propto r^{-\alpha} \quad . \tag{3.3}$$

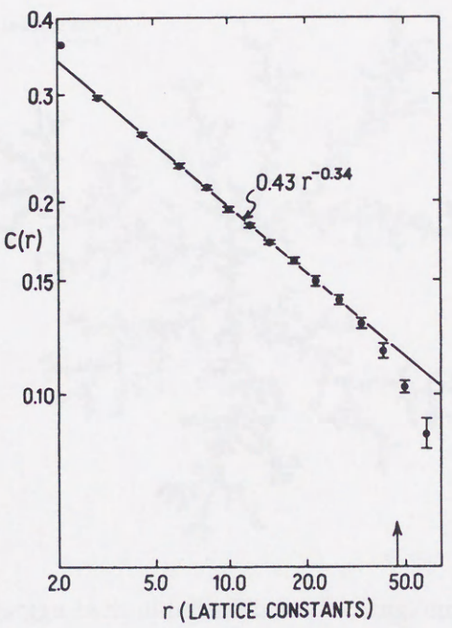

Figure 3.2: The density-density correlation function of diffusion-limited aggregates as a function of distance measured in lattice constants. The arrow marks the average radius of gyration [T. A. Witten and L. M. Sander (1983), Fig.3].

By integrating the density-density correlation function within distance r, the average number of the particles within the range r, $N(r)$, is obtained as

$$N(r) \propto \int_{|\boldsymbol{r}'|\leq r} c(\boldsymbol{r}')\, d\boldsymbol{r}' \propto r^{d-\alpha} \quad , \tag{3.4}$$

where d and $d\boldsymbol{r}'$ denote the embedding space dimension of the aggregate and the volume element of d-dimensional space, respectively. The relation Eq.(3.4) describes the relation between fractal dimension, D, and the exponent α as

$$D = d - \alpha \quad . \tag{3.5}$$

By numerical results, the exponent α for the clusters in two-dimensional diffusion-limited aggregation is estimated as $\alpha \simeq 0.3$ which leads to the fractal dimension $D \simeq 1.7$ [T. Vicsek (1989)].

3.1.2 Scaling Relation in Diffusion-limited Growth

We consider a variation of the model of the diffusion-limited aggregation by replacing the seed particle by a set of seed particles forming a straight line, a line seed. This case of the diffusion-limited growth starting from a line seed is called diffusion-limited deposition. An example of the pattern formed by the diffusion-limited deposition is shown in Fig.3.3. In the case of the diffusion-limited deposition, the system forms tree-like structures. We define clusters as the individual "trees" connected to their respective seed particles and introduce cluster size as the number of the aggregated particles contained in the individual tree. By the result of large scale simulation shown in Fig.3.4, it was found that the cluster size distribution has a power-law tail as

$$P(\geq s) \propto s^{-\tau} \quad , \tag{3.6}$$

where s denotes the cluster size and the value of the exponent was estimated as $\tau = 0.55$ [P. Meakin (1984)].

The infinite power-law tail of the cluster size distribution Eq.(3.6) should be

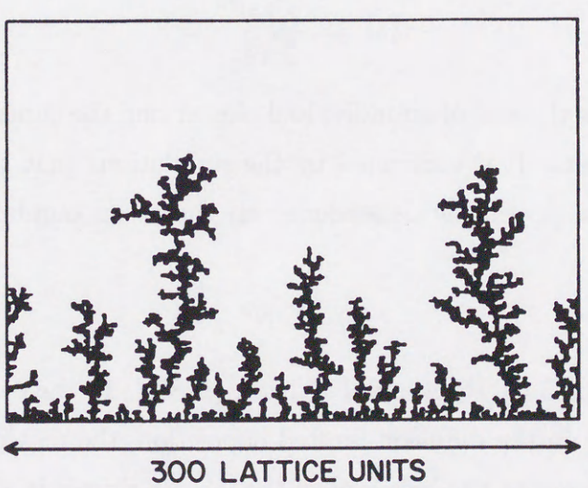

Figure 3.3: Branches by the diffusion-limited deposition process starting from a line seed [P. Meakin (1983), Fig.3].

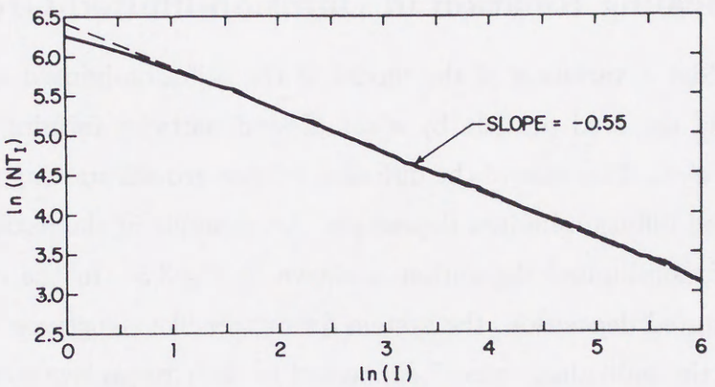

Figure 3.4: The cumulative cluster size distribution by the two-dimensional diffusion-limited deposition [P. Meakin (1984), Fig.1].

observed in the idealized case that the aggregation process of diffusing particles is infinitely repeated. In real systems, the number of aggregated particles is limited and the cluster size distribution has a cutoff at a certain finite size.

Let us consider a system after depositing N particles per one seed particle. We define mean cluster size, $\langle s \rangle$, as

$$\langle s \rangle \equiv \frac{\sum_i {s_i}^2}{\sum_i s_i} \quad , \tag{3.7}$$

where s_i denotes the size of an individual cluster and the sums run over all the individual clusters. It is confirmed by the simulations that the mean cluster size $\langle s \rangle$ shows a power-law dependence on the mean number of aggregated particles N as

$$\langle s \rangle \propto N^z \tag{3.8}$$

as shown in Fig.3.5 [Z. Rácz and T. Vicsek (1983)]. In the case of the cluster size distribution in the diffusion-limited deposition, the mean cluster size has a tendency to describe the behavior of the largest cluster in the system. This means that the cutoff of the cluster size distribution must appear around the mean cluster size. Considering the existence of the cutoff, the cumulative

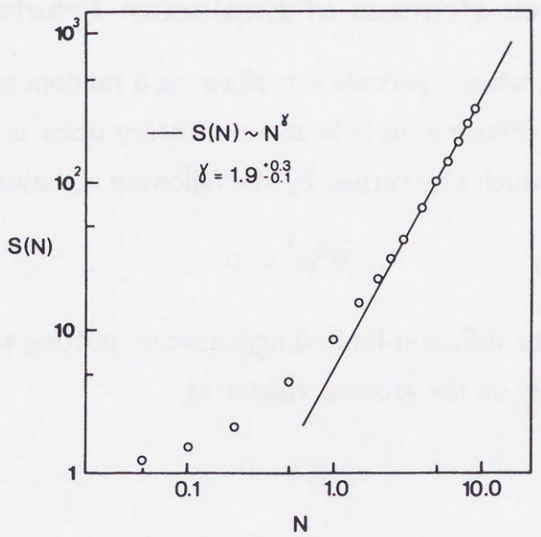

Figure 3.5: The dependence of the mean cluster size on the number of the aggregated particles [Z. Rácz and T. Vicsek (1983), Fig.2].

cluster size distribution function, $P_N(\geq s)$, is assumed to be written as

$$P_N(\geq s) \;\propto\; s^{-\tau} f(s/N^z) \tag{3.9}$$

using a cutoff function, $f(x)$, defined as

$$f(x) \;\simeq\; \begin{cases} 1 & \text{for } x \ll 1 \\ 0 & \text{for } x \gg 1 \end{cases} \quad . \tag{3.10}$$

Using Eq.(3.9), we obtain

$$N \;\propto\; \int_0^\infty s^{1-(\tau+1)} f(s/N^z)\, ds \;\propto\; N^{(1-\tau)z} \tag{3.11}$$

since the expectation of the cluster size s should be proportional to the number of the aggregated particles. The relation Eq.(3.11) leads to the following scaling law:

$$(1-\tau)z \;=\; 1 \tag{3.12}$$

[Z. Rácz and T. Vicsek (1983)].

3.1.3 Growth Process of Laplacian Fractals

In the situation when a particle is performing a random walk, the probability of finding the diffusing particle at an arbitrary point is proportional to a Laplace field, ϕ, which is governed by the following equation:

$$\nabla^2 \phi = 0 \quad . \tag{3.13}$$

In the model of the diffusion-limited aggregation, putting the boundary condition for Eq.(3.13) on the growing cluster as

$$\phi = 0 \tag{3.14}$$

and on the system edge placed sufficiently far from the cluster as

$$\phi = 1 \quad , \tag{3.15}$$

the probability that the diffusing particle reaches to an arbitrary point on the growing cluster surface is proportional to the gradient of the probability field ϕ. It means that the growth probability of the cluster at the cluster surface point $\boldsymbol{r}$, $p(\boldsymbol{r})$, follows

$$p(\boldsymbol{r}) \propto |\nabla \phi| \quad . \tag{3.16}$$

Thus the growth process of the diffusion-limited aggregation is governed by a Laplace field surrounding the growing cluster and, therefore, it is classified as a kind of Laplacian fractals.

There are several fractal growth processes classified as Laplacian fractals besides the diffusion-limited aggregation. For examples, electrode deposition [M. Matsushita, M. Sano, Y. Hayakawa, H. Honjo, and Y. Sawada (1984)], dielectric breakdown [L. Niemeyer, L. Pietronero, and H. J. Wiesmann (1984)], crystallization [Gy. Radnoczi, T. Vicsek, L. M. Sander, and D. Grier (1987)], viscous fingering [G. Daccord, J. Nittmann, and H. E. Stanley (1986)], chemical dissolution [G. Daccord (1987)], and bacterial growth [H. Fujikawa and M.

Matsushita (1989)] are also known to show the Laplacian growth aspects. Each of these systems includes a Laplace field as a governor of the growth rules. For example, in the case of the electrode deposition, the Laplace field is an electric potential field. In the case of the diffusion-limited aggregation, the Laplace field surrounding the growing cluster governs the growth process through the growth probability described by Eq.(3.16). By Eq.(3.16) the growth velocity of the cluster at a surface point $\boldsymbol{r}$, $\boldsymbol{v}(\boldsymbol{r})$, is also proportional to the gradient of the Laplace field at the surface point on the average. That is,

$$\boldsymbol{v}(\boldsymbol{r}) \propto \nabla\phi \tag{3.17}$$

holds besides Eq.(3.16). For example, the growth velocity of the viscous fingering is described by Eq.(3.17).

The patterns formed by these Laplacian growth systems are similar each other and the fractal dimensions D of the patterns are all found around $D \simeq 1.7$. They are believed to belong to the same universality class to that of the diffusion-limited aggregation.

3.1.4 Competitive Aspect in Laplacian Fractals

It is now intuitively recognized that one of the important factors leading to the fractal behaviors in the Laplacian fractals is competition between the branches of the growing clusters.

The interface of growing phase in Laplacian fractals shows instability to fluctuation. The situation is schematically illustrated in Fig.3.6. We introduce a flux density field by the gradient of the Laplace field ϕ surrounding the growing clusters. In the condition that ϕ on the growing phase is kept a constant, the flux density field around a protrusion of the growing phase becomes more intensive compared to other interface points. The concentration of the flux results faster growth of the protrusion because of Eq.(3.16) or Eq.(3.17) and the growth of the protrusion results further concentration of the flux. Thus

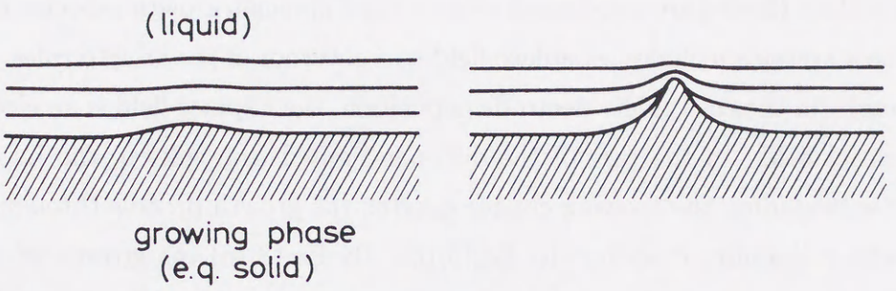

Figure 3.6: A schematic illustration of the interface instability. The shaded part shows the growing phase and the lines near the growing interface show contour lines of the Laplace field ϕ. In the picture the growing and medium phases are noted as solid and liquid phases, respectively, as in the system of electrode deposition [T. Vicsek (1989), Fig.9.1].

the interface fluctuation of the growing phase grows increasingly.

The interface instability of the growing phase causes the competition between the growing clusters. Let us consider the case of the diffusion-limited deposition. As mentioned above, the flux surrounding the clusters has a nature to concentrate on relatively protrusive places of clusters, taller trees. Thus initially larger trees can get more intensive flux and grow faster than the other clusters. On the other hand, initially smaller trees finally stop growing because almost all the flux is caught by the neighboring larger trees. This phenomenon is referred to as "shield effect". In this way, the clusters in the Laplacian growth systems are under competition for the flux, and the competition separates the clusters into growing and shielded parts.

The competition between the clusters in Laplacian growth systems such as the diffusion-limited deposition continues throughout all evolution stages. At a certain evolution stage of a Laplacian growth system, there are growing trees having large enough size to catch the flux. However, not all of the growing trees can continue to grow. As the evolution proceeds, even such relatively large growing trees are separated into the part continuing to grow and the part

shielded by the neighboring growing trees. The size of the emerging shielded trees becomes larger as the evolution proceeds. As a result, the shielded trees having various size are produced forming a power-law cluster size distribution.

3.2 Minimal Competitive Growth Model

As discussed in the previous section, one of the essential factors for the power-law cluster size distribution observed in Laplacian fractals is intuitively believed to be the competitive growth process of the clusters. To confirm the speculation, we apply the concept of the minimal model introduced in Sec.2.4. It is confirmed that the model imitating the competitive growth process seen in Laplacian fractals reproduce the power-law size distribution of the growing elements [H. Inaoka (1993)].

3.2.1 Basic Concept of the Model

Let us consider a two-dimensional line-seed Laplacian growth system as illustrated in Fig.3.7. Obviously, the system has anisotropy in the growth direction. The growth occurs in the direction from the bottom to the top in

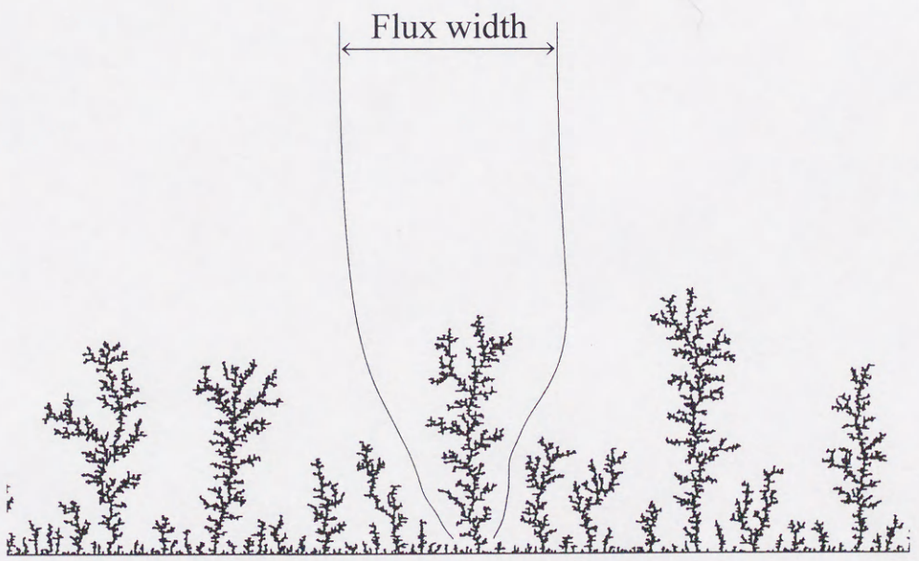

Figure 3.7: A schematic picture for the definition of the flux width. By tracing the flux from a cluster to the upper edge of the system, the flux width for the cluster is determined.

the figure. In the system, each cluster grows detecting the flux surrounding the cluster and its growth rate is proportional to the intensity of the flux. So the cluster size is proportional to the integration of the flux intensity which has been detected by the cluster.

Here, if the system size is large enough in the growth direction, the flux density field far from the growing clusters can be regarded to be uniform. We consider to trace the flux from an arbitrary cluster to the uniform flux density region. Focusing on the bunch of flux which is connected to an arbitrary chosen cluster, the width of the flux for the chosen cluster can be determined at the uniform flux density region as illustrated in Fig.3.7. Since the intensity of the flux detected by the chosen cluster is conserved during the propagation of the flux between the cluster and the upper edge, the growth rate of the cluster should proportional to the flux width at the uniform flux density region. Determining such flux widths for all the individual clusters in the system, the summation of the flux widths over the clusters should be equal to the system width. This fact means that the total amount of the source of the cluster growth is limited. In the system the larger clusters can catch more intensive flux: they have wider flux and grows faster. As a result, most of the flux is taken by the larger clusters and, therefore, the smaller clusters can hardly get the flux and stop growing because of the shield effect. Thus we can interpret the two-dimensional Laplacian growth systems as a cluster growth systems with competition for the uniform flux density field.

3.2.2 Model Description

The model mainly includes two ingredients: a set of growing mass points and an one-dimensional flux source, as illustrated in Fig.3.8. These correspond to the growing clusters and the uniform flux density field far form the clusters in Laplacian growth systems, respectively. The mass of each mass point represents the cluster size in Laplacian growth systems. The mass points are

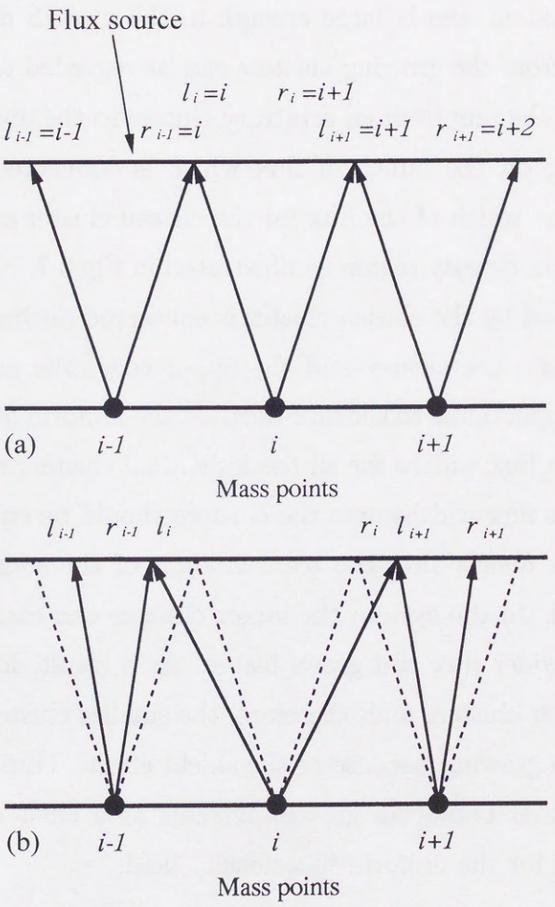

Figure 3.8: (a) The initial condition of the model. Each point has flux source of unit length. (b) The boundaries are moved and the flux source is competed for [H. Inaoka (1993), Fig.1].

on a straight line at regular unit intervals. The unit length flux source is assigned to each mass point initially. For example, for the i-th mass point, the locations of left and right boundaries, l_i and r_i, are set to $l_i = i$ and $r_i = i+1$, respectively. The total length of flux source is equal to the number of mass points, or system size. Initially, the mass of each mass point is assigned by a uniform random number in the range of $[1.0, 1.1)$.

The system is evolved by repeating the following procedures:

1. *Expansion of the flux width.* We should note that the competing dynamics for the flux may be similar throughout all evolution stages in real Laplacian growth systems. Therefore, it is assumed that the expansion rate for the flux width is proportional to the α-th power of mass, where α is a constant. Then the boundaries of the i-th mass point are moved by the following rules as

$$\begin{cases} l_i & \to & l_i - C({m_i}^\alpha - {m_l}^\alpha) \\ r_i & \to & r_i + C({m_i}^\alpha - {m_r}^\alpha) \end{cases} , \tag{3.18}$$

   where C is a constant and m_l and m_r denote the left and right neighbor mass of the i-th mass point, respectively.

2. *Removing the shielded mass point.* In the procedure 1, if the boundaries becomes $l_i \geq r_i$, the mass point is removed from the procedures and stops growing. The removed mass point corresponds to the shielded clusters in Laplacian growth.

3. *Growth of the mass.* Each mass point grows its mass with the source region width as

$$m_i \to m_i + \rho(r_i - l_i) \quad . \tag{3.19}$$

   Here, ρ denotes the density of the flux source.

These procedures make one time step.

The constants used in the following discussion are $C = 0.3$ and -0.3 for the cases $\alpha > 0$ and $\alpha < 0$, respectively, and $\rho = 0.1$.

3.2.3 Simulation Results

In Fig.3.9, an example of the time evolution of the system in the case of $\alpha = 0.3$ is illustrated. The figure shows a time evolution of the configuration of the source boundaries on the one-dimensional flux source. The curves in the figure which separate the space-time are the trajectories of the source boundaries. As can be seen from the figure, the trajectories draw a self-affine domain set in the space-time. Since the mass of the mass point is the integration of the flux width with time, the area of each domain represents the mass of the mass point which belongs to the domain. The self-affine configuration of the domains implies a power-law mass distribution.

Fig.3.10 is a result in the case of $\alpha = 0.3$. The points in log-log scale are on a straight line ranging from 10 to 10^5 indicating that the cumulative mass distribution by the model follows a power law as

$$P(\geq m) \propto m^{-\tau} \quad , \tag{3.20}$$

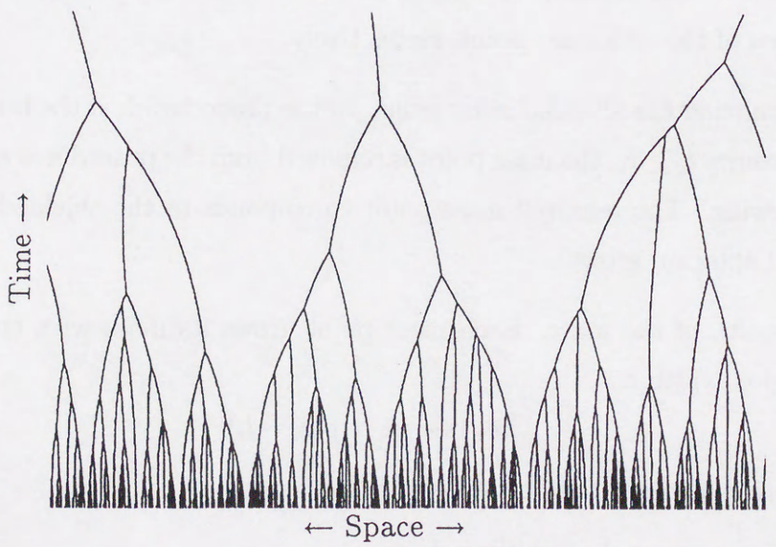

Figure 3.9: Trajectories of the source boundaries in the case of $\alpha = 0.3$ [H. Inaoka (1993), Fig.2].

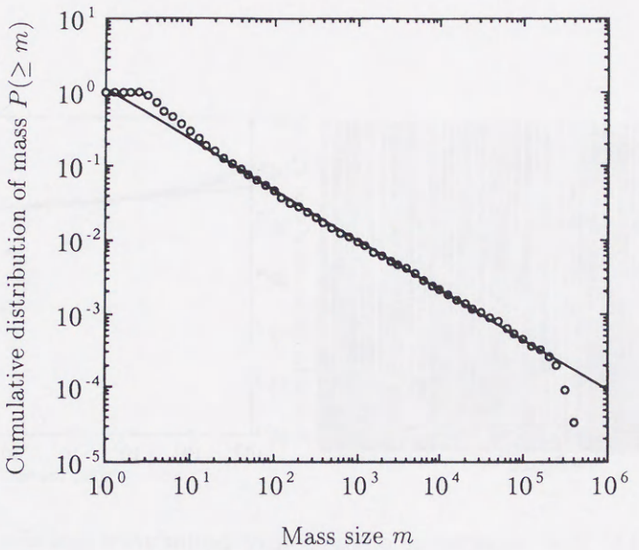

Figure 3.10: The cumulative distribution of the particle mass in log-log scale. The line shows a power-law distribution as $P(\geq m) \propto m^{-0.68}$ [H. Inaoka (1993), Fig.3].

where m denotes the mass. The power-law behavior of the mass distribution seems to be observed around the parameter range $-0.5 < \alpha < 1.0$. In the parameter ranges $\alpha < -0.5$ and $\alpha > 1.0$, it seems that the mass distribution loses the power-law behavior although, formally, we can estimate the exponent of the distribution, τ. In the range of $\alpha < -0.5$, the competitive process of the model seems ineffective. So the domain shape on the space-time is quite elongated and the cumulative mass distribution has a flat form as shown in Fig.3.11. On the contrary to the case of $\alpha < -0.5$, in the case of $\alpha > 1.0$, the competitive process is too intense and the system soon reaches the state that only one mass point is growing as seen in Fig.3.12.

We plot the dependence of the exponent of the cumulative mass distribution τ on the parameter α in Fig.3.13. It can be easily seen from Fig.3.13 that a simple linear relation holds between α and τ in the range of $-0.5 < \alpha < 1.0$, the fractal parameter range. In the range $\alpha < -0.5$ and $\alpha > 1.0$, the points

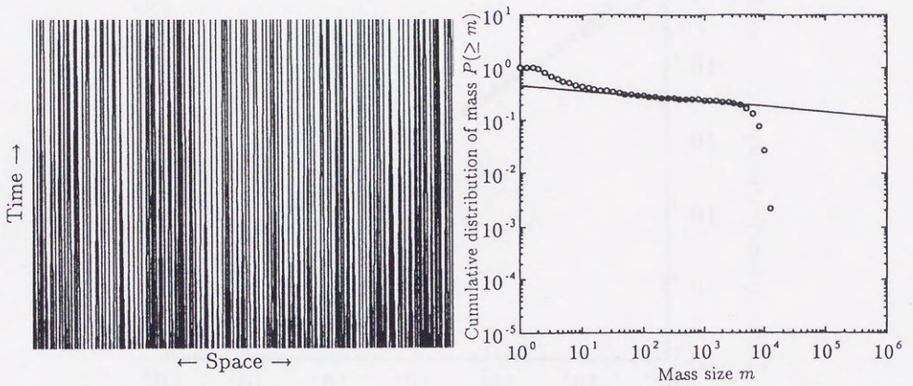

Figure 3.11: The trajectories of the source boundaries and the cumulative mass distribution in log-log scale in the case of $\alpha = -1.2$.

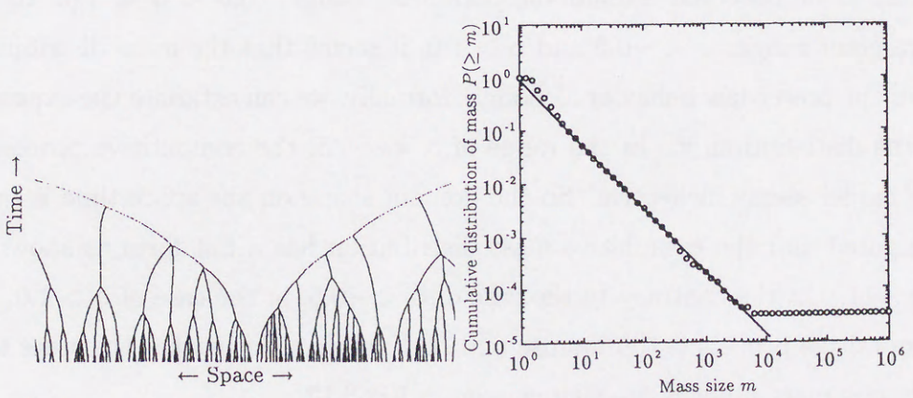

Figure 3.12: The trajectories of the source boundaries and the cumulative mass distribution in log-log scale in the case of $\alpha = 1.2$.

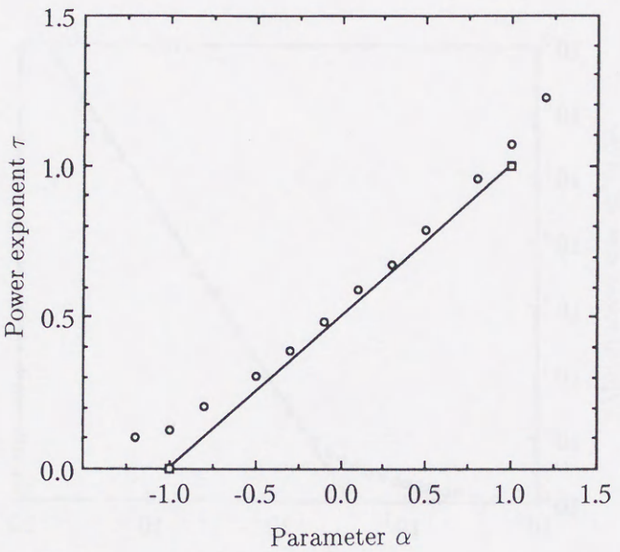

Figure 3.13: The relation between the exponent τ and the parameter α. The line shows the slope of $\tau = \frac{1+\alpha}{2}$ [H. Inaoka (1993), Fig.4].

deviate from the line. As shown above, the system does not show the fractal behavior in these ranges.

In the model of the diffusion-limited aggregation, the mean cluster size shows a power-law relation with the number of the aggregated particles as Eq.(3.8). We define typical mass, $\langle m \rangle$, for the model in the similar way to Eq.(3.7) as

$$\langle m \rangle \equiv \frac{\sum_i {m_i}^{r+1}}{\sum_i {m_i}^r} \quad , \tag{3.21}$$

where r is a positive constant. The typical mass describes the behavior of the largest mass in the system in the limit of $r \to \infty$. We use $r = 3$ in the simulation. In the fractal parameter range $-0.5 < \alpha < 1.0$, the typical mass $\langle m \rangle$ is also expected to show power-law relation with time. One of the numerical result is shown in Fig.3.14 in log-log scale. At the starting stage of the simulation, the competitive process for the flux source is ineffective. Around the stage just before 10^2 time steps, the competition becomes effective

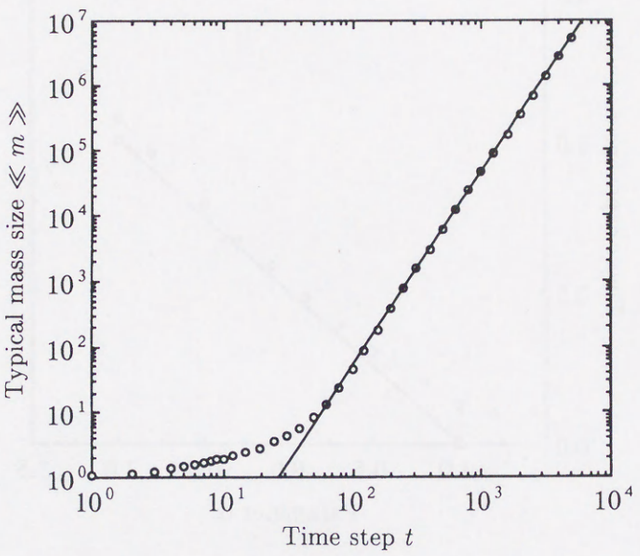

Figure 3.14: The time evolution of the typical mass for $\alpha = 0.3$. The line shows a power-law expansion as $\langle m \rangle \propto t^{2.98}$ [H. Inaoka (1993), Fig.5].

α	τ	z
1.2	1.23	18.98
1.0	1.07	10.88
0.8	0.96	6.45
0.5	0.79	3.99
0.3	0.68	2.98
0.1	0.59	2.41
−0.1	0.49	2.04
−0.3	0.39	1.75
−0.5	0.31	1.56
−0.8	0.21	1.37
−1.0	0.13	1.25
−1.2	0.10	1.22

Table 3.15: The values of τ and z for various α [H. Inaoka (1993), Table 1].

and the typical mass $\langle m \rangle$ shows a power-law expansion as

$$\langle m \rangle \propto t^z \quad , \tag{3.22}$$

where t denotes the time step.

The values of τ and z for various values of the parameter α are collectively shown in Table 3.15. In the case of $\alpha < -0.5$, the values of z are relatively close to 1. It means that the competitive process is not so effective and the mass points in the system have a tendency to grow with time. On the contrary, in the case of $\alpha > 1.0$, $\langle m \rangle$ seems to grow exponentially or diverge in a finite time because of the intensive competition, and the system does not show the fractal property.

3.2.4 Scaling Relation

Here, we introduce a scaling relation to describe the behavior of the model.

We assume that the behavior of the model can be grasped by investigating the behavior of the heaviest particle in the model. The continuous version of the evolving procedure of the model is described by the set of differential equations as

$$\frac{dw_i}{dt} = C\{({m_i}^\alpha - {m_r}^\alpha) + ({m_i}^\alpha - {m_l}^\alpha)\} \quad , \tag{3.23}$$

$$\frac{dm_i}{dt} = \rho w_i \quad , \tag{3.24}$$

where w_i denotes the flux width of i-th mass, $r_i - l_i$. If the particle i is the heaviest one in the model and the effect of other particles are neglected, the equations Eqs.(3.23) and (3.24) becomes

$$\frac{d^2m}{dt^2} = 2C\rho m^\alpha \quad , \tag{3.25}$$

where the index i is removed for simplicity.

From Eq.(3.25), we obtain the solutions for the case $0 < \alpha < 1$ as

$$m = c_2(c_3 + t)^{\frac{2}{1-\alpha}} \tag{3.26}$$

and for the case $\alpha > 1$ as

$$m = c_2(c_3 - t)^{\frac{2}{1-\alpha}} \quad . \tag{3.27}$$

In Eqs.(3.26) and (3.27), $c_2 = \{\frac{(1-\alpha)^2}{1+\alpha}\}^{\frac{1}{1-\alpha}}$ and c_3 should be positive by a mathematical restriction. As for the case of $\alpha < 0$, there is no analytical solution except for rare special cases. In the special case of $\alpha = 1$, the exponential behavior of the mass is easily confirmed.

From Eq.(3.27), in the case of $\alpha > 1$, it is shown that the mass of the heaviest point diverges in a finite time c_3, which agrees with the simulation result. Eq.(3.26) shows a power-law expansion of the mass of the heaviest mass point in the case of $0 < \alpha < 1$. If the mass of the heaviest mass point is sufficiently larger than those of the other mass points, the theoretical exponent $\frac{2}{1-\alpha}$ can be interpreted as the exponent of the typical mass size expansion z by the simulation. Since the model imitates the growth process of Laplacian fractals, the scaling relation Eq.(3.12) must also hold in this case. Using the scaling relation Eq.(3.12), we obtain a simple linear relation between α and τ as

$$\tau = \frac{1+\alpha}{2} \quad . \tag{3.28}$$

The result is shown in Fig.3.13 by a solid line. The dots are roughly on the line indicating the reasonable success of the scaling approach. The line fits the simulation results in the entire fractal region of the parameter range $-0.5 < \alpha < 1$ while the analytical solution of Eq.(3.25) is given only in the range $\alpha > 0$.

Chapter 4
River Networks

4.1 Fractal Nature of River Networks

The patterns of river networks are the intuitively most easily understandable fractal structures and they are often introduced as an example of the fractal geometries. Fig.4.1 is a photograph of stream branches taken by a satellite [K. W. Kelley (1988)]. At first glance of the picture we can easily recognize that the whole stream consists of smaller branch streams similar to the whole stream, and the branch streams again consist of even smaller similar branch streams. In this way, river networks make complex nesting structures. Geomorphologists recognized the self-similarity long before the recognition of the concept of fractals and many standard text books of geomorphology mention it [for example, A. E. Scheidegger (1961)]. The description of the self-similarity of river networks is related to the interpretation of so-called Horton's laws, which are experiential laws for the structure of stream branches. Related to the concept of fractals, a nontrivial power-law behavior known as Hack's law

Figure 4.1: Hadhramaut plateau, South Yemen [K. W. Kelley (1988), Plate 84].

and the power-law distribution of drainage-basin area are also confirmed in field data.

4.1.1 Drainage-basin Area Distribution

The self-similarity of river networks implies a power-law size distribution of stream branches similar to that seen in Laplacian fractals discussed in Sec.3.1. Note that the size of a stream branch corresponds to the drainage-basin area of the stream in the case of the river networks. Rodríguez-Iturbe et al. examine the drainage-basin area distribution of five river networks in north America using digital elevation maps [I. Rodríguez-Iturbe, E. J. Ijjász-Vásquez, R. L. Bras, and D. G. Tarboton (1992)]. The digital elevation map is a set of elevation data measured on pixels of a square lattice covering a map. By assigning each lattice site a drainage direction which is directed to the lowest nearest

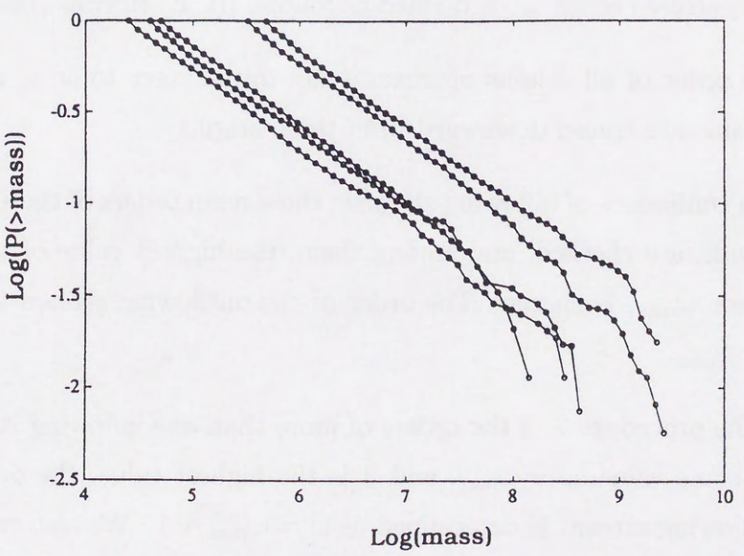

Figure 4.2: The cumulative distribution of the drainage-basin area in five different basins [I. Rodríguez-Iturbe, E. J. Ijjász-Vásquez, R. L. Bras, and D. G. Tarboton (1992), Fig.3].

neighbor lattice site, branch structures representing the river networks are obtained (see also Fig.4.10). The drainage-basin area of an arbitrary chosen site is determined by the number of upstream sites connected to the chosen site. They found that the drainage-basin area measured by the number of the sites, n, follows a power-law distribution as

$$P(\geq n) \propto n^{-\tau} \tag{4.1}$$

with the exponent in the range of $\tau = 0.41 - 0.44$ as shown in Fig.4.2.

4.1.2 Horton's Laws

To introduce Horton's laws, we have to determine stream order which classifies individual streams in a network. There are several definitions of the stream order. Since Horton's and Strahler's stream orders are most suitable for the discussion of the Horton's laws, we introduce these two stream orders.

Horton's stream order, ω, is defined as follows [R. E. Horton (1945)]:

1. The order of all origins of streams are initially set to $\omega = 1$, and the streams are traced downward from these origins.

2. At a confluence of inflowing streams, the stream orders of these inflowing streams are checked, and among them, the highest value of the stream orders, $\omega_{\max}$, is chosen. The order of the outflowing stream is given as $\omega = \omega_{\max}$.

3. In the procedure 2, if the orders of more than one inflowing streams are the same value, $\omega = \omega_{\max}$, and it is the highest value, the order of the outflowing stream is determined as $\omega = \omega_{\max} + 1$. We also re-label the order of the longer inflowing stream as $\omega = \omega_{\max} + 1$ from the confluence to the origin.

4. The tracing is continued until it reaches the mouth of the river.

By the procedure 3 we can easily find the main stream of the stream network because the main stream has the highest order when the ordering is finished. This is the advantage of the method, however, performing the procedure 3 is rather elaborate especially when we perform the analysis of field data. Strahler's stream order is introduced to reduce such trouble [A. N. Strahler (1952)]. The difference between these two stream orders is that the Strahler's stream order does not determine the main stream. That is, the procedure 3 is replaced by the following one:

3. At a confluence of streams, when more than one inflowing streams have the maximum order $\omega_{\max}$, we only fix the stream order of the outflowing stream as $\omega = \omega_{\max} + 1$.

The resulting classification by these two stream ordering is shown in Fig.4.3.

Classifying a river network by Horton's stream order, the number of ω-order streams, N_ω, is counted and the average length of ω-order streams, L_ω,

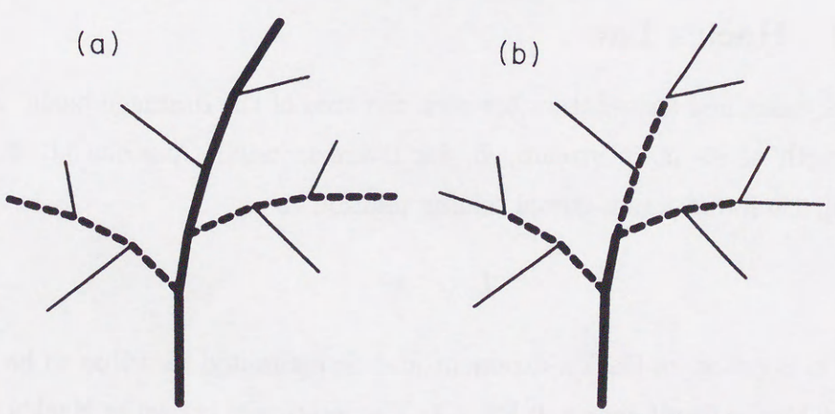

Figure 4.3: The stream orders determined in two different ways for the same stream network [H. Inaoka and H. Takayasu (1993), Fig.9]: (a) Horton's stream order and (b) Strahler's stream order. The fine lines, dashed lines, and bold lines show first-, second-, and third-order streams, respectively.

is measured. Horton's laws state that the ratios,

$$N_\omega / N_{\omega+1} = R_B \quad , \tag{4.2}$$

$$L_{\omega+1} / L_\omega = R_L \quad , \tag{4.3}$$

are independent of ω [R. E. Horton (1945)]. The constants R_B and R_L are called bifurcation ratio and stream-length ratio, respectively. It is known that the Horton's stream order in the definition of the Horton's laws can be replaced by the Strahler's stream order [A. E. Scheidegger (1968a) and (1968b)].

These laws have simple physical meaning. Interpreting these laws, an ω-order stream has R_B $(\omega - 1)$-order streams as branches and the length of the branches is reduced by a factor of $\frac{1}{R_L}$ from the length of the ω-order stream on the average. Therefore, the validity of the relations Eqs.(4.2) and (4.3) on any ω-order streams means the statistical self-similarity of the river network. Real river networks well satisfy the Horton's laws and the bifurcation ratio and the stream-length ratio are known to be in the ranges $R_B = 2 - 6$ and $R_L = 1.5 - 3.5$, respectively [P. La Barbera and R. Rosso (1989)].

4.1.3 Hack's Law

Hack examined the relation between the area of the drainage basin, A, and the length of its main stream, L, for rivers in north America [J. T. Hack (1957)]. He found a non-trivial scaling relation as

$$L \propto A^\alpha \quad , \tag{4.4}$$

where α is called as Hack's exponent and he estimated its value to be about $\alpha \simeq 0.6$ by the result shown in Fig.4.4. The relation is known as Hack's law. If the shapes of the river basins are similar each other and the fractal dimension of the main stream is 1, we expect a usual relation as

$$L \propto A^{\frac{1}{2}} \quad . \tag{4.5}$$

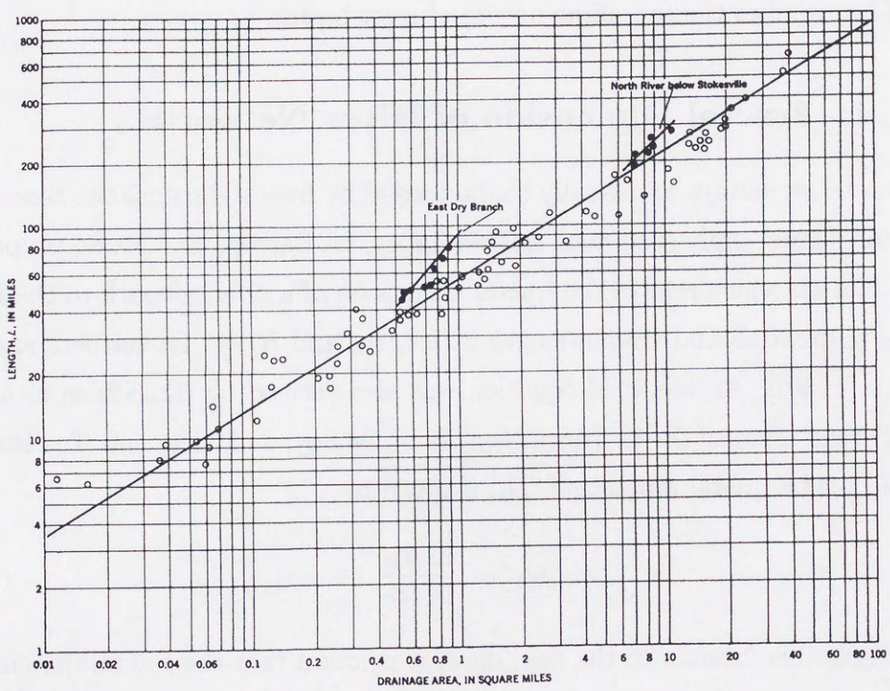

Figure 4.4: A logarithmic scatter diagram showing the relation between the main stream length and the drainage-basin area in field data [J. T. Hack (1957), Fig.25].

Therefore, the non-trivial relation Eq.(4.4) implies a fractal behavior of river basins. Mandelbrot showed from the relation Eq.(4.4) that the fractal dimension of main streams should be $2\alpha \simeq 1.2$ assuming the similarity of the shape of river basins [B. B. Mandelbrot (1982)]. However, the similarity of the basin shapes is doubtful. In fact, Hack mentioned in his paper that the relatively larger basins have more elongated shapes [J. T. Hack (1957)]. The Hack's law Eq.(4.4) implies the self-affine nature of river basins.

4.1.4 Fractal Dimension of River Networks

Fractal structures are usually characterized by fractal dimensions. Since the Horton's laws imply statistical self-similarity, La Barbera and Rosso proposed an equation which relates the fractal dimension of a river network to the Horton's bifurcation and stream-length ratios, R_B and R_L [P. La Barbera and R. Rosso (1989)]. An identical equation was also derived by Hinrichsen et al. in a different manner [E. L. Hinrichsen, K. J. Måløy, J. Feder, and T. Jøssang (1989)]. The fractal dimension, D_s, is given by

$$D_s = \frac{\ln R_B}{\ln R_L} \quad . \tag{4.6}$$

Applying this formula to the field data, it is found that the fractal dimension lies between 1.5 and 2.0 with the average $D_s = 1.6 - 1.7$ (Fig.4.5). Takayasu also proposed another relation to calculate the fractal dimension of a branching geometry, D_τ, using the exponent of the power-law branch size distribution τ [H. Takayasu (1988)]. The relation is

$$D_\tau = \frac{1}{1-\tau} \quad . \tag{4.7}$$

Substituting the exponent of the power-law drainage-basin area distribution from the field data into the equation, the range of the fractal dimension is estimated as $D_\tau = 1.69 - 1.79$.

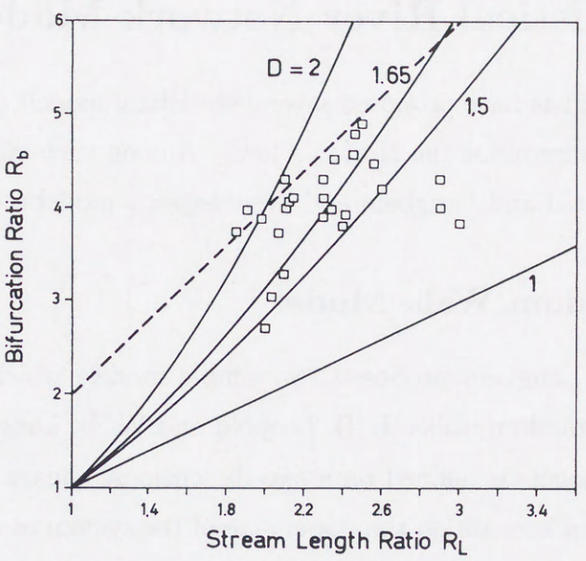

Figure 4.5: A plot of the field data R_L versus R_B. The solid curves indicate the fractal dimension by $D_s = \ln R_B / \ln R_L$ [P. La Barbera and R. Rosso (1989), Fig.5].

On the other hand, Tarboton et al. insisted that the fractal dimension of river networks must be 2, which is the dimension of the space-filling geometry in two-dimensional space [D. G. Tarboton, R. L. Bras, and I. Rodriguez-Iturbe (1988) and (1990)]. The reason is that rain water falling on earth's surface flows to join river streams wherever the rain water falls unless there is a stagnancy region of the water, which means that the whole earth's surface belongs to the river networks.

The cause of the inconsistency may also due to the self-affine nature of river networks. In general, fractal dimension is meaningful only in the case that self-similarity is guaranteed.

4.2 Statistical River Network Models

Geomorphologists have proposed several statistical models of river networks to numerically reproduce the Horton's laws. Among such statistical models, models by Leopold and Langbein and Scheidegger's model are well-known.

4.2.1 Random Walk Model

Leopold and Langbein proposed two simple models which generate river networks using random walks [L. B. Leopold and W. B. Langbein (1962)].

One of the models is defined on a two-dimensional square lattice and, initially, random walkers are on the upper side of the system at regular intervals representing the origins of streams. Each of the random walkers moves to its down-left, down, or down-right site in one time step performing a biased

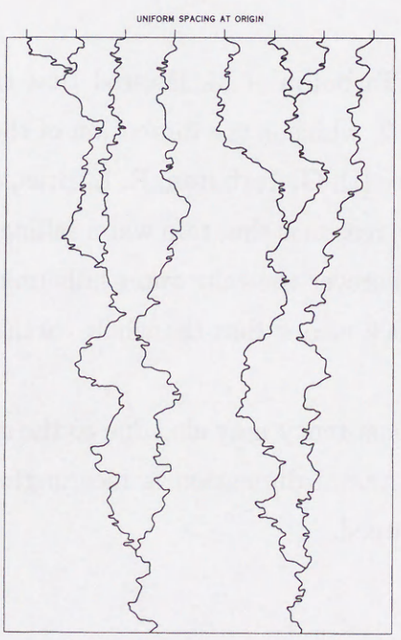

Figure 4.6: The river networks by a random walk model [L. B. Leopold and W. B. Langbein (1962), Fig.6].

random walk. When more than one random walkers come into the same site, the random walkers stick to each other and act as one random walker from there. By these procedures, the pattern similar to river network branches is obtained. An example of the river networks generated by the model is shown in Fig.4.6.

Leopold and Langbein also proposed another type of river network model shown in Fig.4.7. The model is again defined on a square lattice. A random walker is put on an arbitrary site and from there it performs a self-avoiding random walk until it reaches the system edge. During the random walk, the trajectory is recorded and the sites visited by the random walker are regarded as occupied sites. Then the second random walker is put on an unoccupied site and performs a self-avoiding random walk until it reaches the system edge or the occupied sites. The procedure is repeated till the whole system is covered by the occupied sites. We regard the ensemble of the trajectories of the random walkers as a river network. The pattern obtained in the model well reproduce the Horton's laws and the Hack's law. Recently, Meakin et al. performed large scale simulation of the model and found that the drainage-basin area of the networks also follows a power-law distribution whose exponent is estimated as $\tau = 0.39$ [P. Meakin, J. Feder, and T. Jøssang (1991)].

4.2.2 Scheidegger's Model

Scheidegger's river model is a model for river patterns on a slope defined on a two-dimensional triangular lattice [A. E. Scheidegger (1967)]. The river patterns are obtained by assigning two kinds of flow vectors, right down and left down, randomly to each lattice site (x, y). An example of the river networks by the model is illustrated in Fig.4.8.

The Scheidegger's river model can be regarded as a model of aggregation process with injection. Let us consider one-dimensional discretized space. Initially, there is a particle having unit mass on each site x. Then the particles

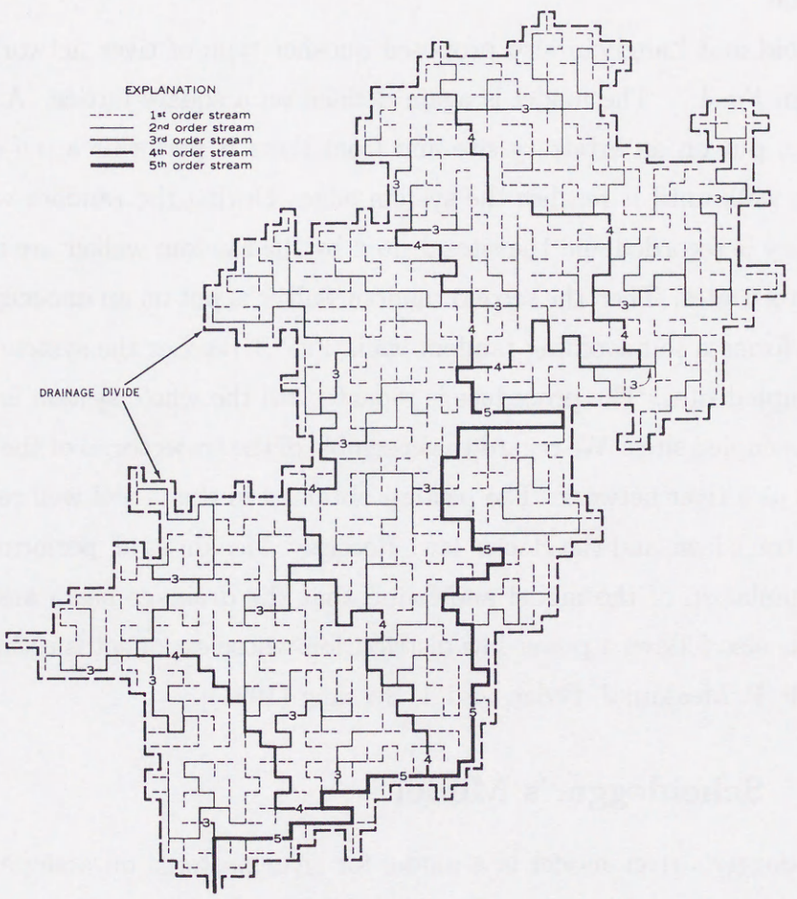

Figure 4.7: The river networks by a self-avoiding random walk model [L. B. Leopold and W. B. Langbein (1962), Fig.8].

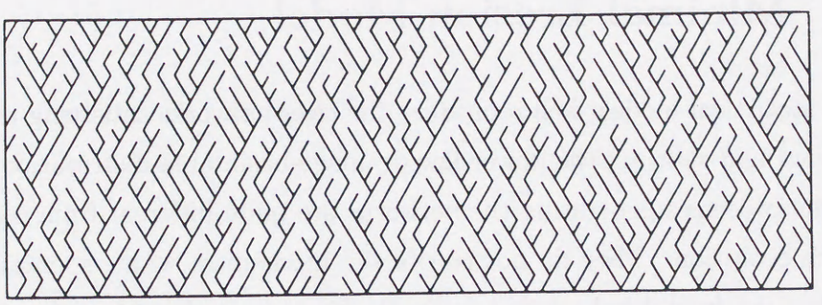

Figure 4.8: The river networks by Scheidegger's model [A. E. Scheidegger (1967), Fig.4].

move to their right neighbor site $x+1$ or stay at x with equal probability and, simultaneously, a particle having unit mass is injected on each site. When more than one particles collide at a site, they aggregate with each other forming a particle having the sum of the mass of the colliding particles. The aggregation and the injection of the particles are repeated with y increased by 1: y denotes time in this case. By observing the trajectories of the particles on x-y plane, the branching pattern identical to that by the Scheidegger's river model is obtained. The mass of the particles in the aggregation system represents the drainage-basin area in the Scheidegger's river model. Takayasu et al. studied the generalized cases of the aggregation process with injection and exactly solved the mass distribution [H. Takayasu, M. Takayasu, A. Provata, and G. Huber (1991)]. According to the result, in the case which corresponds to the Scheidegger's river model, the mass follows a power-law distribution with exponent $\tau = \frac{1}{3}$. The result means that the drainage-basin area, A, by the Scheidegger's river model follows a power-law distribution as

$$P(\geq A) \propto A^{-\frac{1}{3}} \quad . \tag{4.8}$$

4.3 Minimal Erosion Model

The statistical models well reproduce the river networks satisfying the Horton's laws and showing the power-law drainage-basin area distribution. However, the processes generating the networks are quite different from real river network evolution. They do not clarify the mechanism which spontaneously organizes the fractal behaviors seen in the river networks. Moreover, the exponents of the power-law drainage-basin area distribution by the models seem to be different from that by the field data. This fact indicates that the models belong to different universality class from that of real river networks.

Our interest is in the fractal behaviors of river networks, especially, the power-law drainage-basin area distribution. To clarify their causes, we apply the minimal model for the river network evolution as we discussed in Sec.2.4. Most of local processes which only have short range effects can be neglected when we discuss the fractal behaviors of the river networks. Therefore, we do not have to simulate all the local processes of the river network evolution. On the other hand, we should carefully introduce the processes which seem to be essential for the fractal behaviors.

As we saw in Chapter 3, one of the most important factors for the power-law branch size distribution of Laplacian fractals is the competitive growth process of clusters. The competitive cluster growth is supported by the existence of the flux density field, the gradient of the Laplace field, surrounding the clusters. The clusters in a system of the Laplacian fractals detect their relative sizes through the Laplace field and the larger clusters grow the faster. We can easily have an insight that erosion and river network evolution processes also have competitive nature similar to the Laplacian fractals.

River networks are formed to transport the water on earth's surface, and the water mainly comes from precipitation. The quantity of the precipitation may depend on seasons and spatial distribution of clouds, however, since the time

scale of landform evolution is so long, we can regard it as uniform temporally and spatially on the average. Neglecting the effects of underground water, infiltration, and evaporation, the quantity of the water is conserved during the transportation. Then the quantity of the water flowing at an arbitrary point is proportional to the area of the upper drainage basin. The transportation of the water causes the erosion of the earth's surface. The speed of the erosion depends on the intensity of the water flow, the quantity of the water flowing in the unit time period, on the surface. It is intuitively clear that the erosion speed is faster at a place where the water flow is more intensive. Since the quantity of the water flowing on a stream directly reflects the size of the stream branch, a stream which has larger drainage basin area expands its drainage basin area faster. This nature of the water erosion process must cause a competitive process among neighboring river networks very similar to that seen in the Laplacian fractals. In other words, we can regard the water erosion process as a kind of fractal growth process. We cannot observe real river network evolution because of its long time scale. However, the pictures in an experiment on the water erosion [R. Wittmann, T. Kautzky, A. Hübler, and E. Lüscher (1991)] clearly show that it looks as if the gorges by the erosion grow from the outlet upward (Fig.4.9).

As we discussed above, it seems that the essential factors for the power-law drainage-basin area distribution is the competitive growth process of river networks caused by the uniform precipitation, the conservation of the water during the flow process on the earth's surface, and the increasing erosion speed with the water-flow intensity. To confirm this insight, we introduce a minimal model of the water erosion process [H. Takayasu and H. Inaoka (1992) and H. Inaoka and H. Takayasu (1993)].

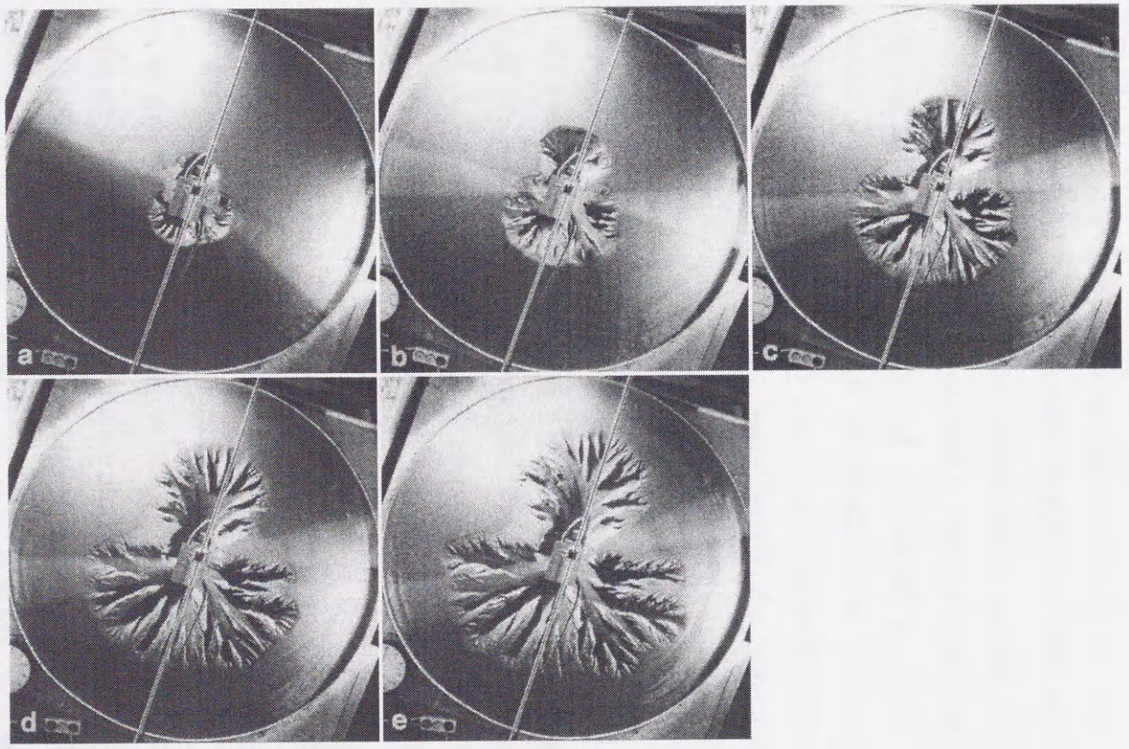

Figure 4.9: An experiment of the water erosion process. The water uniformly sprinkled on sand flows toward an outlet placed at the center of the disk. The gorges grow from the outlet to the perimeter. (a) 46s, (b) 63s, (c) 106s, (d) 213s, and (e) 360s at 3200 ml/min [R. Wittmann, T. Kautzky, A. Hübler, and E. Lüscher (1991), Fig.3].

4.3.1 Model Description

In the model, the water erosion process only by the water from rainfall is simulated, that is, the effects of underground water, infiltration, evaporation, and weathering are neglected. The rain is assumed to be falling on land uniformly and constantly. The quantity of the water on the land, which is given by the sum of the precipitation, is conserved in water-flow process. The land eroded in the model is assumed to have no geographical structure and crustal movement: it is uniform and static. Furthermore, sand produced by the erosion is assumed to be smoothly washed away by the water flow, so that the sedimentation of the sand is neglected. Because of the last assumption, the height of the land at each point decreases monotonically and never increases.

Under these conditions, the processes such as rainfall, water flow, water erosion, and formation and vanishing of lakes are simulated. The rules used in the system are local and deterministic, so randomness comes only from the initial condition of the system.

The model is defined on a two-dimensional triangular lattice. Every site (x, y) has three variables: $h(x, y)$, the height of the land; $s(x, y)$, the water-flow intensity; and $w(x, y)$, the thickness of water accumulation. The height of water surface, $h_w(x, y)$, is defined as $h_w(x, y) \equiv h(x, y) + w(x, y)$. Note that the water-flow intensity does not contribute to the height of the water surface since it is assumed to have no thickness. The thickness of the water accumulation is introduced to realize the formation and vanishing of lakes, and does not relate to the water erosion process. A site for which $w(x, y)$ is not zero is called a "lake" site.

For a given landform $h(x, y)$ and configurations of the water $s(x, y)$ and $w(x, y)$, the time evolution of the system is performed by repeating the following procedures:

1. *Determination of water-flow direction.* For every site (x, y), we find the

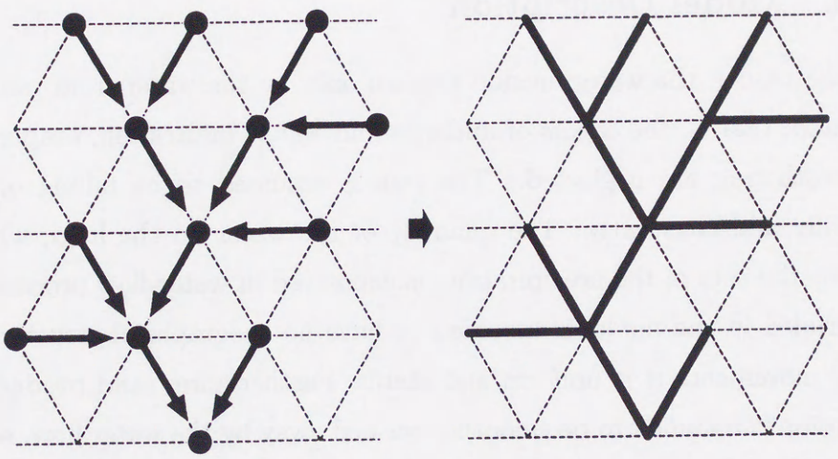

Figure 4.10: The formation of a river pattern. The arrows in the left part show the flow directions [H. Inaoka and H. Takayasu (1993), Fig.1].

site (x', y') which has the lowest height of the water surface in the six nearest neighbors. When $h_w(x, y) > h_w(x', y')$, the water-flow direction of the site (x, y) is determined as the direction to the site (x', y'). However, if $h_w(x, y) \leq h_w(x', y')$, it becomes unnatural to flow out $s(x, y)$ to the site (x', y'). In this case, $w(x, y)$ is renewed by

$$w(x, y) = h_w(x', y') - h(x, y) + \epsilon \tag{4.9}$$

to raise the water surface, where ϵ is a very small positive number. On the other hand, it is quite natural to assume that $w(x, y)$ becomes zero when $h(x, y) > h_w(x', y')$. So we make $w(x, y)$ zero at such a site. We can draw a global water-flow pattern which we call a river pattern when the water-flow directions for all sites are determined (Fig.4.10).

2. *Water erosion.* By the effect of the water erosion, $h(x, y)$ is decreased by

$$\delta h(x, y) = F(J(x, y))\{h_w(x, y) - h_w(x', y')\} \quad , \tag{4.10}$$

where $J(x, y)$ denotes water power which is defined as

$$J(x, y) \equiv s(x, y)\{h_w(x, y) - h_w(x', y')\} \quad . \tag{4.11}$$

The function F is a positive monotonically increasing function which satisfies $F(0) = 0$ and $\lim_{J\to\infty} F(J) < 1$. In the model we use $F(J) = \frac{CJ^a}{1+J^a}$, where C and a are positive constants.

3. *Water flow and rainfall.* The $s(x, y)$ is moved to the site (x', y'). The new $s(x, y)$ is determined as the sum of s from the nearest neighbors and a constant s_0. This s_0 corresponds to the water from the rainfall.

Procedures 1, 2, and 3 make one time step. These procedures are performed simultaneously on all sites.

4.3.2 Time Evolution of the System

The time evolution of the system is performed starting from an initial landform such as

$$h(x, y) = 2000.0 + r(x, y) \quad , \tag{4.12}$$

where $r(x, y)$ denotes uniform random fluctuation ranging $[0.0, 0.1)$. Namely, it has a flat surface perturbed by very slight white noise. In the initial condition, there is no water on the land, i.e., $s(x, y) = 0$ and $w(x, y) = 0$ for every site. As for the boundary condition of the system, the left- and right-side edges of the system are connected by a periodic boundary condition. A high wall is built on the top-side edge, while the height of the bottom-side edge is zero and fixed, so all of the water in the system flows out from the bottom-side edge. At first we fix the value of the parameter in the function $F(J)$ as $a = 1.0$.

Fig.4.11 shows an example of time evolution of a landform. As can be seen from the series of figures, gorges grow from the bottom-side edge to the top-side edge.

Sufficiently evolved river networks are considered to have no stagnant region of water such as lakes. In the model the lakes are made at local minimum sites, which have not undergone sufficient erosion. Therefore, the number of the lake sites indicates the maturity of the landform in the system. We plot the number

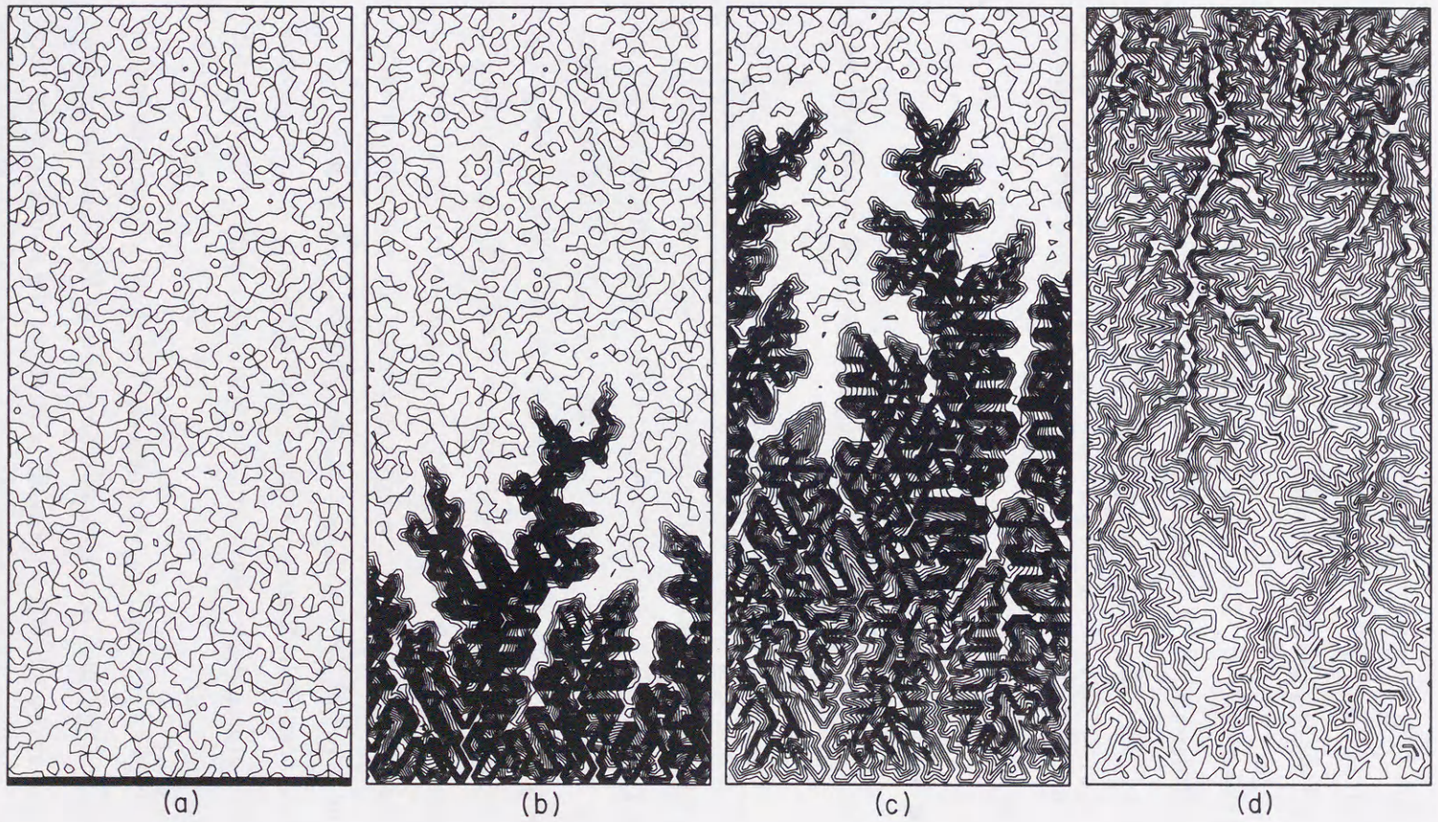

Figure 4.11: A series of contour maps of the landform evolution for $a = 1.0$. A part (40×100) of the system of size 100×100 is illustrated. (a) Initial condition. (b) At 300 time steps. (c) At 600 time steps. (d) At 1500 time steps [H. Inaoka and H. Takayasu (1993), Fig.2].

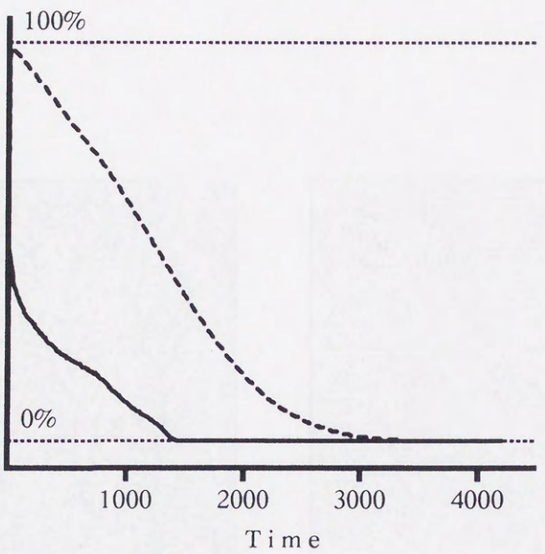

Figure 4.12: The number density of the lake sites (dashed line) and the unstable sites (bold line). The number is shown as a percentage [H. Inaoka and H. Takayasu (1993), Fig.4].

densities of the lake sites and unstable sites which change the flow direction in one time step in Fig.4.12. Initially, almost all sites are covered by lakes, and the number of the lake sites decreases monotonically with the evolution of the gorges. About the time that the gorges spread over the whole surface in the system, the number of the lake sites becomes zero. In this stage, the number of the unstable flows also becomes zero, namely, the system reaches a kind of steady state where all sites in the system do not change their flow directions. This steady state is very stable, so once the system reaches this steady state, the river pattern on the surface never changes while the erosion process of the land progresses. An example of a steady-state river pattern is displayed in Fig.4.13.

In the model, the randomness of the resulting landform comes only from the initial condition, so the sensitivity to perturbation in the initial landform of the model is an important problem. To check the sensitivity, two identical

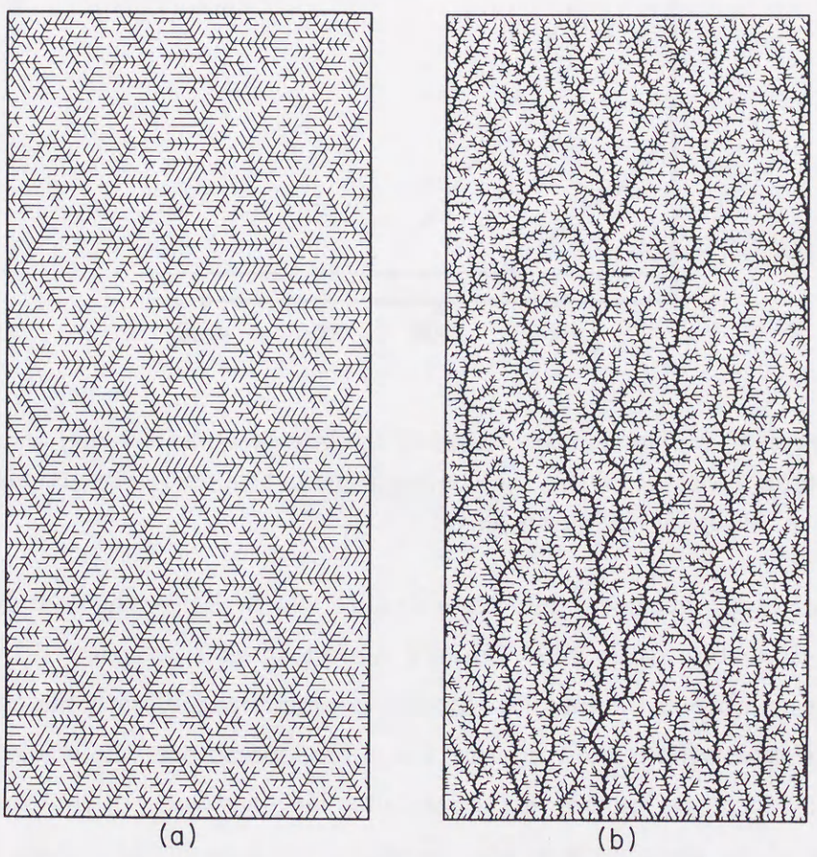

Figure 4.13: An example of a steady-state river pattern from the system of size 512×512. (a) An enlargement of the system. A part of size 50×128 is illustrated. (b) A part of size 200×512. The thickness of the pattern is proportional to the logarithm of the water-flow intensity [H. Inaoka and H. Takayasu (1993), Fig.5].

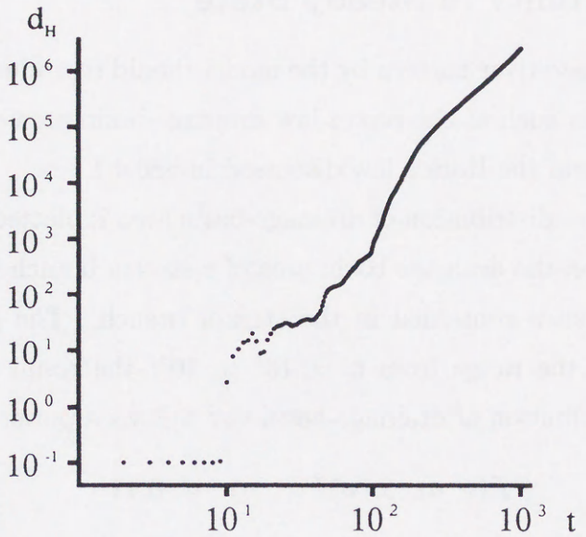

Figure 4.14: The time evolution of the Humming distance d_H of the case $a = 1.0$ in log-log scale. The straight part of the line ranging from 200 to 1000 time steps shows that the errors grow as $d_H \propto t^{2.6}$ [H. Inaoka and H. Takayasu (1993), Fig.6].

initial landforms, $h_1(x, y)$ and $h_2(x, y)$, are prepared and a noise (=0.1) is put on a randomly chosen site of $h_2(x, y)$. These two landforms are evolved and Humming distance defined as

$$d_H \equiv \sum_{x,y} |h_2(x, y) - h_1(x, y)| \tag{4.13}$$

is calculated for every time step. Fig.4.14 shows a result of the case $a = 1.0$ in log-log scale. The points are on a straight line ranging from 200 to 1000 time steps, while they look irregular at the beginning. This result shows that the Humming distance d_H expands as

$$d_H \propto t^{2.6} \quad , \tag{4.14}$$

namely, errors grow following a power law indicating that the system is at the edge of chaos.

4.3.3 Fractality in Steady State

The steady-state river pattern by the model should reproduce the statistical fractal properties such as the power-law drainage-basin area distribution, the Horton's laws, and the Hack's law discussed in Sec.4.1.

The cumulative distribution of drainage-basin area is plotted in log-log scale in Fig.4.15. Here, the drainage basin area of a stream branch is defined as the number of the sites contained in the stream branch. The points are on a straight line in the range from $n = 10^1$ to 10^3; the result shows that the cumulative distribution of drainage-basin size follows a power law

$$P(\geq n) \propto n^{-\tau} \quad , \quad \tau = 0.42 \quad . \tag{4.15}$$

Ordering the streams in the river networks by the Horton's stream order, we estimate the number of the streams, N_ω, and the average stream length, L_ω, for each stream order, ω, and plot them in semilog scale in Fig.4.16. The

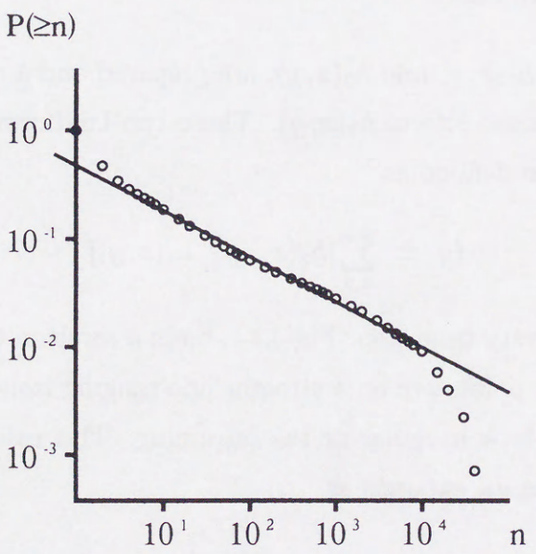

Figure 4.15: The cumulative distribution of drainage-basin area $P(\geq n)$ of the case $a = 1.0$ in log-log scale. The line shows a power law as $P(\geq n) \propto n^{-0.42}$ [H. Inaoka and H. Takayasu (1993), Fig.7].

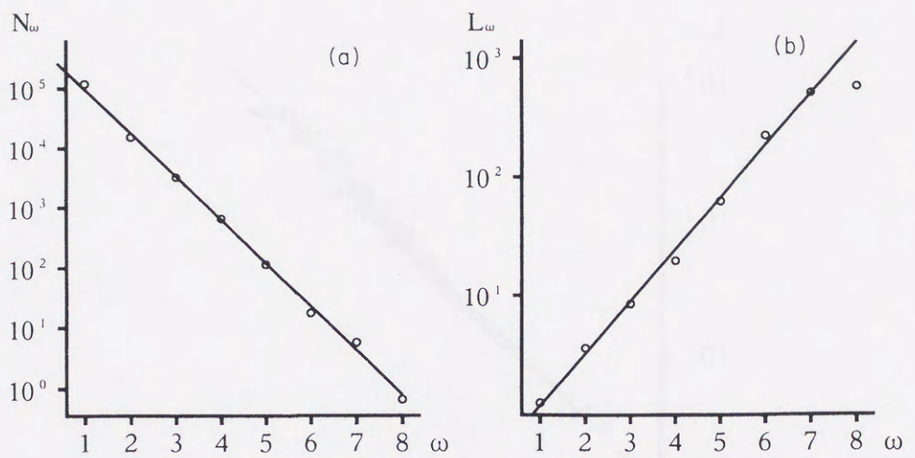

Figure 4.16: The relations of the stream order ω and (a) the number of streams N_ω and (b) the average stream length L_ω in semilog scale for $a = 1.0$ [H. Inaoka and H. Takayasu (1993), Fig.10].

points are clearly on straight lines except for the points of the highest order. The values of the bifurcation and the stream-length ratios are estimated as $R_B = 5.3$ and $R_L = 2.7$ in the case $a = 1.0$, respectively. The results are in the range of the field data. However, we should note that these results may have comparatively large errors because only seven or eight points are used to estimate these ratios.

The Hack's law is also confirmed by plotting the relation between drainage-basin area of stream branches and their main stream length. Fig.4.17 is the result and the value of the Hack's exponent α is found in the range as $\alpha = 0.60 - 0.64$. Since the fractal dimension of the main stream by the model is confirmed to be very close to 1.0, it is clarified that the Hack's law is reproduced purely by the self-affine property of the drainage basins in the case of the model. The self-affine property of the river networks is seen clearly in the shapes of the drainage basins in the model. In Fig.4.18 the branches of the steady-state river pattern having different drainage-basin area by the model are illustrated. By the figure, it is noticed that the river basins have more

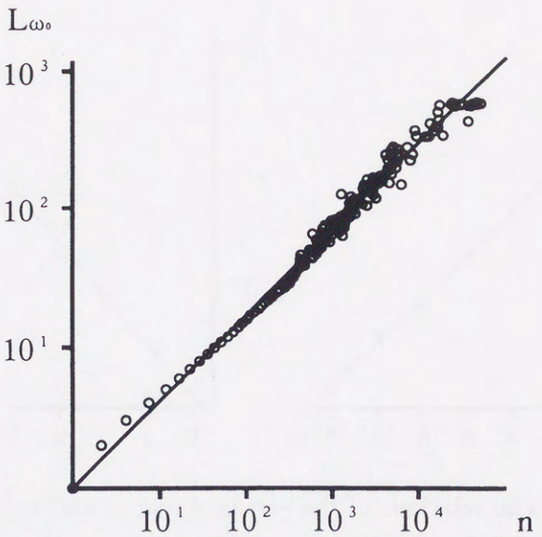

Figure 4.17: The relation between the drainage basin area and the main stream length in log-log scale for the case $a = 1.0$. The line shows a relation as $L \propto n^{0.62}$ [H. Inaoka and H. Takayasu (1993), Fig.12].

elongated shape as they have larger drainage-basin area as mentioned by Hack indicating that the self-similarity of the drainage basins is broken.

As shown above, the steady state river networks by the model well reproduce the fractal properties of the real river networks such as the drainage-basin area distribution, the Horton's laws, and the Hack's law. The numerical results such as the exponent of the power-law drainage-basin area distribution and the Hack's ratios are also in good agreement with the field data. This fact indicates that the factor introduced in the model, the competitive growth of the river networks by the erosion process, is essential for the fractal behaviors.

4.3.4 Universality in Erosion Process

The statistical fractal behaviors by the model show robust universality to the function form of the water power $F(J)$, the initial condition, and the geological feature of the eroded land.

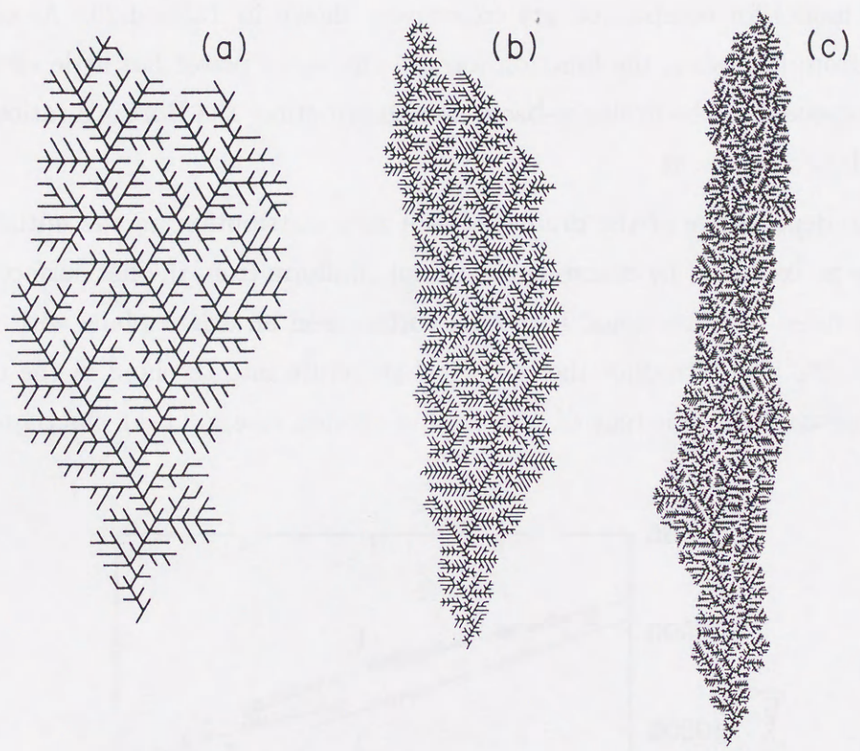

Figure 4.18: The river network branches having different branch size from the steady-state river pattern. The shape of a drainage basin is more elongated as it has larger basin area. (a) $n = 748$, (b) $n = 3257$, and (c) $n = 11020$ [H. Inaoka and H. Takayasu (1993), Fig.11].

The form of the water-power function $F(J)$ for $J \ll 1$ is ruled by the parameter a. So the dependence in the behavior of the model on the function form can be examined by changing the value of the parameter a. In the cases of $a \neq 1.0$, the model also reaches the steady state where the river patterns are frozen. The numerical results of the cases of various a and the Scheidegger's river model for comparison are collectively shown in Table 4.20. As can be seen from the table, the function form of the water power has little effect on the exponent of the drainage-basin area distribution, the Horton's ratios, and the Hack's exponent.

The dependence of the drainage-basin area distribution on the initial condition is examined by changing the initial landform from the flat surface with white noise to a fractional Brownian surface and an aslant plane with white noise. We also introduce the geological structure into the land in the model by replacing the constant C to a field of erosion rate, $C(x, y)$, fluctuated by

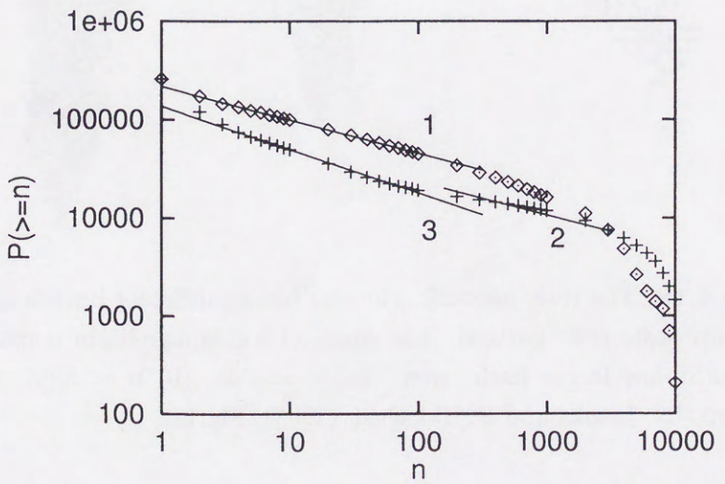

Figure 4.19: The cumulative distribution of drainage-basin area stating from a slope. The lines (1) and (2) show a theoretical slope of the Scheidegger's river model, $-\frac{1}{3}$, and line (3) shows a slope of -0.44 [R. Li, H. Takayasu, and H. Inaoka (1996), Fig.3].

a fractional Brownian surface function. All these cases lead to the identical power-law distribution to that of the original model within error range [R. Li, H. Takayasu, and H. Inaoka (1996)].

For example, in the case of the aslant plane initial condition, the appearance of the initial river network is very similar to that of the river networks by the Scheidegger's river model. In fact, the drainage-basin area distribution follows a power-law distribution with an exponent very close to $\frac{1}{3}$, the theoretical result of the Scheidegger's river model. Even in this case, as the erosion process proceeds, the river network is re-organized to have the exponent $\tau = 0.44$, which is the universal value of the minimal erosion model (Fig.4.19).

Thus the exponent $\tau \simeq 0.42$ is universal.

Parameter a	0.5	0.8	1.0	1.2	1.5	Scheidegger's model	Error range
Power-law exponent of drainage-basin area distribution, β	0.43	0.42	0.42	0.41	0.40	0.36 ($\frac{1}{3}$)	0.01
Bifurcation ratio R_B	5.4	5.3	5.3	5.2	5.1	4.7	0.4
Stream-length ratio R_L	2.7	2.7	2.7	2.7	2.7	3.0	0.1
Fractal dimension of the river patterns from Horton's ratios D_s	1.69	1.67	1.66	1.66	1.65	1.40	
Fractal dimension of the river patterns from β, D_β	1.75	1.72	1.72	1.70	1.69	1.58 ($\frac{3}{2}$)	
Hack's exponent α	0.60	0.62	0.62	0.63	0.64	0.68 ($\frac{2}{3}$)	0.02

Table 4.20: The numerical results by simulations of size 512×512 for various values of parameter a [H. Inaoka and H. Takayasu (1993), Table I]. The results for the Scheidegger's river model are also shown for comparison. The values in the parentheses are the theoretical results [H. Takayasu, M. Takayasu, A. Provata, and G. Huber (1991)].

4.4 Mean Field Approach

In this section we introduce a mean field approach for the statistical fractal properties in the river networks by the lattice models discussed in the previous sections.

4.4.1 Drainage-basin Area Distribution

Let p_k be the probability that the number of streams which flow into an arbitrary chosen site is k, and n_i $(i = 1, 2, \ldots, k)$ be the drainage-basin area of the site which has an inflowing stream to the chosen site. In the numerical models such as the minimal erosion model, whole sites in the system belong to river networks forming a part of a stream branch. Since each site has one outflowing link, the number of the flow links is equal to the total number of the sites in the system. It means that the expectation of the number of the streams which flow into the chosen site must be 1, so p_k satisfies the following two relations:

$$\sum_k p_k = 1 \quad , \tag{4.16}$$

$$\sum_k k p_k = 1 \quad . \tag{4.17}$$

Note that k takes 0, 1, and 2 in the case of the Scheidegger's river model or 0, 1, 2, and 3 in the case of the minimal erosion model. The drainage-basin area for the chosen site, n, is the sum of n_i and the number of the site itself = 1, that is,

$$n = n_1 + n_2 + \cdots + n_k + 1 \quad . \tag{4.18}$$

By treating the nearest neighbor sites as mean-field sites, the distribution of n, $P(n)$, follows an equation

$$P(n) = \sum_k p_k \sum_{n_1+n_2+\cdots+n_k=n-1} P(n_1)P(n_2)\cdots P(n_k) \quad . \tag{4.19}$$

Instead of treating the distribution itself, we introduce a characteristic function $Z(\rho)$, the Laplace transform of $P(n)$, which is defined as

$$Z(\rho) \equiv \sum_{n=1}^{\infty} e^{-\rho n} P(n) \quad . \tag{4.20}$$

We obtain the equation for $Z(\rho)$ by transforming both sides of Eq.(4.19):

$$Z(\rho) = e^{-\rho} \sum_{k} p_k Z(\rho)^k \quad . \tag{4.21}$$

The asymptotic behavior of $P(n)$ for $n \to \infty$ corresponds to that of $Z(\rho)$ for $\rho \to 0$. To explore this behavior, we expand $Z(\rho)$ around $\rho = 0$. By definition $Z(0) = 1$; we put $Z(\rho)$ as

$$Z(\rho) = 1 + \tilde{Z}(\rho) \quad , \quad |\tilde{Z}(\rho)| \ll 1 \tag{4.22}$$

around $\rho = 0$. Substituting Eq.(4.22) into Eq.(4.21) and using Eqs.(4.16) and (4.17), we find

$$\tilde{Z}(\rho) \propto \rho^{\frac{1}{2}} \quad , \tag{4.23}$$

so $Z(\rho)$ is obtained as

$$Z(\rho) = 1 + c\rho^{\frac{1}{2}} + \cdots \quad , \tag{4.24}$$

where c denotes a constant. Eq.(4.24) indicates that the distribution $P(n)$ is proportional to $n^{-\frac{3}{2}}$ for large n. The cumulative distribution of n becomes

$$P(\geq n) \propto n^{-\frac{1}{2}} \quad , \tag{4.25}$$

which shows that the mean-field exponent τ is $\frac{1}{2}$. It is easy to show that if we omit the space-filling condition Eq.(4.17), then the distribution of n always has an exponential decay. That is, the space-filling condition that every site has one outflowing stream leads to the fractal behaviors of river networks.

4.4.2 Horton's Laws

We use the Strahler's stream order in this discussion. Let S_ω be the number of sites which belong to ω-order streams. We define site-number ratio, R_S, as

$$R_S \equiv \frac{S_\omega}{S_{\omega+1}} \quad . \tag{4.26}$$

Using the total site number of the system, $S = \sum_\omega S_\omega$, and S_ω, the probability W_ω that an arbitrary chosen site in the system belongs to an ω-order stream is given by

$$W_\omega = \frac{S_\omega}{S} \quad . \tag{4.27}$$

In this discussion the limited situation that the maximum number of inflowing streams at a confluence is 2 is examined, while it is three in the steady-state river networks by the minimal erosion model. In the case that the number of the inflowing streams is 2, the stream order of the outflowing stream ω is determined as follows in terms of the stream orders of the inflowing streams, ω_1 and ω_2:

$$\omega = \begin{cases} \max\{\omega_1, \omega_2\} & \text{for} \omega_1 \neq \omega_2 \\ \omega_1 + 1 & \text{for} \omega_1 = \omega_2 \end{cases} \quad . \tag{4.28}$$

Also taking into account the cases of $k = 0$ and 1, we have five cases of ω, the order of the outflowing stream of the chosen site, with probabilities given as follows:

$$\begin{array}{lll} k = 0, & \omega = 1 & \text{with probability} \quad p_0 \\ k = 1, & \omega = \omega_1 & \text{with probability} \quad p_1 W_{\omega_1} \\ k = 2, & \left\{ \begin{array}{ll} \omega = \omega_1 & \text{with probability} \quad p_2 W_{\omega_1} \sum_{j=1}^{\omega_1 - 1} W_j \\ \omega = \omega_2 & \text{with probability} \quad p_2 W_{\omega_2} \sum_{j=1}^{\omega_2 - 1} W_j \\ \omega = \omega_1 + 1 & \text{with probability} \quad p_2 {W_{\omega_1}}^2 \end{array} \right. \end{array} \quad .$$

Thus we obtain the equations for W_ω as

$$W_1 = p_0 + p_1 W_1 \quad , \tag{4.29}$$

$$W_\omega = p_1 W_\omega + 2p_2 W_\omega \sum_{j=1}^{\omega-1} W_j + p_2 W_{\omega-1}^2 \quad . \tag{4.30}$$

Using Eqs.(4.16) and (4.17) of the case $k = 0$, 1, and 2, we find $W_1 = \frac{1}{2}$ and $W_\omega = 2^{-\omega}$. So the site-number ratio R_S is independent of ω and is estimated as

$$R_S = \frac{S_\omega}{S_{\omega+1}} = \frac{W_\omega}{W_{\omega+1}} = 2 \quad . \tag{4.31}$$

Next we consider the average stream length of ω-order streams. The probability that a stream starting with order ω remains to be of the same order in l sites is given as

$$\left[p_1 + p_2 \sum_{j=1}^{\omega-1} W_j\right]^{l-1} p_2 \left[1 - \sum_{j=1}^{\omega-1} W_j\right] (p_2 W_{\omega-1}^2)^{-1} \quad . \tag{4.32}$$

The expectation of l, L_ω, is then calculated as

$$\begin{aligned} L_\omega &= \sum_{l=1}^{\infty} l \left[p_1 + p_2 \sum_{j=1}^{\omega-1} W_j\right]^{l-1} p_2 \left[1 - \sum_{j=1}^{\omega-1} W_j\right] (p_2 W_{\omega-1}^2)^{-1} \\ &= \sum_{l=1}^{\infty} l \{p_1 + p_2(1 - 2^{1-\omega})\}^{l-1} \{1 - (1 - 2^{1-\omega})\} 2^{2(\omega-1)} \\ &= \{p_2(1 + 2^{1-\omega})\}^{-2} 2^{\omega-1} \quad . \end{aligned} \tag{4.33}$$

Therefore, the stream-length ratio R_L for large ω is obtained as

$$R_L = \lim_{\omega \to \infty} \frac{L_{\omega+1}}{L_\omega} = 2 \quad . \tag{4.34}$$

The number of ω-order streams in the system is given by $N_\omega = \frac{S_\omega}{L_\omega}$, so the bifurcation ratio $R_B = \frac{N_\omega}{N_{\omega+1}}$ is calculated from R_S and R_L as

$$\frac{N_\omega}{N_{\omega+1}} = \frac{S_\omega}{S_{\omega+1}} \frac{L_{\omega+1}}{L_\omega} = R_S R_L = 4 \quad . \tag{4.35}$$

Summarizing these results, the mean-field Horton's ratios are $R_B = 4$ and $R_L = 2$.

4.5 Scaling Relation

A simple scaling relation between the exponent of the drainage-basin area distribution and the Hack's exponent is derived by dimension analysis. We also show the effectiveness of the stable distribution theorem to the scaling relation.

4.5.1 Scaling Relation in River Network Models

Let us consider a square system whose linear dimension is L. The drainage-basin area distribution by field data and numerical models inevitably has a cutoff because of the finiteness of the system size. Considering the self-affine nature of drainage basins, the cutoff drainage-basin area is assumed to be written using an exponent z as L^z. We describe the drainage-basin area distribution with the cutoff, $P_L(\geq A)$, as

$$P_L(\geq A) \propto A^{-\tau} f(A/L^z) \quad , \tag{4.36}$$

where A and $f(x)$ denote drainage-basin area and a cutoff function defined as

$$f(x) \simeq \begin{cases} 1 & \text{for } x \ll 1 \\ 0 & \text{for } x \gg 1 \end{cases} \quad . \tag{4.37}$$

The number of the stream branches in the system should be proportional to the perimeter length of the system because each branch must occupy a perimeter site as a mouth of the river. Since the river network fills the whole surface in the system, the following relation holds:

$$L^2 \propto L \int_0^\infty A^{1-(\tau+1)} f(A/L^z)\, dA \propto L^{1+(1-\tau)z} \quad . \tag{4.38}$$

The relation suggests a scaling relation as

$$(1-\tau)z = 1 \tag{4.39}$$

[P. Meakin, J. Feder, and T. Jøssang (1991)]. Since the exponent z describes the self-affine nature of river basins, it is related to the Hack's exponent α.

The diameter of the largest river basin in the system along the main stream must be proportional to the system size. In the case that the fractal dimension of the main stream is 1, the diameter is regarded to be nearly equal to the main stream length. Therefore, we can interpret that the system size L is proportional to the main stream length of the largest basin, and it means that the exponent z is the inverse of the Hack's exponent α by the Hack's law Eq.(4.4). The relation Eq.(4.39) is written using the Hack's exponent α as

$$\tau = 1 - \alpha \quad . \tag{4.40}$$

4.5.2 Application of Stable Distribution Theorem

The identical scaling relation to Eq.(4.40) also derived by using the theorem of stable distribution introduced in Sec.2.3 [H. Takayasu (1993)].

We consider a situation that all the water in the system is drained to one side of the system such as illustrated in Fig.4.13. In such situation, all stream branches in the system have their outlet on the draining side. Considering a part of the draining side, S, whose length is λ, we extract a set of the drainage basins whose outlet is located in S. We define generalized drainage-basin area, $A(\lambda)$, for the extracted set of drainage basins as

$$A(\lambda) \equiv \sum_{i \in S} A_i \quad , \tag{4.41}$$

where A_i denotes the drainage-basin area of the individual river networks and sum runs over the drainage basins whose outlets are located in S. Note that $A(1)$ denotes the area of the individual drainage basins in lattice models since a drainage basin occupies one site on the outlet side.

We describe the relation between the width, w, and the height, h, of a drainage basin using an exponent for the self-affine nature, ν, as

$$h \propto w^{\nu} \quad . \tag{4.42}$$

We regard that the Hack's relation Eq.(4.4) purely comes from the self-affine nature of the river basins and that the fractal dimension of the main stream is 1. Then the basin height is regarded to be proportional to the main stream length and the exponent ν is written by the Hack's exponent α as $\nu = \frac{1}{1-\alpha}$. By assuming a kind of self-similarity of drainage basin configurations, we expect a relation

$$A(\lambda) \stackrel{d}{=} \lambda^{1+\nu} A(1) \quad , \tag{4.43}$$

where $\stackrel{d}{=}$ denotes that the stochastic variables on both sides follow the identical distribution.

By combining two adjacent generalized drainage basins whose outlet side lengths are λ_1 and λ_2, respectively, we form a generalized drainage basin whose outlet side length is $\lambda_1 + \lambda_2$. In such situation, a relation, $A(\lambda_1 + \lambda_2) = A(\lambda_1) + A(\lambda_2)$, holds since there is no aperture between two adjacent generalized drainage basins. Generalizing the relation, we assume

$$A(\lambda_1 + \lambda_2) \stackrel{d}{=} A(\lambda_1) + A(\lambda_2) \tag{4.44}$$

even in the case that two generalized drainage basins are not located adjacently.

According to the theorem of stable distribution discussed in Sec.2.3, an independent stochastic variable following the relations Eqs.(4.43) and (4.44) follows a stable distribution that has a power-law tail as

$$P(\geq A) \propto A^{-\tau} \quad , \quad \tau = \frac{1}{1+\nu} \quad . \tag{4.45}$$

Using the Hack's exponent α, we finally obtain the relation between τ and α as

$$\tau = 1 - \alpha \quad . \tag{4.46}$$

It is clear that the stochastic variable $A(\lambda)$ is not independent. However, the result Eq.(4.46) is well confirmed by the data in Table 4.20 and field data.

Chapter 5

Impact Fracture

5.1 Experiments of Impact Fracture

Because of its importance in various fields of science, there are numerous studies of fracture process. Here, we treat the fracture process of brittle materials caused by impact. We focus only on fractal behaviors of the impact fracture process, especially, power-law fragment mass distribution. In this section, we survey several experimental results showing the power-law fragment mass distribution and the existence of "failure wave" which seems to be a clue to the study of the cause of the fractal behaviors.

5.1.1 Fractal Fragment Mass Distribution

Concerning the size distribution of the fragments by an impact fracture process, there is a well known experimental work by Gilvarry and Bergstrom [J. J. Gilvarry and B. H. Bergstrom (1961)]. They performed a series of experiments under carefully controlled conditions. They used glass spheres as specimens and filled around the specimens with congealed gelatin to avoid the fragments to scatter and cause secondary fragmenting. The load to the specimens were also controlled to form single impacts to the specimens. By these conditions, we can regard that the results by the experiments describe the pure behaviors of the impact fracture process caused by single impact. According to the results, the cumulative fragment size distribution is well described as $P(\geq v) \propto v^{-\frac{2}{3}}$ as shown in Fig.5.1, where v denotes the volume of the fragments. Assuming that the mass of a fragment, m, is proportional to the volume of the fragment, the distribution describes cumulative power-law fragment mass distribution as $P(\geq m) \propto m^{-\frac{2}{3}}$.

Recently, Oddershede et al. performed a set of experiments of the impact fragmentation using specimens of various materials such as gypsum, soap, stearic paraffin, and frozen potato and various shapes as balls, cubes, half cubes, plates, and bars [L. Oddershede, P. Dimon, and J. Bohr (1993)]. Their

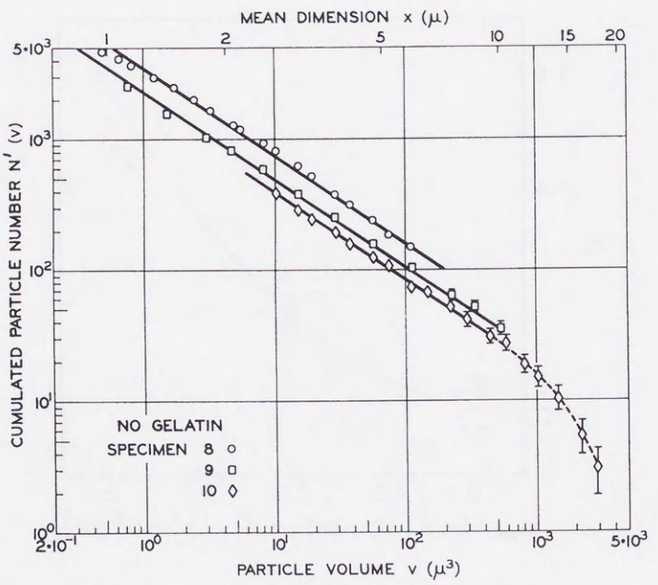

Figure 5.1: The cumulative fragment size distribution by impact fragmentation. The fragment size is measured by volume [J. J. Gilvarry and B. H. Bergstrom (1961), Fig.14].

experiments were performed by throwing the specimens onto a hard floor or by striking them with a hammer. They confirmed the power-law fragment size distribution. Moreover, they found that the exponent of the distribution does not depend on the material of the specimens but depends on the shape or the dimensionalities of the specimens. They introduced a shape parameter, d_m, by the dimensions of a fractured object, a, b, and c, as

$$d_m \equiv 1 + \frac{2(ab + bc + ca)}{a^2 + b^2 + c^2} \tag{5.1}$$

and plotted the exponent of the fragment mass distribution versus the shape parameter as shown in Fig.5.2. According to their results, the values for the exponent of the cumulative fragment size distribution are 0.05, 0.08, and 0.63 for a bar, a disk, and a ball made of gypsum, respectively. These results are regarded as the results by the fragmentation of one-, two-, and three-dimensional objects and the exponent by the three-dimensional case shows

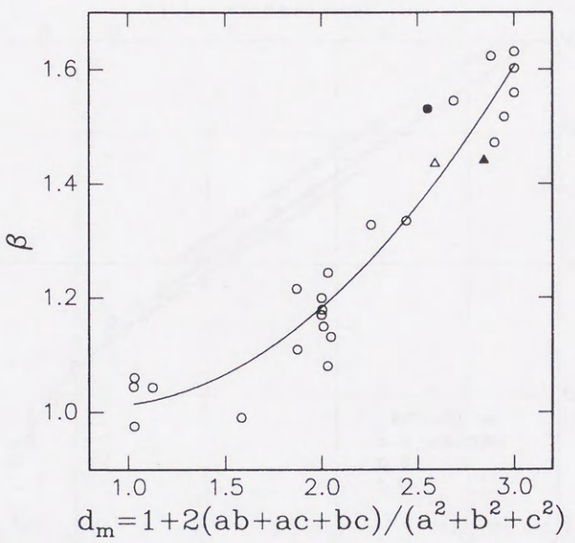

Figure 5.2: The exponent of the power-law fragment size distribution density as a function of a shape parameter. Data points for gypsum, soap, stearic paraffin, and frozen potato are given as open circles, a filled circle, a triangle, and a filled triangle, respectively [L. Oddershede, P. Dimon, and J. Bohr (1993), Fig.4].

good agreement within the error range with the Gilvarry's result, $\frac{2}{3}$.

On the other hand, Ishii and Matsushita performed experiments of the fragmentation of glass rods and found that the function form of the fragment size distribution depends on the experimental condition [T. Ishii and M. Matsushita (1992)]. The glass rods were put into steel pipes with sealed ends, and the experiments were performed by dropping the pipes onto a concrete floor from various heights. The experiments correspond to the case of the one-dimensional fragmentation. In the cases that the falling height is low, the fragment size distribution shows log-normal distribution as indicated in Fig.5.3. The distribution is given versus normalized fragment length by the length of the specimen. Since the fragment length is proportional to the fragment mass in the case of the one-dimensional fragmentation, the distribution is identical

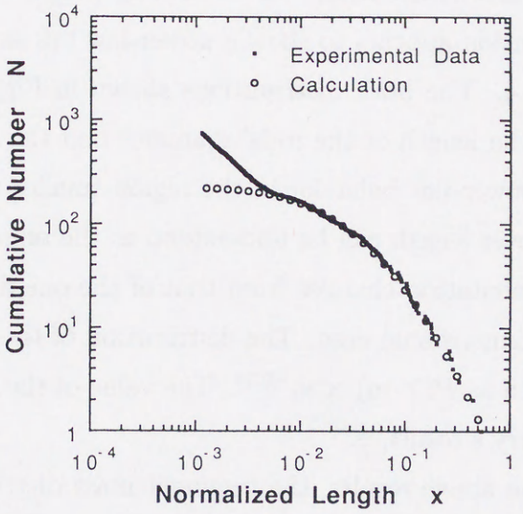

Figure 5.3: The cumulative number of fragments for the falling height at 1.2m. The open circles represent cumulative log-normal distribution [T. Ishii and M. Matsushita (1992), Fig.3].

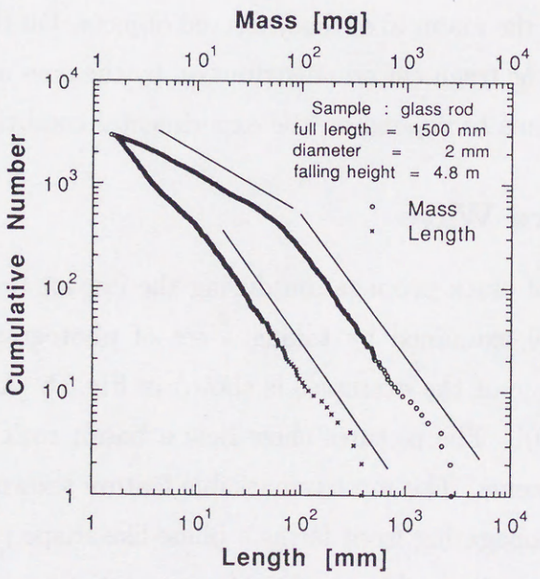

Figure 5.4: The cumulative number of fragments for the falling height at 4.8m [T. Ishii and M. Matsushita (1992), Fig.4].

to the fragment mass distribution. As the falling height increases, the fragment mass distribution appears to show a power-law tail as $P(\geq m) \propto m^{-1.40}$ as shown in Fig.5.4. The both distributions shown in Figs.5.3 and 5.4 have crossover around the length of the rods' diameter and the distributions seem to show another power-law behavior in the region smaller than the crossover length. The crossover length can be understood as the point where the mechanism of the fragmentation changes from that of the one-dimensional case to that of the three-dimensional case. The distribution of the smaller fragments in Fig.5.4 is written as $P(\geq m) \propto m^{-0.59}$. The value of the exponent is rather close to the Gilvarry's result, $\frac{2}{3}$.

Summarizing the above results, the fragment mass distribution in the case where the mechanism of the three-dimensional fragmentation is dominant follows a universal power law,

$$P(\geq m) \propto m^{-\tau} \quad , \quad \tau = \frac{2}{3} \quad , \tag{5.2}$$

not depending on the material of the fractured objects. On the other hand, the function form of the fragment size distribution by the one- or two-dimensional fragmentation seems to depend on the experimental conditions.

5.1.2 Failure Wave

The behavior of crack propagation during the impact fracture process can be experimentally examined by taking a set of photographs using a high-speed camera. One of the examples is shown in Fig.5.5 [A. Fujiwara and A. Tsukamoto (1980)]. The pictures show how a basalt rock hit by a bullet is broken into fragments. The most remarkable feature shown in the pictures is that the crack propagating front forms a plane-like shape propagating with a nearly constant velocity and most of the fragmentation looks occurring on the front. That is, there are no cracks at all in front of the crack propagating front while many fragments are left behind at the back of the front without obvious

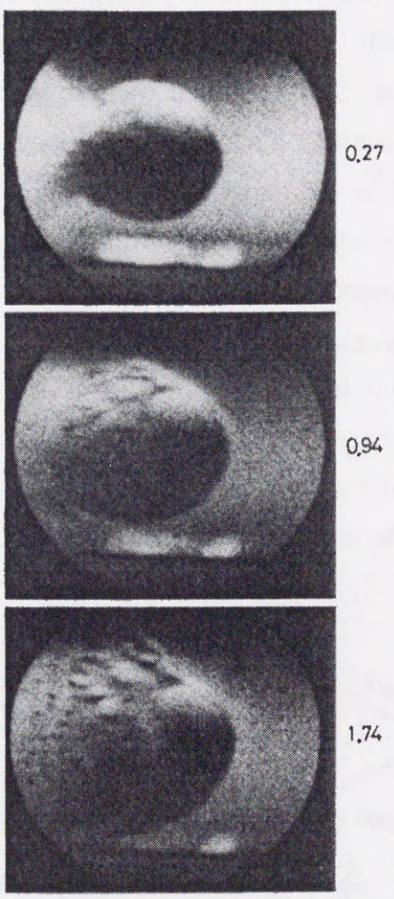

Figure 5.5: Pictures during a fragmenting process of a rock caused by collision of a bullet. The numerics at just right of the pictures indicate the time after the collision in msec [A. Fujiwara and A. Tsukamoto (1980), Fig.1(e)].

secondary fragmentation. The phenomenon of the crack front propagation is called a "failure wave".

The nature of the failure wave was experimentally studied in detail [N. S. Brar, S. J. Bless, and Z. Rosenberg (1991) and S. J. Bless, N. S. Brar, G. Kanel, and Z. Rosenberg (1992)]. The experiments were performed using glass bars and plates as specimens. The specimen was impacted by a projectile under the condition to induce a plane shock wave propagating into the specimen. The situation observed in the experiments is summarized in Fig.5.6. It was observed that the failure wave propagates from the impact side of the specimen with slower speed compared to the speed of the plane shock wave. The speed of the failure wave propagation is not a constant. The speed increases as the speed of the projectile hitting the specimen increases, and it slightly decreases as the failure wave propagate through the specimen. These behavior implies the nonlinear nature of the failure wave. The glass just behind the failure wave is observed to undergo violent expansion. We can imagine that the crack

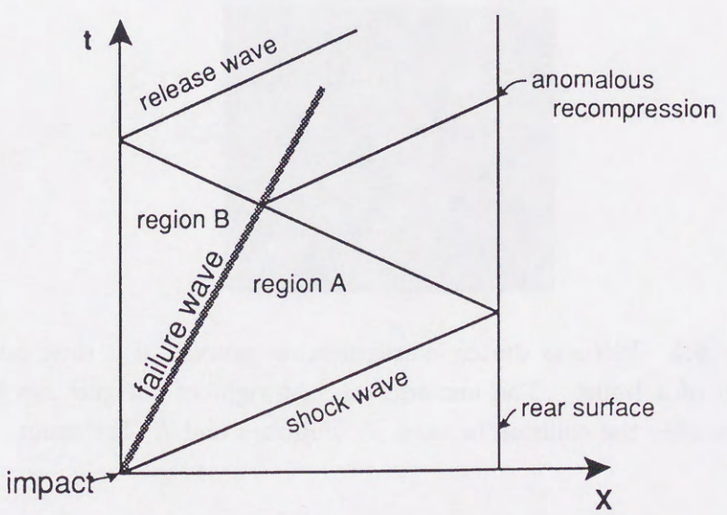

Figure 5.6: A schematic picture of the situation observed in the impact fracture process of a glass plate [S. J. Bless, N. S. Brar, G. Kanel, and Z. Rosenberg (1992), Fig.2].

propagation is caused by the dilatant behavior of the glass.

5.2 Numerical Model of Impact Fracture

The behavior of the impact fragmentation is quite complex. In the fragmenting process of real material, nonlinear, plastic, and dissipative effects of the material cannot be neglected. On the other hand, the fractal behaviors of a quasi-static fracture process is often studied by a numerical model which only treats the deformation of the material by linear elasticity and breaking of the material at threshold deformation. Recently, a simple numerical model for the impact fracture process was proposed [Y. Hayakawa (1995)]. The model treats the deformation of material only by the linear elasticity, and the breaking of the material is assumed to occur at threshold deformation.

In the model, the objects undergoing the fragmentation is represented by a cubic lattice. A mass point called an atom is put at each lattice site and pairs of the nearest neighbor and the next nearest neighbor atoms are connected

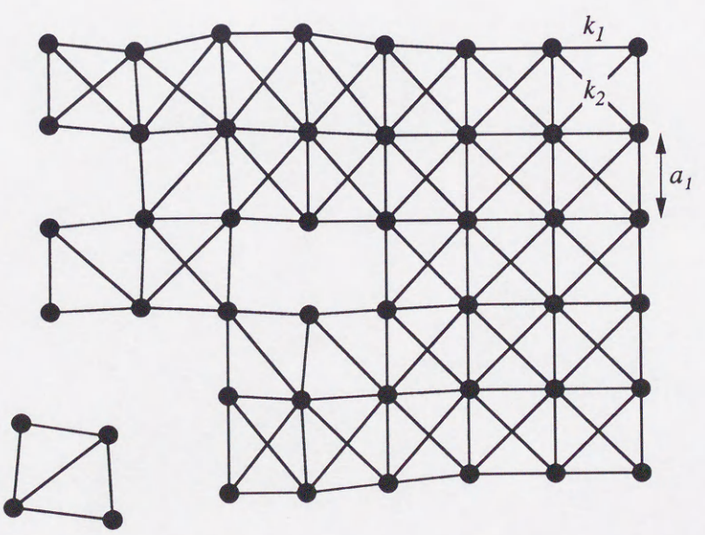

Figure 5.7: A schematic picture of the system. The fractured object is represented by a set of atoms and Hooke springs connecting the atoms. The fracture is reproduced by the breaking of the springs [Y. Hayakawa (1995), Fig.1(a)].

by Hooke springs, which can freely rotate around the atoms, as illustrated in Fig.5.7. The interaction by Hookean force between the next nearest neighbor atoms is essential to reproduce the elastic response of the material. Note that the system shows nonlinear response when the deformation applied to the system is large although the system is made of Hooke springs. However, we can regard that the response is linear as far as the deformation is small.

The breaking of the material is simulated by introducing irreversible breaking of the spring at a certain threshold length, which is performed by setting the spring constant of the spring to zero.

The time evolution of the system is performed by straightforwardly solving the equation of motion for each atom. An atom in the system is moving under the action of the sum of force by the springs and dissipative force. The equation of motion for i-th atom is given as

$$\frac{d^2\boldsymbol{r}}{dt^2} = -\gamma\frac{d}{dt}\left[\sum_j(\boldsymbol{r}_i - \boldsymbol{r}_j)\right] + \boldsymbol{F}_i \quad , \tag{5.3}$$

where $\boldsymbol{r}$, γ and $\boldsymbol{F}_i$ denote locations of the atoms, a dissipation rate, and the force by the springs, respectively, and the sum runs over the nearest and next nearest neighbor atoms of the i-th atom. In the model, each atom is set having unit mass and the dissipation rate γ is set small enough so that the characteristic relaxation time becomes longer compared to the simulating time.

By applying a compressive pulse-like load representing an impact onto a side of the cubic lattice, which is realized by applying external force to the side atoms for an instant, the fragmenting process starts from the impact side. Fig.5.8 shows the relation between the location of the breaking of the spring and the time that the breaking occurs. As clearly shown in the figure, there emerges an intensive region of the spring breaking similar to the failure wave, which propagates from the impact side to the opposite side with a constant velocity nearly equal to the speed of elastic longitudinal waves, the speed of

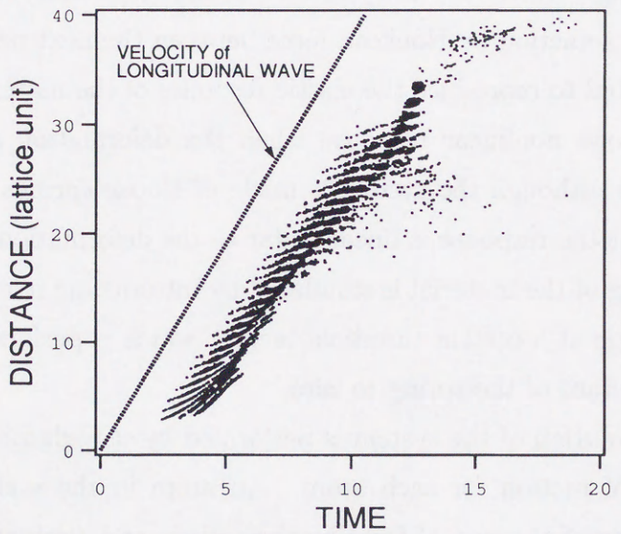

Figure 5.8: The location of the spring breaking versus time. The location is measured by the depth, the distance from the impact side [Y. Hayakawa (1995), Fig.3].

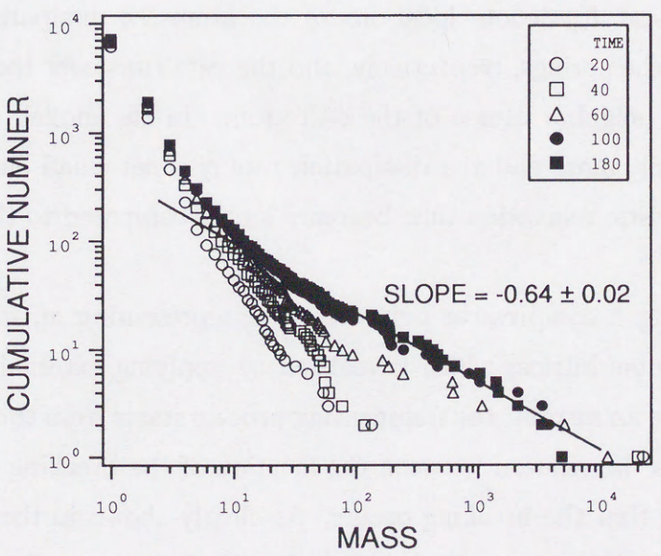

Figure 5.9: The fragment size distribution by the spring model of impact fracture observed at several different time stages [Y. Hayakawa (1995), Fig.5].

sound. This fact implies that the spring breaking occur on a pulse-like elastic longitudinal wave caused by the impact. The intensive breaking region is relatively thin compared to the system size and there is no apparent spring breaking out of the intensive breaking region. In fact, most of the spring breaking occurs during the propagation of the intensive breaking region from the impact side to the opposite.

In Fig.5.9, the cumulative fragment size distribution by the model at several time stages is presented. The distribution converges to a power-law distribution whose exponent is 0.64 ± 0.02 sufficient after the propagation of the intensive breaking region.

As can be seen from the results by the model, the linear elastic deformation with the breaking at threshold deformation seems to be enough for the power-law fragment size distribution.

5.3 Minimal Impact Fracture Model

The numerical model introduced in the previous section seems to well reproduce the power-law fragment size distribution by impact fragmentation. However, since the model is based on the basic equation of motion, it is difficult to figure out the cause of the fractal behavior of the impact fracture process by the mechanism of the model. Our interest is in the common cause of fractal behaviors seen in various systems as well as that of the impact fracture process. In the study of fractal growth systems, it has been clarified that the growth rates of individual growing elements depend on their own relative size, and that it is essential to produce the power-law size distribution of the growing elements. Similarly, if crack dynamics depending on relative fragment size can be extracted from the mechanism of the impact fracture process, it must be the most probable factor to creating the power-law fragment size distribution. To confirm the effects of the extracted dynamics, a minimal model discussed in Sec.2.4 is applicable. In this section, we introduce the minimal model of the impact fracture process [H. Inaoka and H. Takayasu (1995)].

5.3.1 Basic Concept of the Model

The impact fracture process is a complicated process. One of the most complex factors of the process is its three-dimensionality and it is difficult to perform a full three-dimensional simulation because of the limit of computer ability. Fortunately, however, the existence of the failure wave and the result of the numerical model discussed in the previous section imply the possibility that the process can be treated by a set of two-dimensional processes as described in the following.

The situation discussed here is schematically illustrated in Fig.5.10. When an object undergoes an impact, many cracks appear near the impact surface and they propagate to the opposite side of the object forming a failure wave.

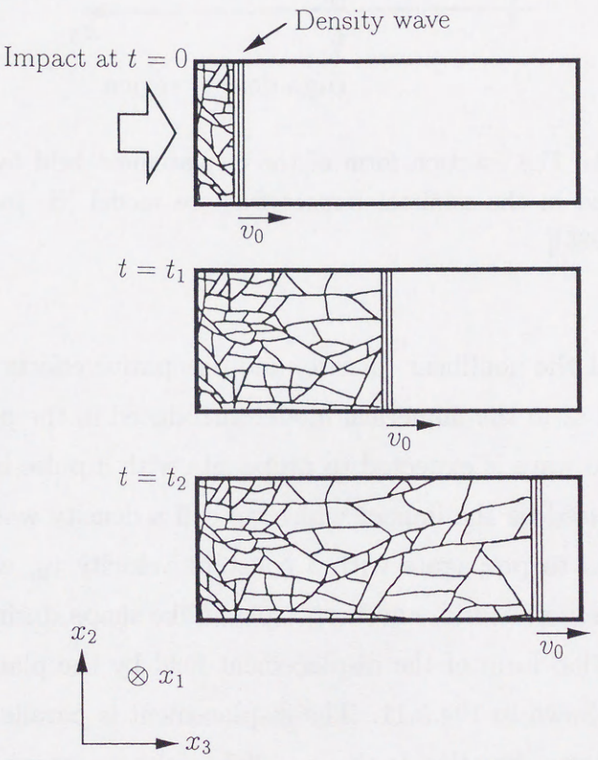

Figure 5.10: A schematic picture of impact fracture process. An impact at $t = 0$ produces a plane density wave as a crack front propagating in the x_3 direction with a constant velocity [H. Inaoka and H. Takayasu (1995)].

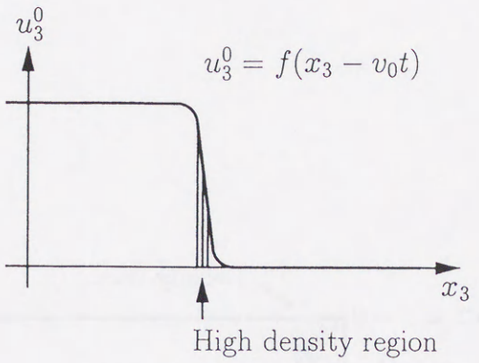

Figure 5.11: The function form of the displacement field by the density wave assumed in the minimal impact fracture model [H. Inaoka and H. Takayasu (1995)].

We assume that the nonlinear, plastic, and dissipative effects of the material is small enough as in the numerical model introduced in the previous section. Then the failure wave is expected to propagate with a pulse-like longitudinal elastic wave caused by the impact which we call a density wave. The density wave is assumed to propagate with a constant velocity v_0, which should be equal to the speed of sound, and keep a plane-like shape during the propagation. The function form of the displacement field by the plane density wave is assumed as shown in Fig.5.11. The displacement is parallel to the x_3 axis and its propagating direction is also parallel to the x_3 axis meaning that the wave is longitudinal compressive. The function is similar to a step function and, within the step region, the density becomes higher than the other place. The region is called a high density region. The high density region is very thin and placed parallel to the x_1-x_2 plane. The displacement field by the plane density wave is denoted by $\boldsymbol{u}^0$. The crack propagation is assumed to occur only within the high density region. This assumption makes it possible to simulate the process by considering the crack dynamics only on the plane density wave.

From Fig.5.5 we notice that the fragments produced near the impact surface tend to be finer than those appearing near the opposite side of the object. Namely, the crack density on the plane density wave seems to decrease as the wave propagates. This decay of crack density is quite natural in view of energy because the crack propagation is a dissipative process and there is no energy injection during the propagation. By this fact, at first, it is also assumed that the cracks are not created and do not bifurcate during the propagation. Then the cracks only move and merge on the propagating plane density wave. The crack density monotonically decreases and, as a result, larger fragments are produced as the fragmenting process proceeds.

While the consideration of the crack dynamics can be limited to the plane density wave, the difficulty of the problem brought by the three-dimensionality can not be eliminated completely because the crack dynamics on the plane density wave must be connected with the strain and stress fields surrounding the cracks: the fields must be solved in three-dimensional space. Fortunately again, the three-dimensional deformation equation can be transformed into a two-dimensional equation by the plane density wave assumption under moderate conditions as follows.

The most general description of material deformation by linear elasticity is the equation of motion with Hooke's law. To produce shock-like wave seen in the fragmenting process of real material, the linear Hooke's law is obviously insufficient. However, since we treat the case that the linear elasticity is dominant, we assume that the Hooke's law can be applicable to all non-crack parts in the object and the cracks determine the boundary condition of the equation. The basic equation is

$$\rho \frac{\partial^2 u_k}{\partial t^2} = \sum_l \frac{\partial}{\partial x_l} \left\{ \lambda \delta_{kl} (\nabla \cdot \boldsymbol{u}) + \mu \left(\frac{\partial u_k}{\partial x_l} + \frac{\partial u_l}{\partial x_k} \right) \right\} \quad , \tag{5.4}$$

where $\boldsymbol{u}$ and u_k denote the displacement vector field and k-th component of the displacement field, and λ, μ, and ρ are Lamé's constants and density,

respectively, with δ_{kl} being Kronecker's delta. It is assumed that the fractured object is nearly homogeneous, i.e., its elastic moduli or Lamé's constants, λ and μ, and mass density, ρ, are nearly constant with very small random spatial fluctuations. Let ϵ be a very small positive parameter. We write λ, μ, and ρ as

$$\lambda = \lambda^0 + \epsilon\lambda^1 \quad , \quad \mu = \mu^0 + \epsilon\mu^1 \quad , \quad \rho = \rho^0 + \epsilon\rho^1 \quad , \tag{5.5}$$

where λ^0, μ^0, and ρ^0 are constants and λ^1, μ^1, and ρ^1 are perturbation fields from the constants, respectively. It will be shown that the results of the simulation do not depend on the magnitude of the randomness later, therefore, the parameter ϵ can take any value so long as it is sufficiently small not violating the assumption of the plane density wave. Because of the small randomness of the material, the displacement field differentiates from $\boldsymbol{u}^0$, namely, the displacement field, $\boldsymbol{u}$, is written using the parameter, ϵ, as

$$\boldsymbol{u} = \boldsymbol{u}^0 + \epsilon\boldsymbol{u}^1 \quad , \tag{5.6}$$

where $\boldsymbol{u}^1$ is perturbation displacement field caused by the randomness of the material. Substituting Eqs.(5.5) and (5.6) into Eq.(5.4), the equation for the first order of ϵ is derived as follows:

$$\begin{aligned} \rho^0\frac{\partial^2\boldsymbol{u}^1}{\partial t^2} + \rho^1\frac{\partial^2\boldsymbol{u}^0}{\partial t^2} &= (\lambda^0+\mu^0)\nabla(\nabla\cdot\boldsymbol{u}^1) + \mu^0\nabla^2\boldsymbol{u}^1 \\ &+ \left\{\frac{\partial^2 u_3^0}{\partial {x_3}^2}(\lambda^1+2\mu^1) + 2\frac{\partial u_3^0}{\partial x_3}\frac{\partial\mu^1}{\partial x_3}\right\}\boldsymbol{e}_3 + \frac{\partial u_3^0}{\partial x_3}\nabla\lambda^1 \quad , \end{aligned} \tag{5.7}$$

where $\boldsymbol{e}_3$ is a unit vector parallel to the x_3 axis. We transform the equation by changing the coordinate to a moving coordinate whose x_1-x_2 plane is just on the middle of the high density region and observe only the x_1-x_2 components of $\boldsymbol{u}^1$. The term $\frac{\partial^2 u_3^0}{\partial {x_3}^2}$ is assumed to be zero on the center of the high density region as known from Fig.5.11. The inertial terms, the left hand side terms of Eq.(5.7), can not be neglected when we discuss wave propagation. The inertial term $\rho^1\frac{\partial^2\boldsymbol{u}^0}{\partial t^2}$, which is directed to the x_3 axis, and x_3 component of $\rho^0\frac{\partial^2\boldsymbol{u}^1}{\partial t^2}$ is

taken into account, but they do not contribute to the crack dynamics because only the x_1 and x_2 components of the deformation on the plane density wave is assumed to have effects to the crack dynamics in the model. As for the x_1 and x_2 components of the term $\rho^0 \frac{\partial^2 \boldsymbol{u}^1}{\partial t^2}$, we neglect them because waves propagating in the direction parallel to the x_1-x_2 plane on the plane density wave are expected to be disturbed severely by the cracks and they may not have significant effect to the model. Then the following equation is derived from Eq.(5.7):

$$(\lambda^0 + \mu^0)\nabla_\perp(\nabla_\perp \cdot \boldsymbol{u}^1_\perp) + \mu^0 {\nabla_\perp}^2 \boldsymbol{u}^1_\perp + \frac{\partial u^0_3}{\partial x_3}\nabla_\perp \lambda^1 = \mathbf{0}_\perp \quad , \tag{5.8}$$

where the subscript $\perp$ denotes that the vectors and operators are perpendicular to the x_3 axis. The two-dimensional displacement field $\boldsymbol{u}^1_\perp$ is generally decomposed into divergence-free part ($\nabla \cdot \boldsymbol{u}^{1,\mathrm{d}}_\perp = \mathbf{0}_\perp$) and rotation-free part ($\nabla \times \boldsymbol{u}^{1,\mathrm{r}}_\perp = \mathbf{0}_\perp$). It is shown that the divergence-free part is determined independently of the non-uniformity λ^1, which suggests that the divergence-free part is irrelevant. By neglecting the divergence-free field, we get following equation:

$${\nabla_\perp}^2 \phi(x_1, x_2, t) = -\theta(x_1, x_2, v_0 t) \quad , \tag{5.9}$$

where ϕ and θ are scalar potentials introduced by

$$\nabla_\perp \phi(x_1, x_2, t) = \boldsymbol{u}^{1,\mathrm{r}}_\perp(x_1, x_2, t) \quad , \tag{5.10}$$

$$\nabla_\perp \theta(x_1, x_2, v_0 t) = \frac{1}{\lambda^0 + 2\mu^0}\frac{\partial u^0_3}{\partial x_3}\nabla_\perp \lambda^1(x_1, x_2, v_0 t) \quad . \tag{5.11}$$

The form of the equation Eq.(5.9) is identical to that of the equation in the static elasticity, where ϕ and θ correspond to the displacement potential and the dilation field, respectively. However, we should note that the cause of the dilation field in this problem is quite different from that in the static elasticity. As known from Eq.(5.11), the term $\frac{\partial u^0_3}{\partial x_3}\lambda^1$ causes the dilation on the density wave plane, namely, the compression in the x_3 direction causes non-uniform

pressure and resulting dilation on the density wave plane, which is assumed to govern the dynamics of the cracks directly. The dilatant behavior around the failure wave is also observed in experiments as introduced in Sec.5.1. The boundary condition of Eq.(5.9) is assumed as

$$\phi(x_1, x_2, t) = 0 \tag{5.12}$$

on the cracks. The physical meaning of the condition is that the displacement near the cracks are perpendicular to the cracks.

Thus the three-dimensional impact fracture process can be treated as a sequence of the two-dimensional processes. In the model, the crack propagation in the three-dimensional objects is treated as a time evolution of the configuration of the cracks in two-dimensional space. Since only the configuration of the cracks on the plane density wave is treated in the model, we should note that a region which encircled by the cracks in the model is not a fragment itself but a section of the fragment by the plane density wave. To construct a fragment itself, we have to pile the fragment section at each moment in time order.

The remaining problem is the nature of the crack dynamics. In a quasi-static fracture process, cracks are considered to propagate in the direction such that the stress intensity factor K_{II} vanishes. However, the stress intensity factor is a concept in the static elasticity and it is not certain whether it can be applied to a dynamic process like the impact fracture. So a proper dynamics of the crack propagation which can produce the power-law fragment mass distribution have to be assumed. A hint for the problem is in the knowledge of fractal growth systems. As discussed in Chapter 3, one of the most essential factors for the fractal behaviors in the fractal growth systems is the competitive growth process of the growing elements. In the impact fracture process, the quantity which follows a power-law distribution is the size of the fragments, especially, the mass of the fragments. Therefore, the fragments are assumed

to be under a competitive process.

Let us introduce a flux density field by the gradient field of the Poisson field ϕ. The flux density field is identical to the displacement field, $\boldsymbol{u}_{\perp}^{1,\mathrm{r}}$. By the nature of the Poisson's equation Eq.(5.9), each surface element, ds, in a fragment section generates the flux of magnitude $-\theta\, ds$, and the flux propagates toward the edge of the fragment section conserving the flux intensity. Thus the flux or the displacement field transmits the information about the size of the fragment section to the cracks. The cracks must have dynamics controlled by the displacement field. So, if the dynamics has a property that a larger fragment section can expand its area faster, then a competitive growth process similar to that in the fractal growth systems must occur and the resulting fragments are expected to form a power-law size distribution.

5.3.2 Model Description

The model is defined on a two-dimensional triangular lattice which represents the propagating plane density wave, and the configuration of the cracks and the fragment sections are considered on it. Each lattice site, (x_1, x_2), has three variables: fragment number, $N_f(x_1, x_2, v_0 t)$; displacement potential, $\phi(x_1, x_2, t)$; and dilation field, $\theta(x_1, x_2, v_0 t)$. Hereafter, v_0 is set to be unity in the model, therefore, time, t, and depth $x_3 = v_0 t$ are regarded as identical. The sites which have the same fragment number are regarded that they belong to the section of the same fragment. That is, the fragment number $N_f(x_1, x_2, x_3)$ is an indicator of the individual fragments and it means that there is a crack between any two adjacent sites having different fragment numbers each other. An example of the configuration is shown in Fig.5.12. The displacement potential $\phi(x_1, x_2, x_3)$ is determined by solving Eq.(5.9) under the boundary condition Eq.(5.12) on the cracks, and the displacement field $\boldsymbol{u}_{\perp}^{1,\mathrm{r}}(x_1, x_2, x_3)$ is introduced by Eq.(5.10). The randomness of the material of the fractured objects is introduced through the dilation field $\theta(x_1, x_2, x_3)$,

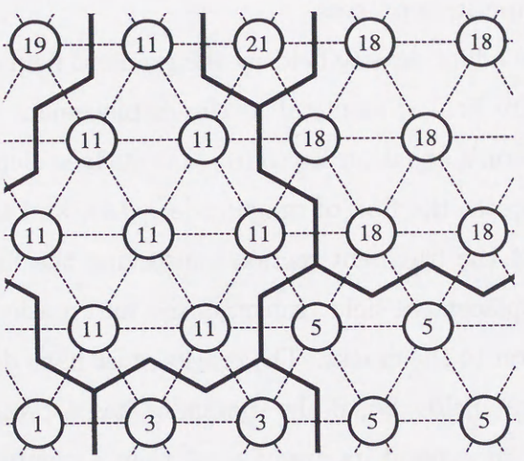

Figure 5.12: A schematic figure of the relation of the fragment numbers, the fragment sections, and the cracks. The circles and the numbers encircled show the sites and the fragment numbers, respectively. The lines show cracks [H. Inaoka and H. Takayasu (1995)].

namely, a random number is generated and assigned to the value of the dilation field at each site.

The dynamics of the cracks is introduced as follows. As mentioned above, cracks are defined on the boundaries of the distinct fragment sections. We calculate the magnitudes of the displacement, $|\boldsymbol{u}_{\perp}^{1,\mathrm{r}}(x_1, x_2, x_3)|$, on a crack from fragment sections on both sides and compare them. The crack is assumed to move by one site toward the site having the smaller value of $|\boldsymbol{u}_{\perp}^{1,\mathrm{r}}(x_1, x_2, x_3)|$.

The simulation is started from the initial condition that each site in the system belongs to a different fragment, which physically means that the impact surface is completely destroyed. Note that, in the model, all the fragments in the system have their roots in the initial plane because of the lack of the creation and the bifurcation of the cracks. The edges of the whole system are connected by a periodic boundary condition.

Starting from the initial condition, the time evolution of the system is performed by repeating the following procedures:

1. For each site (x_1, x_2), a random number distributing uniformly in the interval [1.0 , 1.5) is assigned to $\theta(x_1, x_2, x_3)$.

2. The displacement potential $\phi(x_1, x_2, x_3)$ is solved by a relaxation method.

3. The sites which are at the edges of the fragment sections are extracted from the system and make a set of sites, A.

4. For each site $(x_1, x_2) \in A$, a set of neighboring sites, U, which consists of the site (x_1, x_2) itself and six nearest neighbors of the site (x_1, x_2) is made. Then the site, (x_1', x_2', x_3), which have the largest value of the displacement potential ϕ in the set of $U \cap A$ is chosen. The fragment number $N_f(x_1, x_2, x_3)$ is renewed by $N_f(x_1', x_2', x_3)$.

These procedures make one time step and they are repeated with an increased x_3 by 1. In the following discussion we call this model a basic model.

5.3.3 Numerical Results

As mentioned previously, a snapshot of the system corresponds to the section of the system parallel to the plane density wave in the model. To get a cross section perpendicular to the density wave, we have to observe the time evolution of the configuration of the fragment numbers on a set of sites forming a straight line. Fig.5.13 shows a typical crack pattern observed on the sections by the model. The cross section parallel to the density wave, Fig.5.13(a), shows a configuration of fragment sections at a certain depth. There appear fragment sections having nearly the same size each other. Contrasted with the figure, the cross section perpendicular to the density wave, Fig.5.13(b), shows many fine fragments near the initial plane on the top and a few large ones located away from the initial plane indicating that the system contains fragments of various size. In the model, the quantity which corresponds to the volume of the fragments in a real fracture process is the integration of the

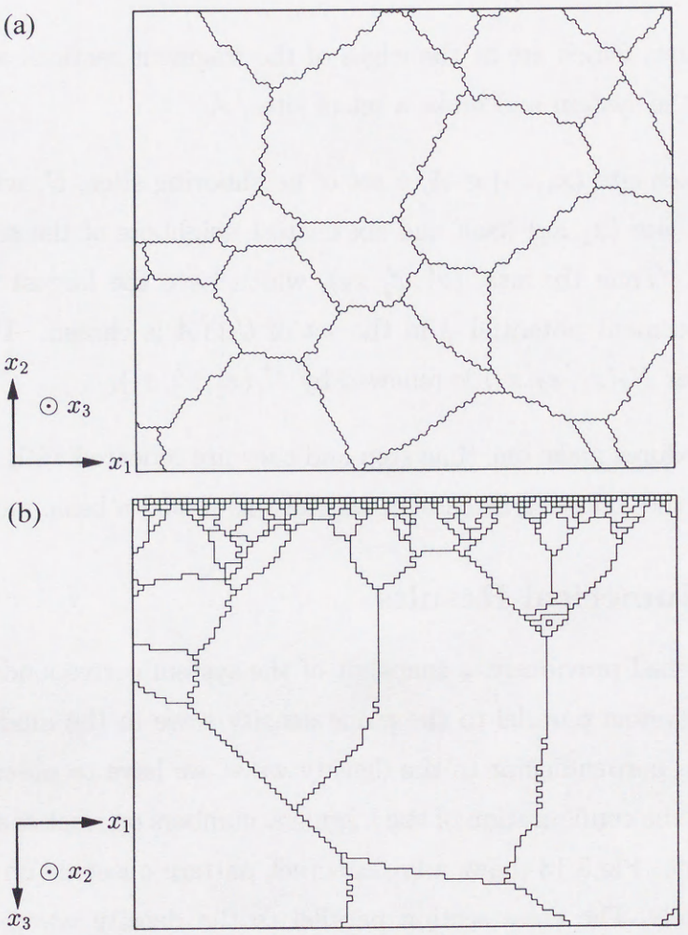

Figure 5.13: (a) A snapshot of the system of the basic model. The solid lines show cracks. (b) A section perpendicular to the plain density wave. The time is shown in the direction from the top to the bottom [H. Inaoka and H. Takayasu (1995)].

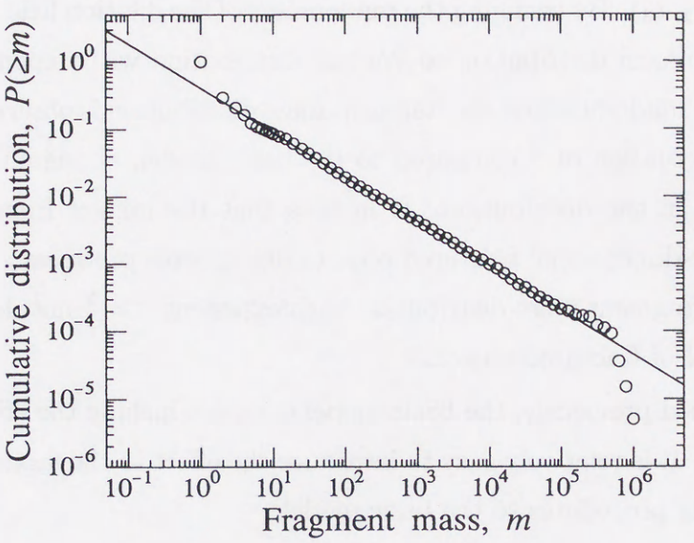

Figure 5.14: The cumulative distribution of the fragment mass in the basic model in log-log scale. The solid line shows a power-law distribution as $P(\geq m) \propto m^{-0.66}$ [H. Inaoka and H. Takayasu (1995)].

fragment section area to the time. During the simulation, the number of the sites which belong to each fragment section at each time step is counted up and it is summed up throughout all the evolution time steps. The sum is regarded as the volume or the mass of the fragment. The cumulative fragment mass distribution in the model is shown in Fig.5.14 in log-log scale. In Fig.5.14, the dots are clearly on a straight line in the mass range from 10 to 10^5 indicating that the cumulative fragment mass distribution follows a power-law as

$$P(\geq m) \propto m^{-\tau} \quad , \quad \tau = 0.66 \quad , \tag{5.13}$$

where m and $P(\geq m)$ denote the fragment mass and the probability that a randomly chosen fragment has mass larger than or equal to m, respectively. The value of the exponent $\tau = 0.66$ is very close to $\frac{2}{3}$, and such exponent value has been often observed in experimental situations as discussed in Sec.5.1.

In the model, the nature of the material is reflected only through the dilation

field $\theta(x_1, x_2, x_3)$. By changing the randomness of the dilation field $\theta(x_1, x_2, x_3)$ from the uniform distribution to Weibull distribution with exponent 0.2, the effect of the randomness on the fragment mass distribution is observed. In spite of large fluctuation of θ compared to the basic model, no significant change is observed in the distribution. It implies that the impact fracture process in the three-dimensional fractured objects like spheres produces a cumulative power-law fragment mass distribution with exponent $\tau = \frac{2}{3}$ not depending on the material of fractured object.

As assumed previously, the basic model does not include the effect of crack bifurcation. It is relatively easy to introduce the effect to the model by adding the following procedures to the basic model:

5. A fragment edge site set E is made by the similar way to the procedure 3.

6. For each site $(x_1, x_2) \in E$, the site is regarded to belong to subset of E, E', with probability c.

7. For each site $(x_1, x_2) \in E'$, a brand-new number is assigned to the fragment number $N_f(x_1, x_2, x_3)$.

Namely, these procedures add new fine fragment sections near the cracks. Applying Weibull distribution with exponent 0.2 to the dilation field $\theta(x_1, x_2, x_3)$, the modified model is simulated with $c = 0.1$. The distribution has a power-law tail with exponent 0.68, and relatively lager number of fine fragments appear compared to the result in the basic model. So the effect of the crack bifurcation of this type does not significantly modify the power-law tail of the distribution.

Thus the exponent of the fragment mass distribution seems to have robust universality with respect to the randomness of the material and the crack bifurcation.

5.3.4 Universality in Fragment Size Distribution

As discussed above, the value of the exponent, $\tau = \frac{2}{3}$, of the fragment mass distribution by the full three-dimensional impact fracture process seems to be universal.

Let us consider the time evolution of a locally largest fragment with the fragment number $N_f(x_1, x_2, x_3) = n_f$. The total dilation in the fragment, Θ, at a moment x_3 is defined as

$$\Theta \equiv \sum_{N_f(x_1,x_2,x_3)=n_f} \theta(x_1, x_2, x_3) \quad , \tag{5.14}$$

where the sum runs over the sites which belong to the fragment section numbered n_f. From Gauss's theorem, in the continuous limit of the system, the following equation holds:

$$\oint u_\perp \, dl \; = \; -\Theta \quad , \tag{5.15}$$

where $u_\perp$ and dl denote the normal component of $\boldsymbol{u}_\perp^{1,\mathrm{r}}$ to the crack and line element, respectively, and the integral runs along the crack encircling the fragment section. For simplicity, we assume the isotropy of the fragment section shape and, for a moment, the uniformity of the dilation field $\theta(x_1, x_2, x_3)$. The physical meaning is that the shape of the fragment section is a circle and the dilation field $\theta(x_1, x_2, x_3)$ has no fluctuation. Then, using Eq.(5.15) and the symmetry, the relation between the magnitude of the displacement at the edge of the fragment section and the total dilation is simply written as

$$|\boldsymbol{u}_\perp^{1,\mathrm{r}}| \; \propto \; \Theta S^{-\frac{1}{2}} \quad , \tag{5.16}$$

where S denotes the area of the fragment section. In fact, the dilation field $\theta(x_1, x_2, x_3)$ is generated by a uniform random number in the basic model, that is, Θ is a stochastic variable which consists of the sum of $\theta(x_1, x_2, x_3)$ over S sites. The expectation of Θ, $\langle\Theta\rangle$, is written using the expectation of θ, $\langle\theta\rangle$, as

$$\langle\Theta\rangle \; = \; \langle\theta\rangle S \quad , \tag{5.17}$$

where θ is an independent stochastic variable being assigned to $\theta(x_1, x_2, x_3)$. On the other hand, the fluctuation or the standard deviation of Θ, $\langle \Delta\Theta \rangle$, holds the following relation when the standard deviation of θ, $\langle \Delta\theta \rangle$, has a finite value:

$$\langle \Delta\Theta \rangle \;=\; \langle \Delta\theta \rangle S^{\frac{1}{2}} \quad . \tag{5.18}$$

In the limit of large S, the fluctuation of Θ becomes relatively small compared to the expectation of Θ, i.e.,

$$\lim_{S\to\infty} \frac{\langle \Delta\Theta \rangle}{\langle \Theta \rangle} \;=\; \lim_{S\to\infty} \frac{\langle \Delta\theta \rangle S^{\frac{1}{2}}}{\langle \theta \rangle S} \;=\; 0 \quad . \tag{5.19}$$

So, for large S, it is regarded that the magnitude of the displacement, $|\boldsymbol{u}_{\perp}^{1,\mathrm{r}}|$, at the fragment edge almost certainly follows a relation

$$|\boldsymbol{u}_{\perp}^{1,\mathrm{r}}| \;\propto\; S^{\frac{1}{2}} \tag{5.20}$$

from Eqs.(5.16) and (5.17).

In the model, the cracks move by one site at a time step toward the place having smaller magnitude of the displacement. By the rule, the locally largest fragment section almost certainly expands its section radius by one site at a time step because, from Eq.(5.20), the magnitude of the displacement $|\boldsymbol{u}_{\perp}^{1,\mathrm{r}}|$ at the edge of the fragment section is a monotonically increasing function of S, $S^{\frac{1}{2}}$. Using a monotonically increasing function of $|\boldsymbol{u}_{\perp}^{1,\mathrm{r}}|$, $F(|\boldsymbol{u}_{\perp}^{1,\mathrm{r}}|)$, the dynamics of the cracks such as the cracks move by one site at a time step toward the place having a smaller value of $F(|\boldsymbol{u}_{\perp}^{1,\mathrm{r}}|)$ can be considered. Even in this case, the situation that the locally largest fragment section can expand its radius is not changed. So the generalization of the model in this direction results the same competitive dynamics of the fragments as the basic model.

By the nature of the crack dynamics in the basic model, the locally largest fragment expands its section area with the square of the time steps. Fig.5.15 shows a log-log plot of the time evolution of the mean fragment section area,

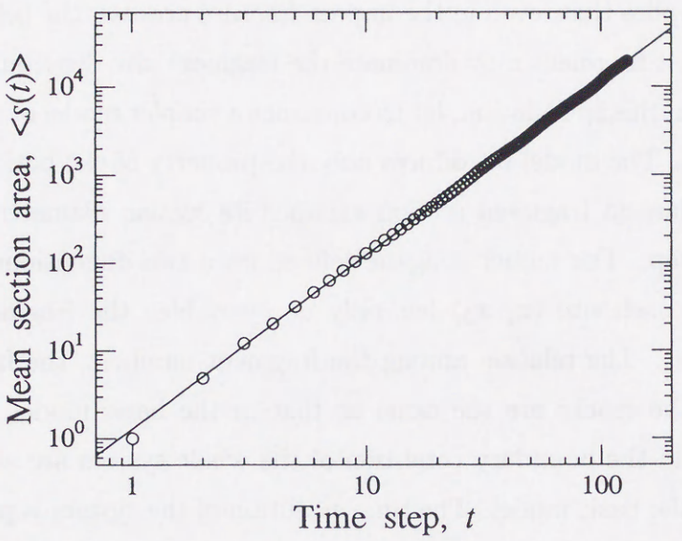

Figure 5.15: The time evolution of the mean fragment section area in log-log scale. The solid line shows a power-law expansion of the mean fragment section area as $\langle s(t) \rangle \propto t^{1.98}$ [H. Inaoka and H. Takayasu (1995)].

$\langle s(t) \rangle$, defined as

$$\langle s(t) \rangle \equiv \frac{\sum_i s_i(t)^2}{\sum_i s_i(t)} \quad , \tag{5.21}$$

where t, i, and s_i denote the time step, the fragment number, and the section area of the fragment numbered i, respectively. By definition, the mean fragment section area $\langle s(t) \rangle$ describes the behaviors of relatively large fragment sections. The dots are on a straight line indicating the power-law expansion of the mean fragment section area as

$$\langle s(t) \rangle \propto t^z \quad , \tag{5.22}$$

where $z = 1.98$ which is very close to 2. This result implies the validity of the above discussion.

As discussed in Sec.3.2, the minimal competitive growth model generates a power-law distribution depending on the competitive dynamics, and the dynamics is well grasped by studying the behavior of the largest growing element.

This fact implies that, even in the impact fracture process, the behavior of the locally largest fragment may dominate the fragment size distribution.

To confirm this speculation, let us construct a simpler model of the fragment competition. The model introduces only the property of the basic model that the locally largest fragment section expands its section diameter by one site at a time step. The model is again defined on a two-dimensional triangular lattice, and each site (x_1, x_2) has only one variable: the fragment number, $N_f(x_1, x_2, x_3)$. The relation among the fragment numbers, the fragment sections, and the cracks are the same as that in the basic model. The initial condition and the boundary condition of the whole system are also the same as those in the basic model. The time evolution of the system is performed by repeating the following procedures:

1. For each fragment, the fragment section area, s, is calculated. Then the fragments are sorted by the magnitude of the section area s. If there are more than one fragments which have the same s, they are randomly ordered within the fragments which have the same s.

2. The set, A, is determined as in the basic model.

3. For each site (x_1, x_2) which belongs to A, we make a set of neighboring sites, U, as in the basic model. For the member of the set $U \cap A$, a site (x_1', x_2') which belongs to the fragment which appears in the earliest order in the sort by the procedure 1 is chosen. The fragment number of the site (x_1, x_2) is renewed by $N_f(x_1', x_2', x_3)$.

4. In the procedure 3, if there emerge fragments which have no section area on the lattice, then the fragments are removed from the procedures.

The cumulative fragment mass distribution in this simplified model follows a power law with exponent $\tau = 0.67$. The value of the exponent is close to $\frac{2}{3}$ as expected.

From the above discussion, it is concluded that the competition process in which the locally largest fragments expand their section area proportionally to t^2 produce the power-law fragment mass distribution with exponent $\tau = \frac{2}{3}$.

5.3.5 Fractal Dimension

Let us extract the largest fragment section from Figs.5.13(a) and (b) and analyze the fractal dimensions of the sections of the fragment periphery by the box-counting method. The result is shown in Fig.5.16. The fractal dimensions, D, of the fragment periphery sections parallel and perpendicular to the density wave are both observed to be very close to 1.0. The result shows that the fractal dimension of the periphery of a fragment is 2, the fractal dimension for an ordinary surface. Namely, each fragment in the model does not have fractal property.

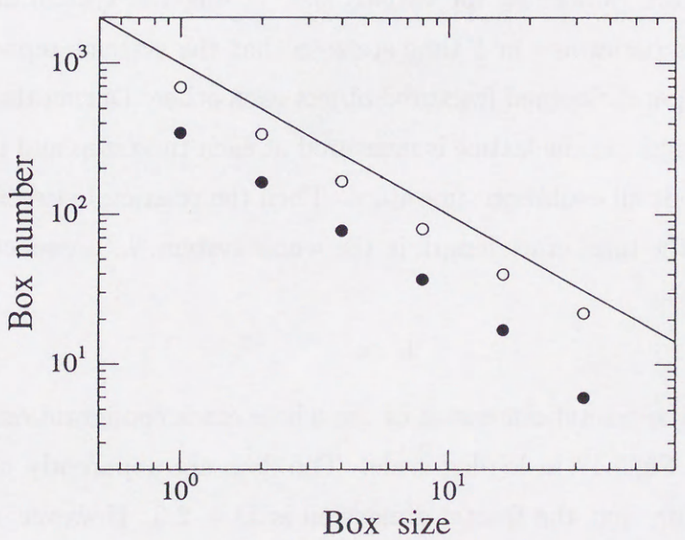

Figure 5.16: The results by the box-counting method applied to the sections of the fragment periphery by planes parallel(○) and perpendicular(●) to the density wave. The solid line shows a slope of $D = 1.0$ [H. Inaoka and H. Takayasu (1996), Fig.3]

A kind of self-similarity is, however, recognized from Fig.5.13(b) as follows. The upside of Fig.5.13(b) corresponds to the section of the impact surface of the fractured object. Let us consider a rectangular part of Fig.5.13(b) which has one of its sides on the section of the impact surface. Expanding the rectangular part properly, it is found that the expanded configuration of the fragment sections seems to have a similarity to the original Fig.5.13(b). This fact implies that the fragments in the system are similar in shape each other and they construct a self-similar structure as a whole though each of them does not have fractal property. Thus the self-similarity of the system requires a unique way for observation, that is, only a rectangular parallelepiped region of the system which has a part of the impact surface as one of its plane is similar to the whole system. So the box-counting method is not suitable for the estimation of the fractal dimension of the whole crack configuration.

To estimate the fractal dimension of the whole configuration of the cracks, simulations are performed for various size. Using the system of size r, the simulation is performed in $\frac{r}{2}$ time steps so that the systems represent similar rectangular parallelepiped fractured object each other. During the simulation, the crack length on the lattice is measured at each time step and it is summed up throughout all evolution time steps. Then the relation between the system size, r, and the total crack length in the whole system, L, is expected to follow a power law as

$$L \propto r^D \quad , \tag{5.23}$$

where D is the fractal dimension of the whole crack configuration. The result is shown in Fig.5.17 in log-log scale. The dots are apparently on a straight line indicating that the fractal dimension is $D = 2.3$. However, a dimension analysis approach to the problem gives another result.

By Eq.(5.22), the number of the fragment sections, N, and the total crack length on the density wave, l, decrease as $N \propto t^{-2}$ and $l \propto N \cdot t \propto t^{-1}$, respectively. Since all the fragments in the model have their roots on the hit

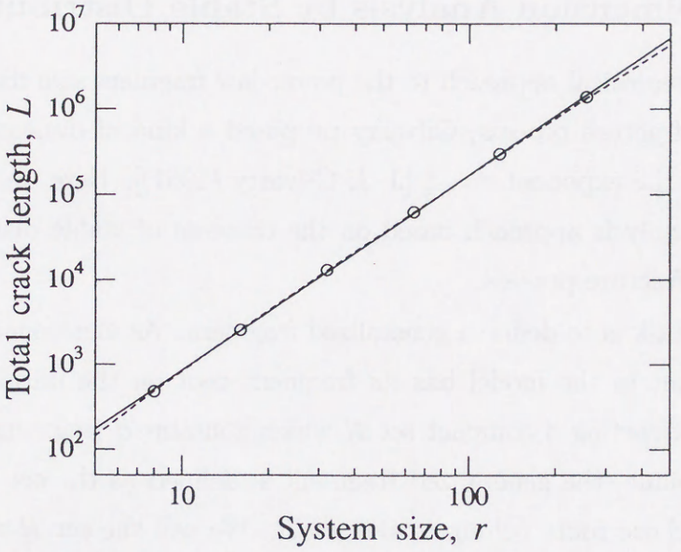

Figure 5.17: The relation between the system size and the total crack length in log-log scale. The solid line shows a relation $L \propto r^{2.3}$ and the dashed line shows the results by a dimension analysis $L \propto r^2 \ln r$ [H. Inaoka and H. Takayasu (1996), Fig.4].

surface of the fractured object, the section number N has a relation with the dimension of the object r as $N \propto r^2$. Then the total crack length in the whole system, L, scales as

$$L \propto \int_{\epsilon}^{\frac{r}{2}} r^2 t^{-1}\, dt \propto r^2 \ln r \quad , \tag{5.24}$$

where ϵ denotes the lattice constant of the model. The result is also shown in Fig.5.17 by a dashed line and it also seems to fit the dots. The difference between $r^{2.3}$ and $r^2 \ln r$ is very subtle in the observed range and we have to perform larger scale simulations to clarify it. However, it is difficult to perform them at present because of the lack of computer ability.

5.3.6 Dimension Analysis by Stable Distribution

For the theoretical approach to the power-law fragment size distribution in the impact fracture process, Gilvarry proposed a kind of dimension analysis and derived the exponent $\tau = \frac{2}{3}$ [J. J. Gilvarry (1961)]. Here, we introduce a dimension analysis approach based on the theorem of stable distribution for the impact fracture process.

Our first task is to define a generalized fragment. As mentioned previously, each fragment in the model has its fragment root on the initial plane. By randomly extracting a compact set R which contains σ fragment roots from the initial plane, the generalized fragment is defined as the set of the usual fragments whose roots belong to the set R. We call the set R a generalized root.

Let us consider a scaling of generalized fragment mass, $m(\sigma)$, defined as

$$m(\sigma) \equiv \sum_{i \in R} m_i \quad , \tag{5.25}$$

where i and m_i denotes the fragment number and the fragment mass of i-th fragment, respectively, and the sum runs over the fragments whose roots belong to the set R. From the relation Eq.(5.22), it is known that the locally largest fragment expands its size as

$$s \propto t^2 \quad , \quad m \propto s \cdot t \propto t^3 \quad , \tag{5.26}$$

where s, m, and t are the fragment section area, the fragment mass, and the time step, respectively. The relation Eq.(5.26) means the usual relation of the mass or the volume of the fragment and the fragment section area as $m \propto s^{\frac{3}{2}}$. Considering the situation that a fragment is expanded by a factor of $\sigma^{\frac{1}{2}}$ in all dimensions, the mass of the fragment is expanded by the factor of $\sigma^{\frac{3}{2}}$ and the area of the fragment root which is originally 1 becomes σ. By assuming a kind of self-similarity in the mass distribution, the distribution of the generalized

fragment mass is expected to follow a relation

$$m(\sigma) \stackrel{d}{=} \sigma^{\frac{3}{2}} m(1) \quad , \tag{5.27}$$

where $\stackrel{d}{=}$ denotes that the stochastic variables of both sides follow the same distribution and $m(1)$ is identical to the usual fragment mass. This relation describes the self-similarity in the system in terms of stochastic variables.

Next, we consider two generalized fragments whose generalized roots, R_1 and R_2, are located adjacently on the initial plane. The generalized roots R_1 and R_2 contain σ_1 and σ_2 fragment roots, respectively. As can be seen from Fig.5.13, there is no aperture between any two fragments. This fact leads to the consequence that the mass of the generalized fragment whose generalized root is given by the combination of R_1 and R_2 is equal to the sum of the mass of the original two generalized fragments. By this fact, a relation

$$m(\sigma_1 + \sigma_2) \stackrel{d}{=} m(\sigma_1) + m(\sigma_2) \tag{5.28}$$

is assumed even in the case that the generalized roots R_1 and R_2 are not adjacently located.

The theorem of stable distribution states that an independent stochastic variable which satisfies the relations Eqs.(5.27) and (5.28) simultaneously follows a stable distribution [W. Feller (1966)] having a power-law tail as

$$P(\geq m) \propto m^{-\tau} \quad , \quad \tau = \frac{2}{3} \quad . \tag{5.29}$$

Thus, if the independence of the m as a stochastic variable is confirmed, the exponent of the fragment mass distribution $\tau = \frac{2}{3}$ is derived theoretically.

The problem is whether the assumptions adopted in the above discussion, the relations Eqs.(5.27) and (5.28) and the independence of the fragment mass as a stochastic variable, are valid in the system or not. In Fig.5.18 and 5.19, the cumulative distribution of rescaled generalized fragment mass, $m_\times$, and

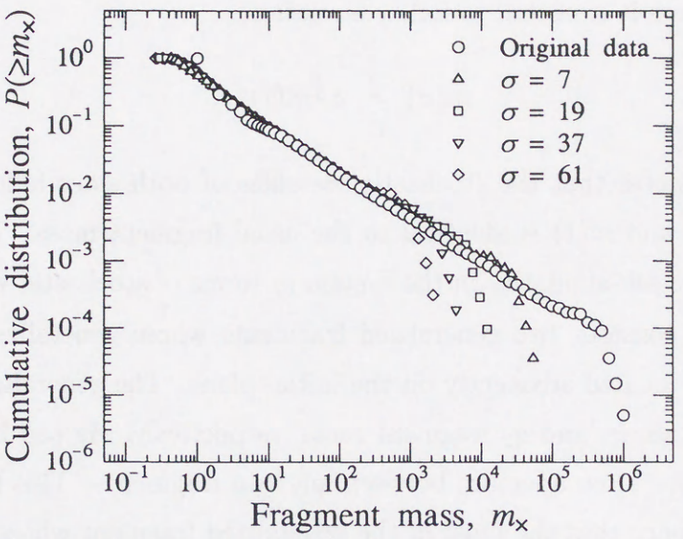

Figure 5.18: The cumulative distribution of the rescaled generalized fragment mass for various values of σ in log-log scale [H. Inaoka and H. Takayasu (1995)].

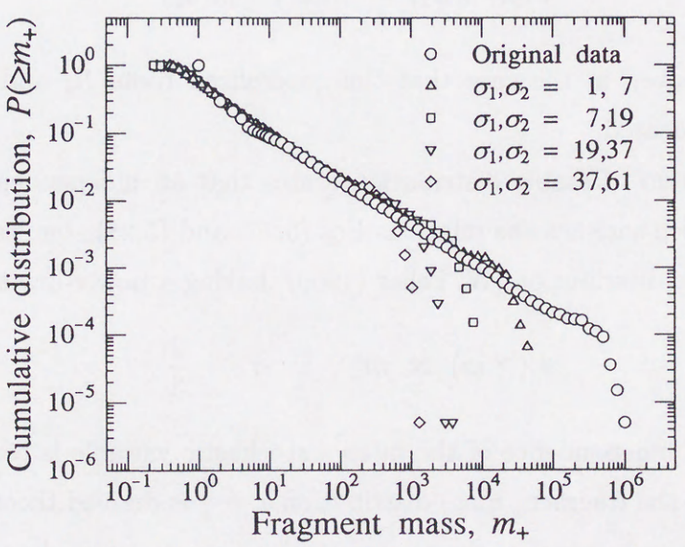

Figure 5.19: The cumulative distribution of the rescaled summation of the generalized fragment mass for various combinations of σ_1 and σ_2 in log-log scale [H. Inaoka and H. Takayasu (1995)].

rescaled summation of the generalized fragment mass, m_+, defined as

$$m_\times \equiv \sigma^{-\frac{3}{2}} m(\sigma) \quad , \tag{5.30}$$

$$m_+ \equiv (\sigma_1 + \sigma_2)^{-\frac{3}{2}} \{m(\sigma_1) + m(\sigma_2)\} \tag{5.31}$$

are plotted for various values of σ, σ_1, and σ_2 in log-log scale, respectively. The dots in both the results are on the identical distribution which is identical to the usual fragment mass distribution indicating that the first two assumptions are valid. While the third assumption, the independence of the fragment mass, is obviously doubtful. Extracting the fragments having mass larger than or equal to a certain threshold mass, m_t, the mass distribution of the fragments whose fragment roots are located adjacently to the fragment roots of the extracted fragments is observed. If the independence is also valid, then the conditional distributions of the fragment mass are identical not depending on the values of m_t. The results are plotted in Fig.5.20 in log-log scale. As clearly shown in the figure, there is a tendency that a large fragment is followed by fine neighbors,

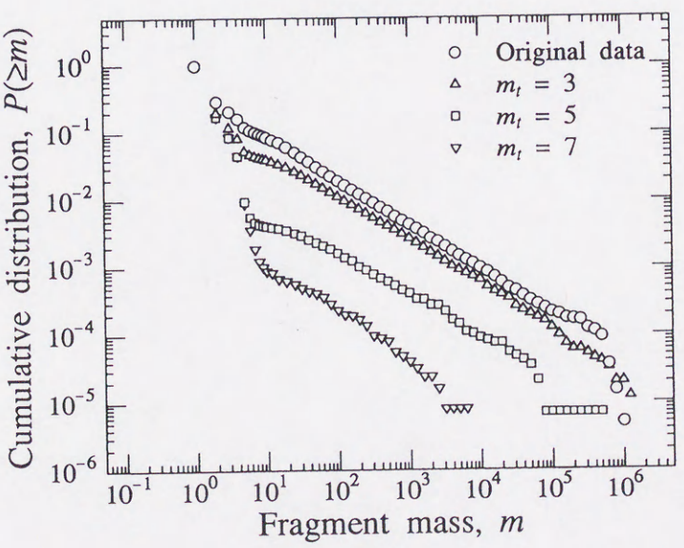

Figure 5.20: The cumulative conditional distribution of the fragment mass for various thresholds m_t in log-log scale [H. Inaoka and H. Takayasu (1995)].

so the distribution depends on the value of m_t. Thus the independence of the fragment mass as a stochastic variable is not valid in the system.

In spite of the dependence of the fragment mass as a stochastic variable, the approach gives the right result, Eq.(5.29). This fact implies the effectiveness of the application of the theorem of stable distribution to the model.

Chapter 6
Conclusion and Remarks

6.1 Summary for Minimal Fractal Models

In this doctoral dissertation, we studied three fractal systems: Laplacian fractals, river networks, and impact fracture. We treated them as competitive fractal growth systems and proposed minimal models for them.

In Sec.3.2 we studied the minimal competitive growth model imitating the competitive growth process in Laplacian fractals. We clarified that the competition is for the one-dimensional flux source in the case of Laplacian fractals in two-dimensional space. It was found that the trajectories of the flux source boundaries draw a self-affine domain configuration on space-time plane as shown in Fig.3.9.

In Sec.4.3 we pointed out that the erosion process and the formation of river networks can be regarded as a competitive fractal growth process. We discussed the fractal features of the river networks. We found that the fractal dimension of each individual drainage basin is 2: the fractal dimension of an ordinary plane. However, the correction of the drainage basins was found to show non-trivial self-affine nature.

We also proposed a model of the three-dimensional impact fracture process in Sec.5.3. In the model, the fracture process is treated as a competitive growth process of the fragment sections on the plane density wave. We also found that each fragment in the model shows no fractal property but the set of the fragments forms a self-similar configuration in three-dimensional space.

We mainly focused on the power-law size distribution of the growing elements in the systems. These three cases have similar property on the point that the competitive processes produce self-similar or self-affine domain configurations. Since the size of the growing element is directly related to the area or the volume of the domain in these three models, the power-law size distribution is deeply related to the self-similar or self-affine domain configuration.

In the following section, we prove that the system of the river networks is at

a self-organized critical state discussed in Sec.2.1. We discuss the second order phase transition in a random branching process. As we can see from Fig.4.18, a drainage basin in the lattice river network models corresponds to a stream branch filling the basin. We show that the stream branch can be regarded as a kind of random branching process and the space-filling condition gives the critical condition of the random branching process. From this point of view, river networks are always at the critical point of the random branching process.

Then we discuss the nature of the self-similar or self-affine space-filling domain configurations seen in the minimal models. We call such a domain configuration fractal tiling. We show that the fractal tiling produces a power-law domain area distribution whose exponent depends on the exponent for the self-affine nature of the fractal tiling.

6.2 Random Branching Process

In this section we introduce a simple random branching process. The random branching process shows a second order phase transition. At the critical point of the process, a power-law branch size distribution is observed. We discuss the relation between the random branching process and the lattice river network models.

6.2.1 Phase Transition in Random Branching Process

Let us consider a simple branching process shown in Fig.6.1 [M. Takayasu (1993)]. A node at generation n independently branches two links making nodes at generation $n+1$ with probability p or ceases branching with probability $1-p$. Starting from one node at generation $n=1$, we consider the probability $P(s)$ that the branch grows to size s. Here, the size of the branch

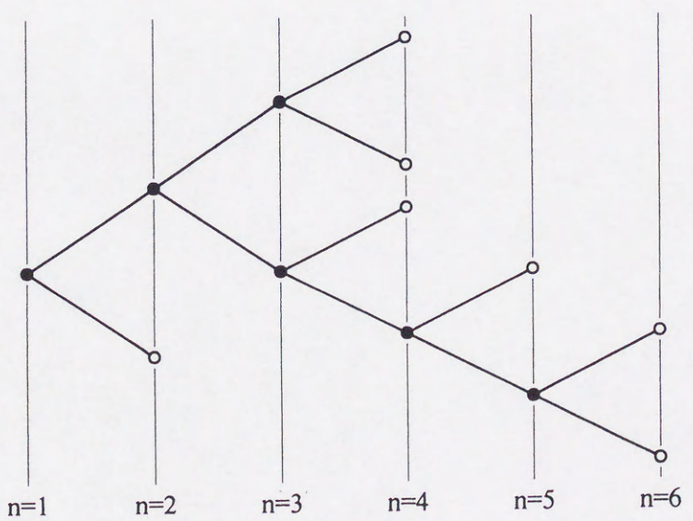

Figure 6.1: An example of the random branching process. The open circles show the halt nodes.

is represented by the number of the nodes contained in the branch. Since the probability that a part of the branch starting from one node at generation n grows to make a subbranch of size s is identical to $P(s)$, the probability distribution $P(s)$ follows

$$P(s+1) = p\sum_{s'=1}^{s} P(s')P(s-s') \quad . \tag{6.1}$$

The relation means that a branch of size $s+1$ is made up of the node at the root and two subbranches of size s' and $s-s'$. By solving Eq.(6.1), we obtain the behavior of the probability distribution for $s \gg 1$ as

$$P(s) \propto s^{-\frac{3}{2}} e^{-as} \quad , \quad a = \log\{4p(1-p)\} \quad . \tag{6.2}$$

As we can see from Eq.(6.2), the distribution has a power-law tail written in a cumulative form as

$$P(\geq s) \propto s^{-\tau} \quad , \quad \tau = \frac{1}{2} \quad , \tag{6.3}$$

at $p = \frac{1}{2}$. In the cases of $p < \frac{1}{2}$ and $p > \frac{1}{2}$, both the distributions decay exponentially but the behaviors of the system are rather different each other. That is, a non-zero value of the probability P_∞ that the branch grows infinitely emerges in the case of $p > \frac{1}{2}$. In this way, the system shows a second order phase transition similar to that of the percolation introduced in Sec.2.1 at $p = \frac{1}{2}$. In this system, the order parameter is the emerging probability of a infinite size branch, P_∞, and the control parameter is the branching probability, p.

Since a node creates 0 or 2 nodes with probability $(1-p)$ and p, respectively, the expectation of the number of the nodes created by one node is calculated as $0 \cdot (1-p) + 2 \cdot p = 2p$. The average number of the nodes at generation n is given by $(2p)^{n-1}$. In the case of $p < \frac{1}{2}$, it is obvious that the average number of nodes decreases exponentially as the generation proceeds since $2p$ is less than 1. It is almost certain that the branch ceases growing in a finite number of generations. On the contrary, the average number of nodes grows

exponentially in the case of $p > \frac{1}{2}$ because $2p$ is larger than 1. In this case, the non-zero value of P_∞ emerges. At the critical point $p = \frac{1}{2}$, the average number of nodes is conserved at each generation. That is, the expectation of the number of nodes created by one node becomes 1:

$$0 \cdot (1-p) + 2 \cdot p \;=\; 1 \quad , \quad p \;=\; \frac{1}{2} \quad . \tag{6.4}$$

In other words, this condition of the node number conservation is the critical condition for the random branching process.

6.2.2 River Network as a Random Branching Process

The river networks discussed in Chapter 4 have branch structures. In the river networks, the streams join each other as water flows down. Here, reversing time, the water flowing the network looks as if it comes from the mouth of the river, bifurcates forming branches, and disappears at the sources. In this case of the time reversal, the river networks can be regarded as a kind of a branching process. In the lattice models of river networks introduced in Chapter 4, the lattice sites and the bonds correspond to the nodes and the links in the random branching process, respectively, and the confluences and the sources of the streams are regarded as the branching and halt nodes, respectively. The number of the links created by one node is not limited to 0 or 2 in the river network models in general. In the general case that a node can create any number of links, the critical condition Eq.(6.4) may be generalized as

$$\sum_k k p_k \;=\; 1 \quad , \tag{6.5}$$

where k and p_k denote the number of the links and the probability that k links is created, respectively. The critical condition Eq.(6.5) is identical to Eq.(4.17) in the discussion of the mean field approach to the river network models in Sec.4.4. According to the discussion in Sec.4.4, the power-law drainage basin

area distribution is obtained only when the condition Eq.(4.17) holds. This fact proves that Eq.(6.5) is really the critical condition for the random branching process of the general case.

The relation Eq.(4.17) is derived from the condition that all lattice sites in the system belong to the part of the river network, that is, the whole system is filled by river network branches. As discussed in Sec.4.1, sufficiently matured river networks cover earth's surface. The river network models such as the Scheidegger's river model and the minimal erosion model also produce river networks covering the whole systems. So the space-filling condition Eq.(4.17) is set to hold in the case of the river networks. It means that the river networks as a random branching process always satisfy the critical condition Eq.(6.5) without tuning of any parameters. In this sense, the river network model can be regarded as a kind of self-organized criticality.

6.3 Fractal Tiling

As we mentioned before, the minimal models studied in this doctoral dissertation all produce fractal domain configurations, which we call fractal tiling. In this section, we introduce deterministic fractal tiling and discuss its properties.

6.3.1 Fractal Configuration of River Basins

As mentioned in the previous section, the Scheidegger's river model and the minimal erosion model produce river networks satisfying the condition Eq.(6.5). However, the exponent of the power-law drainage basin area distribution has different values in both the cases: $\tau = \frac{1}{3}$ and 0.42, respectively. This fact proves that the space-filling condition as the critical condition only insures the systems to produce the power-law drainage-basin area distribution but does not determine the exponent of the distribution.

To clarify the factor which determines the exponent of the drainage-basin area distribution, we focus on the spatial configuration of the drainage basins. We stressed the branch structures in the river networks in the previous section. On the other hand, a branch of streams also forms a compact domain corresponding to the drainage basin on earth's surface. The space-filling condition for the river network branches gives strict spatial restriction to the drainage basins as compact domains. Namely, the domains are required to cover the whole earth's surface without overlap and voids. The shape and the configuration of the drainage basins must be influenced by this condition and it must have a significant effect on the drainage-basin area distribution.

Fig.6.2 illustrates the configurations of the river basins as compact domains in two river network models. By the figure, we recognize that the drainage basins seem to be under several other restrictions as well as the space-filling condition. That is, the collection of the domains forms a self-affine configuration as a whole, and each of the domains has an outlet on the edge of the

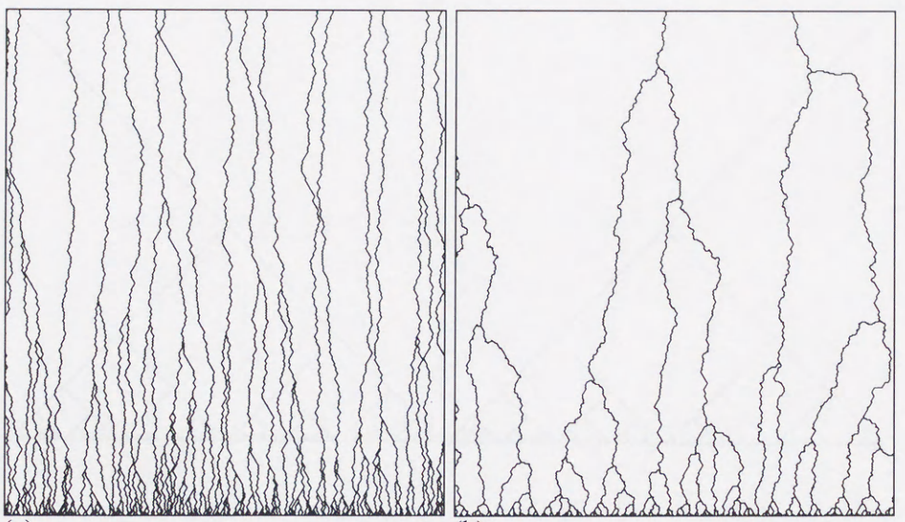

Figure 6.2: The configurations of the river basins by (a) the Scheidegger's river model and (b) the minimal erosion model. The lines in the figures illustrate boundaries between individual river basins.

system and so on. By these conditions, the drainage basins cannot choose their shape freely. In fact, they seem to only have the degree of freedom of the exponent for the self-affine property. It means that the exponent of the power-law domain area distribution is determined uniquely by the exponent for the self-affine property such as the Hack's exponent.

6.3.2 Fractal Tiling and Power-law Distribution

Referring the configurations of the river basins shown in Fig.6.2, let us consider to divide a semiplane into domains as illustrated in Fig.6.3. The figure consists of domains shaped as similar squares, and the whole correction of the squares completely fills the semiplane. By observing a rectangular part of the system with one side located on the edge of the semiplane, we can confirm the

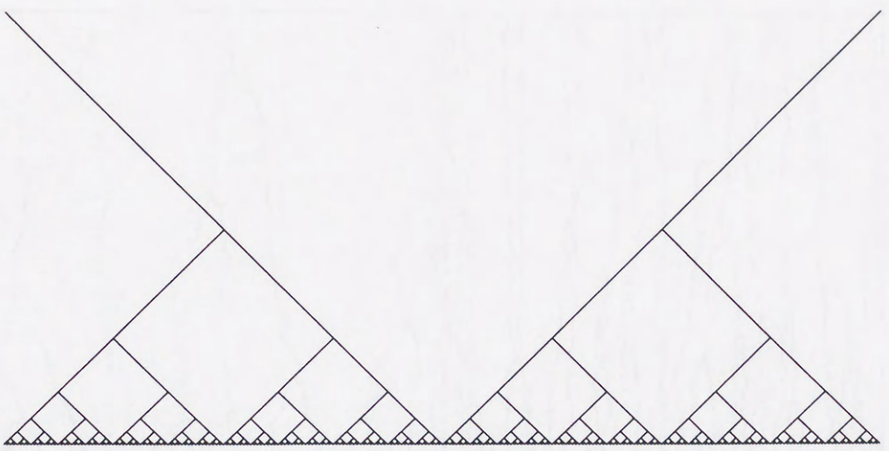

Figure 6.3: An example of the fractal tiling on a semiplane. The edge of the semiplane is placed at the bottom of the figure.

self-similarity of the domain configuration.

In Fig.6.3, let $P(\geq s)$ be the cumulative probability that an arbitrary chosen domain has an area larger than or equal to s. As can be seen from Fig.6.3, by reducing s by a factor of $\frac{1}{4}$, $P(\geq s)$ is doubled. Therefore, the distribution of the domain area has a power-law form as

$$P(\geq s) \propto s^{-\tau} \quad , \quad \tau = \frac{1}{2} \quad . \tag{6.6}$$

In this way, the domain configuration shown in Fig.6.3 leads to a power-law domain area distribution. We call the domain configuration of this type "fractal tiling".

Fig.6.3 has a self-similarity, however, in the cases of the river network models, the drainage basins have a self-affine nature as discussed in Sec.4.1. Namely, there is a relation between h, the diameter of a drainage basin along with the main stream, and w, that across the main stream, as

$$h \propto w^{\nu} \quad , \tag{6.7}$$

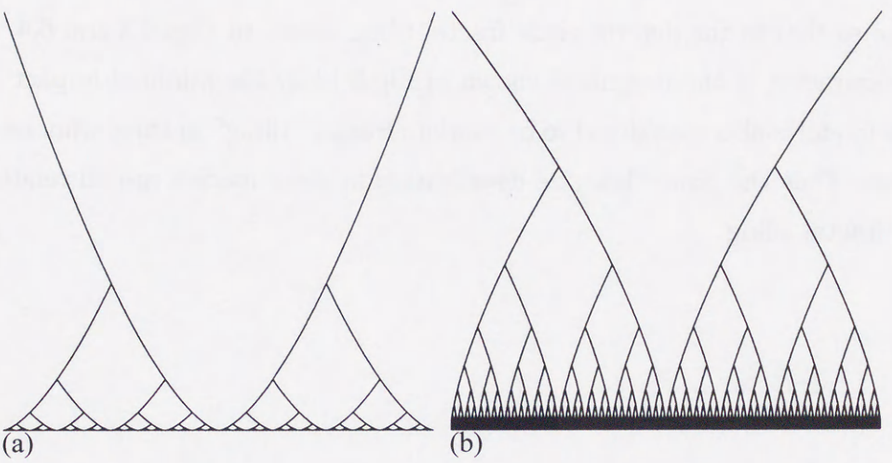

Figure 6.4: Examples for the self-affine fractal tiling on a semiplane for the cases of (a) $\nu = \frac{3}{2}$ and (b) $\nu = \frac{2}{3}$. The edges of the semiplanes are placed at the bottom of the figure.

where ν denotes a positive parameter. For example, in the case of the Scheidegger's model, $\nu = 2$. We can easily generalize the fractal tiling to the self-affine case by transforming the self-similar configuration Fig.6.3 using a function $y' = F(y) = y^{\nu}$, where y and y' denote the distance from the edge of the semiplane before and after the transformation, respectively. The examples are in Fig.6.4. By the transformation, a square domain of area s is transformed into a domain encircled by curves whose area is $s^{\frac{1+\nu}{2}}$. Therefore, the exponent of the domain area distribution is changed to $\tau = \frac{1}{1+\nu}$. Since the parameter ν can take any positive value, the fractal tiling produces the power-law domain area distribution whose exponent is in the range of $0 < \tau < 1$.

We can consider that the self-affine domain configuration Fig.3.9 by the minimal competitive growth model and the drainage-basin configurations in Fig.6.2 by the river network models are kinds of fractal tiling. Although Figs.3.9 and 6.2 have some randomness, we can consider that the basic feature

of the configurations producing the power-law domain area distribution is the same as that in the deterministic fractal tiling shown in Figs.6.3 and 6.4. The configuration of the fragments shown in Fig.5.13 by the minimal impact fracture model is also considered to be random fractal "tiling" in three-dimensional space. Thus the power-law size distribution in these models are all related to the fractal tiling.

References

Bak, P., Tang, C., and Wiesenfeld, K., Phys. Rev. Lett. **59**, 381 (1987).

Bak, P., Tang, C., and Wiesenfeld, K., Phys. Rev. A **38**, 364 (1988).

Bless, S. J., Brar, N. S., Kanel, G., and Rosenberg, Z., J. Am. Ceram. Soc. **75**, 1002 (1992).

Brar, N. S., Bless, S. J., and Rosenberg, Z., Appl. Phys. Lett. **59**, 3396 (1991).

Daccord, G., Nittmann, J., and Stanley, H. E, Phys. Rev. Lett. **56**, 336 (1986).

Daccord, G., Phys. Rev. Lett. **58**, 479 (1987).

Feder, J., *Fractals* (Plenum Press, New York, 1988).

Feller, W., *An Introduction to Probability Theory and Its Applications Vol.2* (John Wiley & Sons, New York, 1966).

Fujikawa, H. and Matsushita, M., J. Phys. Soc. Jpn. **58**, 3875 (1989).

Fujiwara, A. and Tsukamoto, A., ICARUS **44**, 142 (1980).

Gilvarry, J. J., J. Appl. Phys. **32**, 391 (1961).

Gilvarry, J. J. and Bergstrom, B. H., J. Appl. Phys. **32**, 400 (1961).

Hack, J. T., U.S. Geol. Surv. Prof. Pap. **294-B**, 45 (1957).

Hayakawa, Y., private communication (1995).

Hinrichsen, E. L., Måløy, K. J., Feder, J., and Jøssang, T., J. Phys. A **22**, L271 (1989).

Horton, R. E., Bull. Geol. Soc. Am. **56**, 275 (1945).

Inaoka, H., Fractals **1**, 977 (1993).

Inaoka, H. and Takayasu, H., Phys. Rev. E **47**, 899 (1993).

Inaoka, H. and Takayasu, H., preprints (1995).

Inaoka, H. and Takayasu, H., to appear in Fractals (1996).

Ishii, T. and Matsushita, M., J. Phys. Soc. Jpn. **61**, 3474 (1992).

Kelley, K. W., editor, *The Home Planet* (Addison-Wesley, Massachusetts, 1988).

La Barbera, P. and Rosso, R., Water Resour. Res. **25**, 735 (1989).

Leopold, L. B. and Langbein, W. B., U.S. Geol. Surv. Prof. Pap. **500-A**, A1 (1962).

Li, R., Takayasu, H., and Inaoka, H., to appear in Fractals (1996).

Mandelbrot, B. B., Science **155**, 636 (1967).

Mandelbrot, B. B., *The Fractal Geometry of Nature* (W. H. Freeman, New York, 1982).

Manna, S. S., J. Stat. Phys. **59**, 509 (1990).

Manna, S. S., J. Phys. A **24**, L363 (1991).

Matsushita, M., Sano, M., Hayakawa, Y., Honjo, H., and Sawada, Y., Phys. Rev. Lett. **53**, 286 (1984).

Meakin, P., Phys. Rev. A **27**, 2616 (1983).

Meakin, P., Phys. Rev. B **30**, 4207 (1984).

Meakin, P., Feder, J., and Jøssang, T., Physica A **176**, 409 (1991).

Niemeyer, L., Pietronero, L., and Wiesmann, H. J., Phys. Rev. Lett. **52**, 1033 (1984).

Oddershede, L., Dimon, P., and Bohr, J., Phys. Rev. Lett. **71**, 3107 (1993).

Pietronero, L., Vespignani, A., and Zapperi, S., Phys. Rev. Lett. **72**, 1690 (1994).

Rácz, Z. and Vicsek, T., Phys. Rev. Lett. **51**, 2382 (1983).

Radnoczi, Gy., Vicsek, T., Sander, L. M., and Grier, D., Phys. Rev. A **35**, 4012 (1987).

Rodríguez-Iturbe, I., Ijjász-Vásquez, E. J., Bras, R. L., and Tarboton, D. G., Water Resour. Res. **28**, 1089 (1992).

Scheidegger, A. E., *Theoretical Geomorphology* (Springer-Verlag, Berlin, 1961).

Scheidegger, A. E., Bull. Internat. Assoc. Sci. Hydrol. **12**, 15 (1967).

Scheidegger, A. E., Water Resour. Res. **4**, 167 (1968a).

Scheidegger, A. E., Water Resour. Res. **4**, 1015 (1968b).

Stanley, H. E., *Introduction to Phase Transitions and Critical Phenomena* (Oxford University Press, New York, 1987).

Stauffer, D. and Aharony, A., *Introduction to Percolation Theory* (Taylor & Francis, London, 1985).

Strahler, A. N., Bull. Geol. Soc. Am. **63**, 1117 (1952).

Takayasu, H., J. Phys. Soc. Jpn. **57**, 2585 (1988).

Takayasu, H., *Fractals in the physical sciences* (Manchester University Press, Manchester, 1990).

Takayasu, H., Takayasu, M., Provata, A., and Huber, G., J. Stat. Phys. **65**, 725 (1991).

Takayasu, H. and Inaoka, H., Phys. Rev. Lett. **68**, 966 (1992).

Takayasu, H., Fractals **1**, 521 (1993).

Takayasu, M., Doctor's thesis (1993).

Tarboton, D. G., Bras, R. L., and Rodriguez-Iturbe, I., Water Resour. Res. **24**, 1317 (1988).

Tarboton, D. G., Bras, R. L., and Rodriguez-Iturbe, I., Water Resour. Res. **26**, 2243 (1990).

Tolman, S., Meakin, P., and Matsushita, M., J. Phys. Soc. Jpn. **58**, 2721 (1989).

Vicsek, T., *Fractal growth phenomena* (World Scientific, Singapore, 1989).

Witten, Jr., T. A. and Sander, L. M., Phys. Rev. Lett. **47**, 1400 (1981).

Witten, T. A. and Sander, L. M., Phys. Rev. B **27**, 5686 (1983).

Wittmann, R., Kautzky, T., Hübler, A., and Lüscher, E., Naturwissenschaften **78**, 23 (1991).

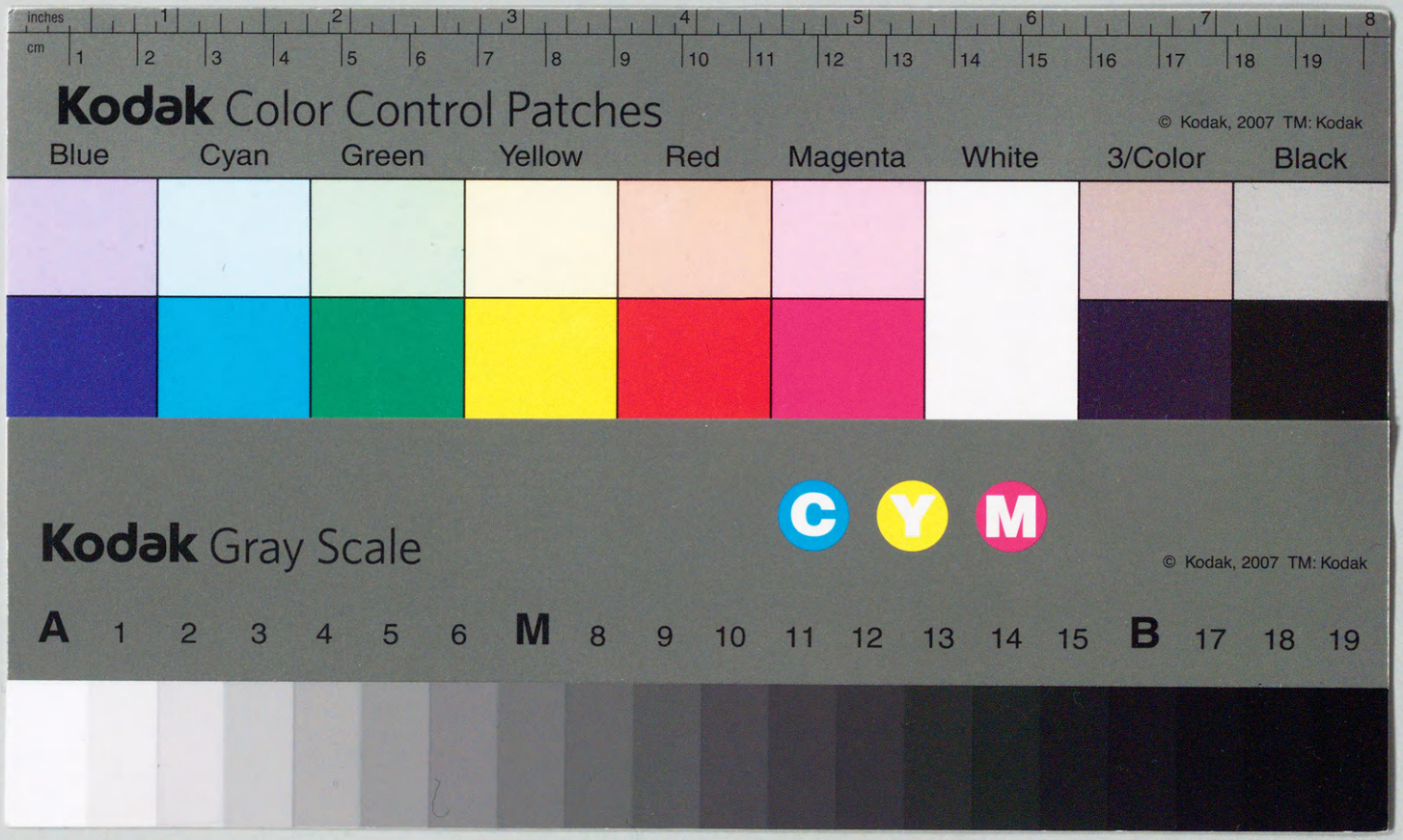
inches
cm
Kodak Color Control Patches
© Kodak, 2007 TM: Kodak
Blue
Cyan
Green
Yellow
Red
Magenta
White
3/Color
Black
Kodak Gray Scale
C
Y
M
© Kodak, 2007 TM: Kodak
A 1 2 3 4 5 6 M 8 9 10 11 12 13 14 15 B 17 18 19